Studies on Conformational Characteristics and Self-Assembled Structures of Polymers in Space-Limited Systems

Ryojun SEKINE

2009

Contents

Chapter 1. *General Introduction*

1.1. Background and Motivation 1

1.1.1. Langmuir-Blodgett Method 3

1.1.2. Phase Behavior of Block Copolymers 5

1.1.3. Scanning Near-Field Optical Microsocopy 6

1.1.4. Radiation Effect on Polymers 9

1.2. Outline of This Thesis 11

References 13

Part I

Chapter 2. *Conformation of Single Poly(methyl methacrylate) Chains in an Ultra-Thin Film Studied by Scanning Near-Field Optical Microscopy*

2.1. Introduction 21

2.2. Experimental Section 24

2.2.1. Sample Preparation 24

2.2.2. SNOM Measurement 25

2.3. Results and Discussion 26

2.3.1. Comparison of Confocal Microscopy and SNOM Image 26

2.3.2. SNOM Imaging of a Single PMMA Chain 28

2.3.3. Single Chain Conformation in the Various Film Thickness 31

2.4. Conclusion 36

References and Note 37

Chapter 3. ***Conformational Relaxation of Single Polymer Chain in a Monolayer Studied by Scanning Near-Field Optical Microscopy***

3.1. Introduction 41

3.2. Experimental Section 43

3.2.1. Sample Preparation 43

3.2.2. SNOM Measurement 44

3.3. Results and Discussion 45

3.3.1. SNOM Imaging of a Single PMMA Chain in the Lateral Directions 45

3.3.2. SNOM Measurement of the Cross-Section of the Sample Films 50

3.4. Conclusion 54

References and Note 56

Chapter 4. ***Localization and Orientation of Homopolymer in Block Copolymer Lamella Studied by Scanning Near-Field Optical Microscopy***

4.1. Introduction 59

4.2. Experimental Section 61

4.2.1. Sample Preparation 61

4.2.2. SNOM Measurements 62

4.3. Results and Discussion 63

4.3.1. SNOM Imaging of a Single PMMA-Pe Chain 63
4.3.2. Analyses of SNOM images 65
4.3.2.1. Conformation, Orientation, and Center of Mass of a Single PMMA Chain 65
4.3.2.2. Determination of Lamellar Spacing and Lamellar Orientation 67
4.3.2.3. Determination of the CM Location of a PMMA-Pe Chain in the Lamella 68
4.3.3. Localization of PMMA Homopolymer Chains in the Lamlla. 70
4.3.4. Relative Orientation of PMMA Homopolymer Chains in the Lamella 72
4.4. Conclusion 76
References and Notes 77

Part II

Chapter 5. ***Conformation of Single Block Copolymer Chain in Two-Dimensional Microphase-Separated Structure Studied by Scanning Near-Field Optical Microscopy***

5.1. Introduction 83
5.2. Experimental Section 86
5.2.1. Synthesis of Diblock Copolymers 86
5.2.2. Monolayer Preparation 87
5.2.3. SNOM Measurement 88
5.3. Results and Discussion 88
5.3.1. AFM Measurement 88
5.3.2. SNOM imaging of a Single PiBMA Sub-Chain 90

5.3.3. Curvature Dependence of PiBMA Sub-Chain Localization 93
5.3.4. Relative Orientation of PiBMA Sub-Chain 95
5.4. Conclusion 97
References 99

Chapter 6. ***Chain End Distribution in Two-Dimensional Microphase-Separated Structure Studied by Scanning Near-Field Optical Microscopy***

6.1. Introduction 103
6.2. Experimental Section 105
6.2.1. Synthesis of Diblock Copolymers 105
6.2.2. Monolayer Preparation 107
6.2.3. SNOM Measurement 107
6.3. Results and Discussion 108
6.3.1. AFM Measurement 108
6.3.2. SNOM Imaging of Microphase-Separated Monolayers 108
6.3.3. Evaluation of Chain End Distribution 110
6.4. Conclusion 116
References and Note 117

Chapter 7. ***Radiation-Induced Fabrication of Polymer Nanoporous Materials from Microphase-Separated Structure of Diblock Copolymers as a Template***

7.1. Introduction 121

7.2. Experimental Section 123
7.2.1. Materials 123
7.2.2. Sample Preparation 123
7.2.3. Measurements 124
7.3. Results and Discussion 124
7.3.1. Solubility Test and IR Spectra 124
7.3.2. TEM measurement 126
7.3.3. SEM measurement 131
7.4. Conclusion 133
References 135

Summary 137

List of Publication 141

Acknowledgements 143

Chapter 1

General Introduction

1.1. BACKGROUND AND MOTIBATION

Polymers have been widely used in various fields because of a variety of structures and properties. The improvement of properties of polymeric materials has important implications in industrial, medical, and household applications. The physical and chemical properties of polymer materials are closely correlated to their structures. In an intermediate region of 1–100 nm between a molecule and bulk materials, the physical properties are different from those in the bulk. Therefore, the controlled structure in a nanometric scale has great potential to produce materials and devices with novel properties. Since the dimension of a polymer chain is in the order of 10–100 nm, polymeric materials have drawn much attention as the basic components of nano-materials.[1-8] Numerous researchers have attempted to fabricate the polymeric nano-materials with novel properties and functions by controlling the structures in the range of 10–100 nm.

Two strategies have been taken for designing nano-structures: top-down and bottom-up approaches.[9,10] The top-down approach provides small structures from larger materials and involves the use of the etching technique. Traditional top-down approach such as scanned-probe lithography[11-15] and electron-beam lithography[16,17] allows artificial designs with a nanometer-level accuracy. Alternatively, the bottom-up approach, where nanometric structures are constructed from their atomic or molecular constituent, is based on natural molecular assemblies to form the nano-structures. The Langmuir-Blodgett (LB) technique is one of the most promising method for providing

organized molecular assemblies with well-defined molecular arrangement.[1] In the LB method, ordered monolayers can be formed over large area and the organized monolayers can be transferred on to a solid substrate. The sequential deposition of the monolayers constructs artificially well-ordered multi-layer films at a molecular level with simple operation[18,19] and the thickness of the films is precisely controlled by the number of deposited layers. The LB technique has been widely used to prepare ultra-thin films for gas separation,[20,21] gas/ion sensors,[22,23] and lithography.[24] On the other hand, a recent trend of the bottom-up fabrication of nano-structures is a self-organization because the ordered structure can be spontaneously formed. Block copolymers covalently consisting of immiscible polymers can self-assemble to form a variety of the nano-structures based on the microphase separation. The scale of the block copolymer self-assembly is directly related to the length of the polymer chain, which is typically 10–200 nm.[25,26] Owing to their various nanometric ordered structures, block copolymers have the potential to fabricate practical products such as high-density data storage media,[27-29] molecular separation membrane,[30] and so forth. Thus, in the past decades many groups have reported the properties and structure of block copolymers in thin film as well as in bulk state for the purpose of fabrication of nano-materials using the microphase-separated structures.[31-36] In thin films, the behavior of polymers differs appreciably from the bulk when the thickness is less than the unperturbed dimension of the polymer chain.[37-44] The interaction between the polymers and the interface plays a crucial role to determine the properties of confined polymers. Since the degree of freedom of the polymer chain is restricted by the spatial confinement in a nanometric scale, the reduction of the conformational entropy of the polymer chain is also important as well as the interface effect. Thus, the chain conformation of polymers is one of the most fundamental issues from the view points of not only the scientific interest but also the practical importance.

The present thesis focuses on the local structures of polymers confined in nanometric geometry at the single chain level. In order to directly observe the individual polymer chain, scanning near-field optical microscopy (SNOM) was employed, which enables optical measurements with a high spatial resolution beyond the diffraction limit of light. The conformation of the individual chain was observed for ultra-thin films and microphase-separated structure of block copolymers, where the polymer chain was constrained in a small space less than the unperturbed dimension. An application of the nanometric polymer structure to fabricate an ordered nano-porous material is also discussed. The author utilized the self-assembled structure of block copolymers as a template to obtain a porous structure. Through the γ-ray-induced simultaneous cross-linking and degradation for each block, the nanoporous material was fabricated. The mechanism of the fabrication process of the nanoporous structure is discussed.

1.1.1. Langmuir-Blodgett Method

The Langmuir-Blodgett (LB) technique, estblished by Langmuir and Blodgett in 1931, is still useful for making ultra-thin organic films with a controlled multilayer structure.[1,45-47] Amphiphilic molecules are adsorbed on the air/water interface under the balance of hydrophilic and hydrophobic groups as shown in Figure 1.1a. Compression up to an appropriate surface pressure makes a uniform monolayer with a thickness of the single molecule. The monolayer on the water surface can be transferred onto a solid substrate by vertical dipping. The deposition of a monolayer can be repeated several times to build up a film with an accurately desired thickness, and to fabricate multilayered nano-structures of ultra-thin films with a desired order. The conventional scheme of the LB technique is illustrated in Figure 1.1. The quality of the LB films depends on the character of the source materials. Although the LB films made of the

low molecular weight fatty acid have problems of reproducibility and defects, in the 1980s many amphiphilic polymers were found to form stable monolayers on the water surface.[48-52] The polymer monolayers possess characteristics such as thinness, homogeneity, mechanical and thermal stability, which are different from those of low molecular weight materials. Such amphiphilic polymers provide the extremely thin polymer films with few defects.

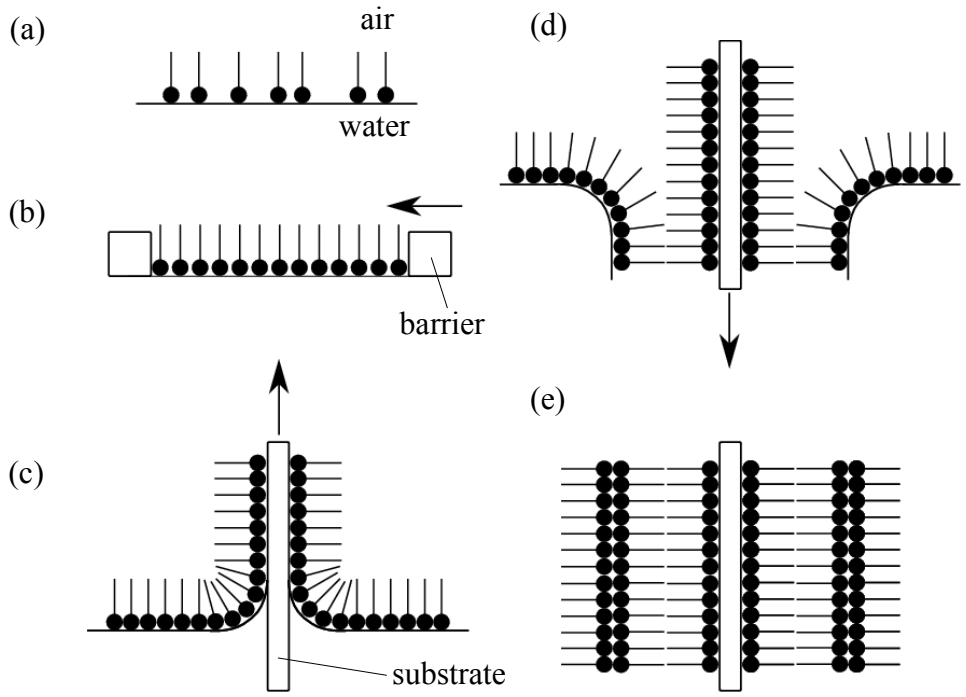

Figure 1.1. Conventional schematic of LB technique. In the first step (a), an amphiphilic molecules are dissolved in a volatile solvent that are then spread at the air/ water interface. The reduction in the area of the trough with a barrier alters the local density of the molecules(b). To form the LB film (c), a substrate is passed through the interface a given number of times, with each pass adding another monolayer to the LB film (d and e)

1.1.2. Phase Behavior of Block Copolymers

Block copolymers consisting of incompatible polymers can self-assemble into a rich variety of nanoscale periodic patterns.[25,26,53,54] The thermodynamics governing the self-assembly of diblock copolymers is now established from both experimental[25] and theoretical[55] perspectives. The microphase separation is induced by the enthalpy gain of demixing of the constituent components of the block copolymers, while the phase separation at a macroscopic scale is prevented by the chemical connectivity of the blocks. An essential parameter in all theories of block copolymer segregation is the segment-segment interaction parameter χ (Flory-Huggins interaction parameter), which provides the driving force of the phase separation. In the linear diblock copolymers, it is described as

$$\chi = \frac{Z}{k_B T}\left(\varepsilon_{AB} - \frac{(\varepsilon_{AA} + \varepsilon_{BB})}{2}\right), \tag{1.1}$$

where ε_{AB} is the interaction energy between A and B monomers, Z is the number of the nearest neighboring monomer units to a block copolymer for a lattice site, k_B is the Boltzmann constant, and T is the temperature. A positive χ shows a repulsive interaction between the A and B monomers, whereas a negative value means mixing of different type of monomers. Another parameter that strongly influences the phase behavior is degree of polymerization N. If N is sufficiently large, the microphase separation is accomplished with some loss of the translational and configurational entropy by local compositional ordering. Since the entropic and enthalpic contributions to the free energy are scaled by N^{-1} and χ, respectively, the product χN is one of the most important parameters to describe the phase state of the block copolymers. When the χN exceeds 10.6, the block copolymers undergo the order-disorder transition. The phase behavior of block copolymers is represented in a morphology diagram in terms of χN and φ. Here φ is the volume fraction of one block. For diblock copolymers, a

lamellar phase is observed for symmetric diblocks (φ = 0.5), whereas asymmetric diblocks form bicontinuous gyroids, hexagonally packed cylinders, and BCC spheres as shown in Figure 1.2.[56] The control of the χN and φ leads to the desirable phase-separated structures and their sizes.

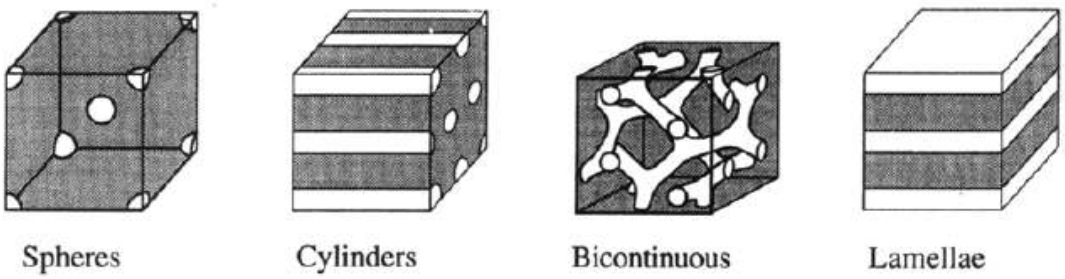

Figure 1.2. Four equilibrium morphologies for a polystyrene-*block*-polyisoprene (PS-*b*-PI) diblock copolymer.

1.1.3. Scanning Near-Field Optical Microscopy

The polymer structures in nanometer dimensions have been revealed owing to the recent developments in analytical instruments such as X-ray and neutron scattering, atomic force microscopy, and electron microscopy. Among these analytical techniques, optical microscopy is one of the most versatile tools, and has been successfully applied to the real space imaging of the structure of polymer systems. Not only imaging but also time-resolving, highly sensitive, and spectroscopic analyses are possible due to the benefits related to light. However, the spatial resolution of conventional microscopy theoretically limited to a half of the wavelength, i.e., 200–400 nm in the visible region. This limitation is called the diffraction limit.[57-60] Therefore, when the object is smaller than a few hundred nanometers, it is impossible to observe its structure. Thus, optical microscopy cannot be applied to the polymer structures in the range of 10 to 100 nm, which numerous researchers desire to observe because a polymer chain measures in the

order of 10 nm and the basic unit making up the material structure is within this scale. Scanning near-field optical microscopy (SNOM) has been developed as a novel technique that overcomes the optical diffraction barrier.[61-69] SNOM can reach a spatial resolution down to tens of nanometers and can examine the chemical composition of samples below the probe tip through fluorescence[70-73] and Raman spectroscopy.[74-79] Therefore, SNOM is one of the most suitable methods for investigating the polymer structure, and the high resolution of SNOM allows one to image the conformation of the polymer chain.[80] In recent years, SNOM has been widely applied in many fields of polymer science such as studies on the polymer chain conformation in a bulk medium,[81] phase separation in polymer blend,[82,83] and the self-assembled structure of block copolymers.[84-86]

The principle of SNOM is as described briefly below. Two small objects A and B are considered. When object A is illuminated by light, the interaction between the light and object A results in the generation of far-field and near-field light components as shown in Figure 1.3a. The far-field propagates through the space as a scattered light whereas the optical near-field is confined around object A as a non-propagating component of light. The distribution of the optical near-field is dependent on the size and shape of object A, and not on the wavelength of the illuminating light. Therefore, a local structure smaller than the wavelength can be observed by the use of the optical near-field. However, since the optical near-field exists only in the vicinity of object A, it is impossible to detect the near-field at a distance larger than a wavelength of light. When object B is placed close to object A in a distance shorter than the wavelength of light (λ) as illustrated in Figure 1.3b, the optical near-field generates around object B and the optical near-field around object A is scattered as a propagating component. Thus, the optical near-field generated around A can be detected as the far-field scattered by B.

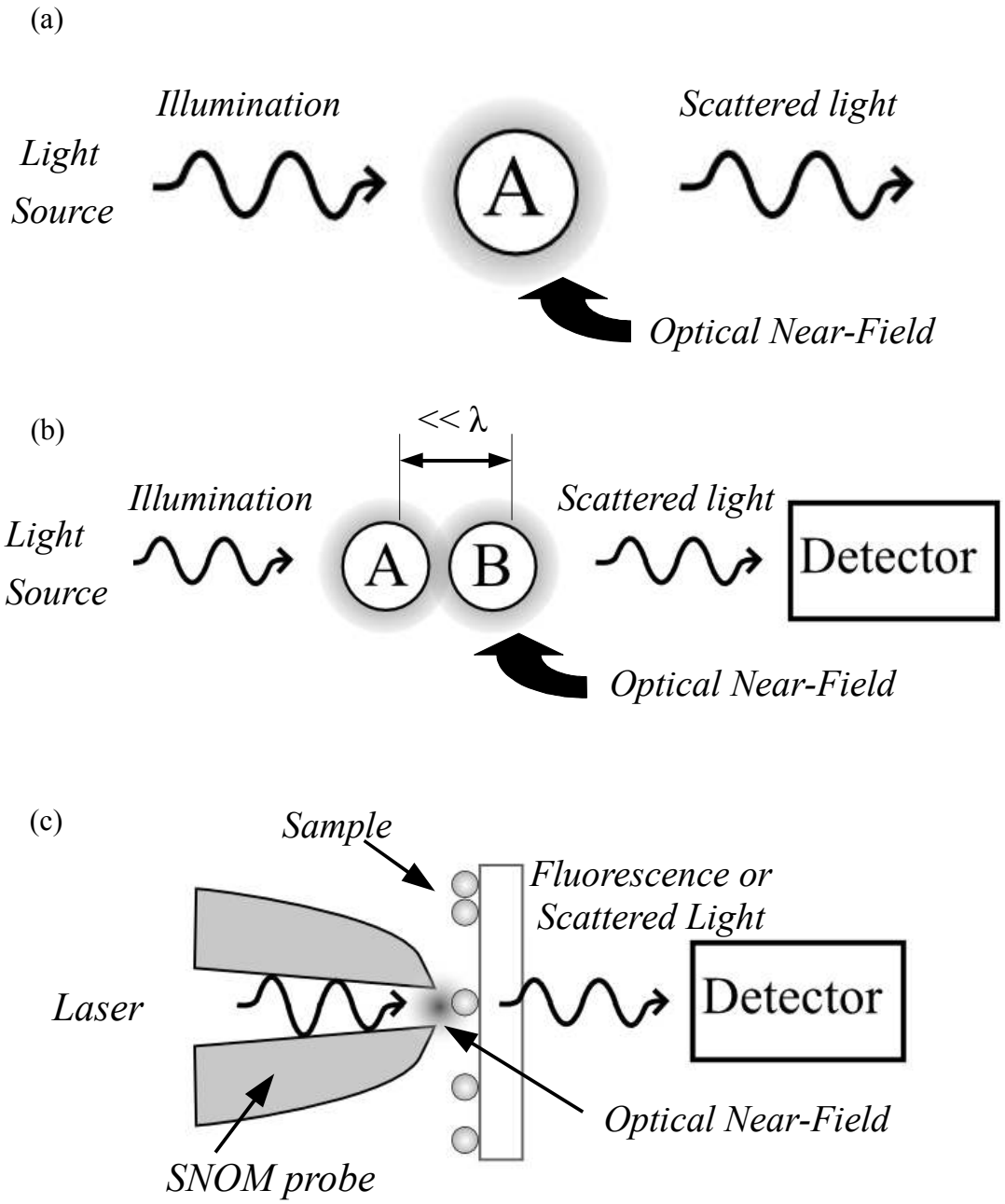

Figure 1.3. Schematic illustration of the optical near-field system. In (a), the optical near-field around object A and far-field are generated by illumination of light. In (b), the two objects, A and B, are placed in a distance shorter than the wavelength of the illuminating light. The optical near-field of object A is monitored by a detector as the scattered light from object B. In (c), the illustration-mode SNOM is depicted schematically. Object A and B in (b) correspond to the SNOM probe and a sample, respectively.

In the actual SNOM system, objects A and B correspond to a probe and a specimen, respectively, and the probe has an aperture much smaller than the wavelength of light as shown schematically in Figure 1.3c. When a laser beam is coupled to the aperture, the optical near-field generates around the aperture. The optical near-field illuminates the sample surface, and the intensities of the signal light from the sample are monitored as a function of the position of the aperture. The obtained two-dimensional array of the signal intensity corresponds to the convolution of the optical near-field and the sample structure. By using the probe with a well-known structure, one can obtain the optical image with a spatial resolution of several tens of nanometers.

1.1.4. Radiation Effects on Polymers

When solid polymeric materials are exposed to ionizing radiation such as γ-ray and high-energy electrons, highly reactive intermediates are formed. These intermediates can follow several reaction paths, which result in the formation of oxidized products, grafts, scission or cross-linking of the main chains.[87,88] The degree of these conversion depends on the structure of the polymer and the irradiation conditions.[89] When the polymers are irradiated in a vacuum condition, either of cross-linking and degradation is predominantly observed. In this aspect, polymers are roughly classified into radiation cross-linking and degrading polymers (Figure 1.4).[90,91] Millar et al. reported an empirical relationship between the radiation effect and the chemical structure of vinyl polymers.[88] When a polymer contains an α-hydrogen atom, the γ-ray irradiation induces the cross-linking of the main chain. On the other hand, the polymer without the α-hydrogen atom undergoes the degradation reaction. The radiation-induced cross-linking starts from the cleavage of a C–H bond on one polymer chain to form a hydrogen radical. The subsequent abstraction of a second hydrogen atom from a neighboring chain produces a hydrogen molecule. Then the two adjacent

polymeric radicals combine to form a cross-link. In contrast, chain scission is the opposite process of cross-linking where the rupture of C–C bonds occurs. The irradiation on the polymers also makes the cleavage of the C–C main chain and forms two polymer radicals. Before the recombination of the polymeric radicals, the polymeric radical combines the hydrogen radical formed by the cleavage of a C–H bond, resulting in the degradation. In the polymers with α-carbon, a C–C double bond is formed between the main chain carbon and the α-carbon by the disproportionation of the methylene radical produced by the cleavage of the C–H bond of the α-carbon. Consequently, the C–C bond of the main chain is ruptured.

Radiation Cross-linking Polymers

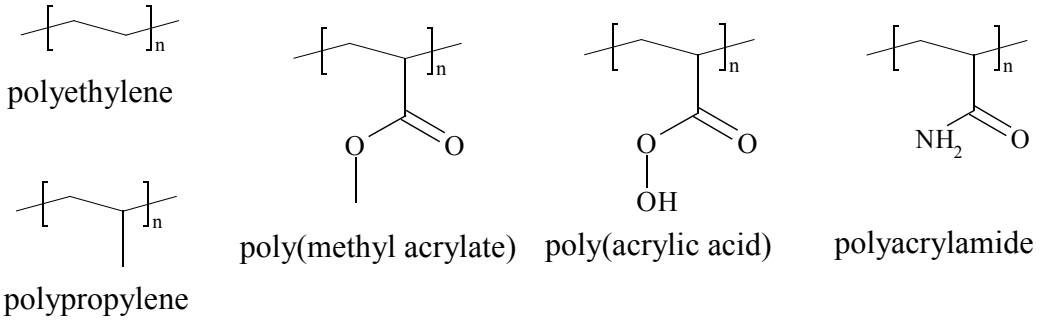

Radiation Degrading Polymers

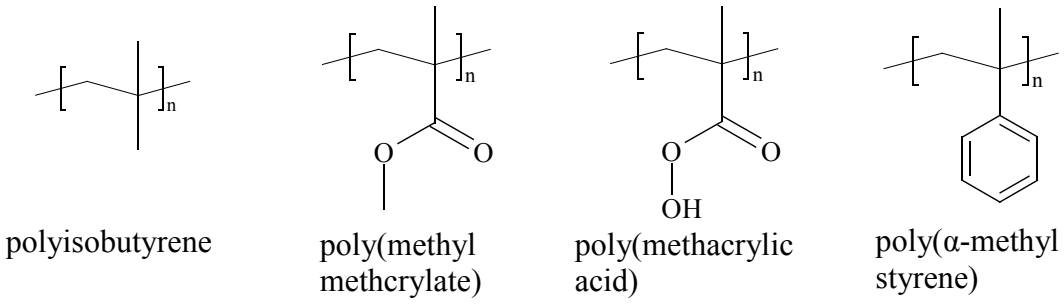

Figure 1.4. Radiation effect on polymers in vacuo.

1.2. OUTLINE OF THIS THESIS

This thesis consists of seven chapters. The first chapter describes the background and the motivation of this thesis, in which the key concept of the LB method, phase behavior of block copolymers, scanning near-field optical microscopy, and radiation chemistry for polymeric systems are mentioned. The following six chapters are divided into two parts. Part I (Chapters 2, 3, and 4) deals with the conformation of single polymer chain under confined geometries.

In Chapter 2, the conformation of poly(methyl methacrylate) (PMMA) confined in the thin film is investigated by SNOM. The direct observation by SNOM is performed for individual PMMA chains in thin films with a thickness less than the unperturbed chain dimension in the bulk state. Through the radius of gyration for the projection of PMMA chains in the two-dimensional plane, the effect of the constraint in the height direction on the polymer chain is examined.

In Chapter 3, the conformational relaxation of PMMA chains confined in a two-dimensional plane to a three-dimensional random coil is investigated. The direct SNOM observation is performed for the individual PMMA chain in a LB monolayer on a bulk PMMA film. The shape and segment density of the individual chains are analyzed at different annealing times. The thermally induced distribution change of PMMA segments is investigated through the cross-sectional observation in comparison with the translational diffusion of the whole chain. The conformational change of the polymer chain free from the two-dimensional restriction is discussed.

In Chapter 4, a single PMMA homopolymer chain confined in a lamellar phase-separated structure formed by polystyrene-*block*-poly(methyl methacrylate) (PS-*b*-PMMA) is investigated by SNOM. The distribution of the PMMA homopolymer chains in the PS-*b*-PMMA lamella is investigated by measuring the center of mass of the PMMA homopolymer chain and the orientational angle of PMMA homopolymer chain

to the PS-*b*-PMMA lamella. The relationship between the localization and the orientation of PMMA homopolymer chains confined in the lamella are discussed.

Part II (Chapters 5, 6, and 7) describes the nano-structures formed by block copolymers.

In Chapter 5, the conformation of poly(isobutyl methacrylate) (PiBMA) block chains in the two-dimensional microphase-separated structure formed by poly(octadecyl methacrylate)-*block*-poly(isobutyl methacrylate) (PODMA-*b*-PiBMA) is investigated by SNOM. The distribution and the orientational angle of PiBMA block chain in the PODMA-*b*-PiBMA lamella are analyzed and the relationship between the conformation of the block chain and the curvature of the domain interface is discussed.

In Chapter 6, the chain-end distribution of the PiBMA block in a two-dimensional microphase-separated structure formed by PODMA-*b*-PiBMA is studied by SNOM. The spatial distributions of the PiBMA block and the PiBMA block chain-end are analyzed and compared. The chain-end distribution of PiBMA block in the two-dimensional microphase-separated structure is discussed in comparison with that in the three-dimensional one.

In Chapter 7, the fabrication from the microphase-separated structure of diblock copolymers as a template is performed through the simultaneous cross-linking and degradation by γ-irradiation. Polybutadiene-*block*-poly(methyl methacrylate) (PB-*b*-PMMA) and PS-*b*-PMMA are used as a sample. Through the solubility test, IR spectroscopy, and electron microscopy observations, the cross-linking and degradation of the each block of PB-*b*-PMMA with the ordered nano-structure are discussed in comparison with those of PS-*b*-PMMA.

References

1. A. Ulman, "*An Introduction to Ultrathin Films from Langmuir-Blodgett to Self-Assembly*", Academic Press, San Diego (1991).
2. H. Vasquez, K. Lozano, V. Soto, and A. Rocha, *Measurement*, **41**, 870 (2008).
3. T. Taniguchi, Y. Fukasawa, and T. Miyashita, *J. Phys. Chem. B*, **103**, 1920 (1999).
4. J. A. Forrest, K. Dalnoki-Veress, J. R. Stevens, and J.R. Dutcher, *Phys. Rev. Lett.*, **77**, 2002 (1996).
5. J.A. Forrest, C. Svanverg, K. Revesz, M. Rodahl, L. M. Torell, and B. Kasemo, *Phys. Rev. E*, **58**, 1226 (1998).
6. Y.-K. See, J. Cha, T. Chang, and M. Ree, *Langmuir*, **16**, 2351 (2000).
7. Park C, Yoon J, and Thomas EL, *Polymer*, **44**, 6725 (2003).
8. J. Njuguna, K. Pielichowski, and S. Desai, *Polym. Adv. Technol.*, **19**, 947 (2008).
9. D. Mijatovic, J. C. T. Eijkel and A. van den Berg, *Lab Chip*, **5**, 492 (2005).
10. N. Zhihong, *Nature Materials*, **7**, 277 (2008).
11. S. Davy and M. Spajer, *Appl. Phys. Lett.*, **69**, 3306 (1996).
12. D. P. Tsai and W. R. Guo, *J. Vac. Sci. Technol. A*, **15**, 1442 (1997).
13. A. Naber, T. Dziomba, U. C. Fischer, H.-J. Maas, and H. Fuchs, *Appl. Phys. A*, **70**, 227 (2000).
14. S. Nolte, B. N. Chichkov, H. Welling, Y. Shani, K. Lieberman, and H. Terkel, *Opt. Lett.*, **24**, 914 (1999).
15. R. Zenobi and V. Deckert, *Angew. Chem. Int. Ed.*, **39**, 1746 (2000).
16. C. N. Kim, D. W. Kang, E. R. Kim, and H. Lee, *Synthetic metals*, **85**, 1407 (1997).
17. W. Zhang, A. Potts, D. M. Bagnall, and B. R. Davidson, *Thin Solid Films*, **515**, 3714 (2007).
18. A. W. Adamson, "*Physical Chemistry of Surfaces*", Wiley, New York (1960).
19. G. G. Roverts, *Adv. Phys.*, **34**, 475 (1985).

20. L. H. Zhang, R. A. Hendel, P. G. Cozzi and S. L. Regen, *J. Am. Chem. Soc.*, **121**, 1621 (1999).
21. T. Riedl, W. Nitsch, and T. Michel, *Thin Solid Films*, **379**, 240 (2000).
22. S. S. Shiratori, K. Kohno, and M. Yamada, *Sens. Actuators B*, **64**, 70 (2000).
23. K. Sirkar, A. Revzin, and M. V. Pishko, *Anal. Chem.*, **72**, 2930 (2000).
24. A. Aoki, M. Nakaya, and T. Miyashita, *Macromolecules*, **31**, 7321 (1998).
25. F. S. Bates and G. H. Fredrickson, *Annu. Rev. Phys. Chem.*, **41**, 525 (1990).
26. I. W. Hamley, "*The Physics of Block Copolymers*", Oxford University Press, New York (1998).
27. K. Liu, S. M. Baker, M. Tuominen, T. P. Russell, and I. K. Schuller, *Phys. Rev.B*, 63, 060403 (2001).
28. M. Park, C. Harrison, P. M. Chaikin, R. A. Register, and D. H. Adamson, *Science*, **276**, 1401 (1997).
29. C. Park, J. Yoon, and E. L. Thomas, *Polymer*, **44**, 6725 (2003).
30. G. Widawski, M. Rawiso, and B. Francois, *Nature*, **369**, 387 (1994).
31. K. Fukunaga, T. Hashimoto, H. Elbs, and G. Krausch, *Macromolecules*, **35**, 4406 (2002).
32. B. H. Sohn and S. H. Yun, *Polymer*, **43**, 2507 (2002).
33. T. Xu, Y. Xhu, S. P. Gido, and T. P. Russell, *Macromolecules*, **37**, 2625 (2004).
34. D. M. Lambreva, R. Opitz, G. Reiter, P. M. Frederik, and W. H. de Jeu, *Polymer*, **46**, 4868 (2005).
35. J.-Y. Wang, W. Chen, and T. P. Russell, *Macromolecules*, **41**, 7227 (2008).
36. L. He, L. Zhang, and H. Liang, *J. Polym. Sci. Polym. Phys. Ed.*, **47**, 1 (2009).
37. J. L. Keddie, R. A. L. Jones, and R. A. Cory, *Faraday Discuss.*, 219 (1994).
38. J. L. Keddie, R. A. L. Jones, and R. A. Cory, *Europhys. Lett.*, **27**, 59 (1994).
39. K. Tanaka, A. Taura, S. R. Ge, A. Takahara, and T. Kajiyama, *Macromolecules*, **29**,

3040 (1996).

40. T. Kajiyama, K. Tanaka, and A. Takahara, *Macromolecules*, **30**, 280 (1997).
41. O. K. C. Tsui and H. F. Zhang, *Macromolecules*, **34**, 9139 (2001).
42. Y. Grohens, L. Hamon, G. Reiter, A. Soldera, and Y. Holl, *Eur. Phys. J. E*, **8**, 217 (2002).
43. L. Si, M. V. Massa, K. Dalnoki-Veress, H. R. Brown, and R. A. L. Jones, *Phys. Rev. Lett.*, **94**, 127801 (2005).
44. K. Tanaka, Y. Tsuchimura, K. Akabori, F. Ito, and T. Nagamura, *Appl. Phys. Lett.*, **89**, 061916 (2006).
45. Gaines, G. L., Jr. "*Insoluble Monolayers at Liquid-Gas Interfaces*", Wiley interscience, New York, (1966).
46. K. Blodgett, *J. Am. Chem. Soc.*, **56**, 495 (1934).
47. K. Blodgett, *J. Am. Chem. Soc.*, **57**, 1007 (1935).
48. S. J. Mumby, J. D. Swalenand, and J. F. Rabolt, *Macromolecules*, **19**, 1054 (1986).
49. M. Watanabe, Y. Kosaka, K. Oguchi, K. Sanui, and N.Ogata, *Macromolecules*, **21**, 2997 (1988).
50. K. Naito, *J. Colloid Interface Sci.*, **131**, 218 (1989).
51. Y. Nishikata, A. Morikawa, M. Kakimoto, Y. Imai, K.Nishiyama, and M. Fujihira, *Polym. J.*, **22**, 593 (1990).
52. R. H. G. Brinkhuis and A. J. Schouten, *Macromolecules*, **24**, 1487 (1991).
53. N. Hadjichristidis, S. Pispas, and G. Floudas, "*Block Copolymers: Synthetic Strategies, Physical Properties, and Applications*", Wiely Interscience, New York (2002).
54. V. Castelletto and I. W. Hamley, *Curr. Opin. Solid State Mat. Sci.*, **8**, 426 (2004).
55. M. W. Matsen and F. S. Bates, *Macromolecules*, **29**, 1091 (1996).
56. A. K. Khandpur, S. Forster, F. S. Bates, I. W. Hamley, W. Bras, S. J. Ryan, K.

Almadal, and K. Mortensen, *Macromolecules*, **28**, 8796 (1995).

57. E. Abbe, *Arch. Mikrosk. Anat.*, **9**, 413 (1873).
58. E. Abbe, *J. Roy. Microsc. Soc.*, **2**, 300 (1882).
59. E. Abbe, *J. Roy. Microsc. Soc.*, **2**, 460 (1882).
60. M. Born and E. Wolf, "*Principles of Optics*", Pergamon Press, New York (1975).
61. E. Betzig, J. K. Trautman, T. D. Haris, J. S. Weiner, and R. L. Kostelak, *Science*, **251**, 1468 (1991).
62. E. Betzig and J. K. Trautman, *Science*, **257**,189 (1992).
63. M. Ohtsu, ed., "*Near-Field Nano/Atom Optics and Technology*", Springer, Tokyo (1998).
64. M. A. Paesler and P. J. Moyer, "*Near-Field Optics: Theory, Instrumentation, and Applications*", John Wiley & Sons, New York (1996).
65. W. P. Ambrose, P. M. Goodwin, J. C. Martin, and R. A. Keller, *Science*, **265**, 364 (1994).
66. X. S. Xie and R. C. Dunn, *Science*, **265**, 361 (1994).
67. X. S. Xie, *Acc. Chem. Res.*, **29** 598 (1996).
68. B.Hecht, B. Sick, U. P. Wild, V. Deckert, R. Zenobi, O. J. F. Martin, and D. W. Pohl, *J. Chem. Phys.*, **112**, 7761 (2000).
69. L. Aigouy, A. Lahrech, S. Gresillon, H. Cory, A. C. Boccara, and J. C. Rivoal, *Opt. Lett.*, **24**, 187 (1999).
70. D. A. Vanden Bout, J. Kerimo, D. A. Higgins, and P. F. Barbara, *Acc. Chem. Res.*, **30**, 204 (1997).
71. T. Ha, T. Enderle, D. F. Ogletree, D. S. Chemla, P. R. Selvin, and S. Weiss, *Proc. natl. Acad. Sci. USA*, **93**, 6264 (1996).
72. J. Hofkens, L. Latterini, P,. Vanoppen, H. Faes, K. Jeuris, S. De Feyter, J. Kerimo, P. F. Barbara, and F. C. De Schryver, *J. Phys. Chem. B*, **101**, 10588 (1997).

73. J. Kerimo, D. M. Adams, P. F. Barbara, D. M. Kaschak, and T. E. Mallouk, *J. Phys. Chem. B*, **102**, 9451 (1998).
74. C. L. Jahncke, M. A. Paesler, and H. D. Hallen, *Appl. Phys. Lett.*, **67**, 2483 (1995).
75. S. Webster, D. N. Batchelder, and D. A. Smith, *Appl. Phys. Lett.*, **72**, 1478 (1998).
76. Y. Narita, T. Tadokoro, T. Ikeda, T. Saiki, S. Mononobe, and M. Ohtsu, *Appl. Spectrosc.*, **52**, 1141 (1998).
77. V. Deckert, D. Zeisel, R. Zenobi, and T. Vo-Dinh, *Anal. Chem.*, **70**, 2646 (1998).
78. R. M. Stockle, Y. D. Suh, V. Deckert, and S. Kawata, *Opt. Commun.*, **183**, 333 (2000).
79. S. Davy and M. Spajer, *Appl. Phys. Lett.*, **69**, 3306 (1996).
80. T. Ube, H. Aoki, S. Ito, J. Horinaka, and T. Takigawa, *Polymer*, **48**, 6221 (2007).
81. H. Aoki, M. Anryu, and S. Ito, *Polymer*, **46**, 5896 (2005).
82. H. Aoki, Y. Sakurai, S. Ito, and T. Nakagawa, *J. Phys. Chem. B*, **103**, 10553 (1999).
83. H. Aoki and S. Ito, *J. Phys. Chem. B*, **105**, 4558 (2001).
84. H. Aoki, Y. Kunai, S. Ito, H. Yamada, and K. Matsushige, *Appl. Surf. Sci.*, **18**, 534 (2002).
85. M. J. Fasolka, L. S. Goldner, J. Hwang, A. M. Urbas, P. DeRege, T. Swager, and E. L. Thomas, *Phys. Rev. Lett.*, **90**, 016107 (2003).
86. M. B. Raschke, L. Molina, T. Elsaesser, D. H. Kim, W. Knoll, and K. Hinrichs, *ChemPhysChem*, **6**, 2197 (2005).
87. A. Bhattacharya, *Prog. Polym. Sci.*, **25**, 371 (2000).
88. R. L. Clough, *Nucl. Instrum.Meth. B*, **185**, 8, (2001).
89. A. Charlesby, "*Atomic Radiation and Polymers*", Pargamon Press, Oxford (1960).
90. A. Chapiro, "*Radiation Chemistry of Polymeric Systems*", Wiley, New York (1962).
91. A. A. Miller, E. J. Lawton, and J. S. Balwit, *J. Polym. Sci.*, **14**, 503 (1954).

Part I

Chapter 2

Conformation of Single Poly(methyl methacrylate) Chains in an Ultra-Thin Film Studied by Scanning Near-Field Optical Microscopy

2.1. INTRODUCTION

Polymer thin films have been widely used in various fields (e. g., coatings and adhesives) and have been extensively explored from both the fundamental and applied points of view. The physical properties of the polymeric thin film differ from those in the three-dimensional bulk state when the thickness is less than the unperturbed dimension of the polymer chain.[1–8] The effect of the interaction between the polymer chain and the interface is a crucial factor to determine the characteristic properties of the thin film. As well as the interface effect, the effect of the reduced degree of freedom of a polymer chain due to the spatial confinement is also important. The properties of the individual chain and the interaction among the surrounding chains would be altered from the bulk state. The conformation of the single polymer chain is one of the most fundamental issues to understand the physics of the polymer thin film, therefore, it has attracted much attention and has been extensively studied by many researchers. The scaling theory predicted that the radius of gyration, R_g, of the polymer chain with the degree of polymerization of N would be expressed as $R_g \sim N^{0.5}$ for the two-dimensional chain, indicating that the two-dimensional chain would be segregated.[9] Computer simulation studies have shown that for the polymer chain restricted between two walls separated by less than the bulk R_g the chain dimension parallel to the surface is not dependent on the gap between the walls and that the value of R_g is scaled by a factor of ~ 0.5 in the two-dimensional limit.[10–15] Although the experimental method to study the

conformation of the polymer chain in the ultra-thin film is limited because of the weak signal from the low sample volume, the small angle neutron scattering (SANS) is a powerful technique to probe the chain conformation. Kraus et al. studied the chain morphology of polystyrene (PS) in the thin film of the regular and deuterated PS by SANS experiments.[16] The radius of gyration, R_g, in the parallel direction to the film surface increased with the decrease of the film thickness for the thickness range of less than $6R_g$, and a similar thickness dependence of the chain conformation in the ultra-thin film has been reported by other groups.[17,18] In contrast, Jones et al. reported the different behavior of the chain dimension of PS in the spin-cast thin film. They showed that the PS chain in an ultra-thin film takes a Gaussian conformation in the lateral dimension and the in-plane R_g is similar to that in the unperturbed state.[19,20] In contrast to the scattering techniques used in previous studies, the real-space imaging of the individual polymer chains provides one the direct information on the chain conformation in the ultra-thin film. Several studies have been performed using polymer monolayer systems as models of the polymer chain in two dimensions. Maier and R ädler studied the DNA chains adsorbed to a cationic lipid membrane.[21,22] In the highly concentrated condition, which can be regarded as the two-dimensional system, they found that the single DNA molecule took a collapsed conformation. Ito and his co-workers revealed the contracted conformation of poly(isobutyl methacrylate) in the monolayer from the energy transfer spectroscopy and the direct observation of the conformation of the single chain in a Langmuir-Blodgett film.[23,24] On the other hand, some research groups reported the expanded conformation contradictorily to the above segregated model of the two-dimensional macromolecule.[25,26] Thus, a clear picture of the chain conformation in the restricted geometry has not been obtained. The current study focuses on the effect of the spatial confinement on the chain conformation. The conformation of the single polymer chain is directly observed for the thin film with a

thickness less than the unperturbed dimension. Recently, atomic force microscopy (AFM) has been used to study single polymer chain.[27–29] The nanometric spatial resolution of AFM allows clear imaging of the single chain contour on an atomically flat substrate. However, AFM observes the isolated chain from the others at an extremely dilute condition and is applicable to measurement of the sample surface; therefore, the contour of an individual macromolecule embedded in the bulk medium cannot be tracked. Fluorescence microscopy is one of the most versatile techniques to obtain the information from the single polymer chain. The fluorescence labeling is the key feature for observation of the single chain. Since the fluorescence moieties are selectively introduced to a single chain in the bulk system, the conformation of the single fluorescence chain can be distinguished from the surrounding unlabeled ones in the fluorescence microscopy image. Therefore, the fluorescence microscopy is a powerful technique to observe the single polymer chain in the bulk system. However, the optical microscopy is not applicable to analysis of a structure less than ~ 250 nm because the spatial resolution is limited by the diffraction barrier,[30] and it has been used to observe huge biological macromolecules such as DNA.[21,22] Scanning near-field optical microscopy (SNOM) has been developed to provide the optical information with the high spatial resolution beyond the diffraction limit of light.[31–37] SNOM is a scanned probe microscopy, which uses the probe tip having an aperture smaller than the wavelength of light. The optical near-field generated at the probe end is confined in the vicinity of the aperture, which enables us to focus the light in a nanometric area. Therefore, the fluorescence imaging by SNOM is a promising technique for the observation of the contour of a single polymer chain in a bulk state.[24,38]

In this chapter, the author presents the direct measurement of the real-space image of the poly(methyl methacrylate) (PMMA) chain in thin film by SNOM. The chain conformation is discussed for the PMMA chain with a reduced degree of freedom

in the height direction by a confinement in the ultra-thin film thinner than the unperturbed chain dimension. The thickness dependence is examined in a wide thickness range of the sample film from the monolayer (~ 1 nm) to a thickness comparable to the unperturbed dimension.

2.2. EXPERIMENTAL SECTION

2.2.1. Sample Preparation

Perylene-labeled PMMA (PMMA-Pe) was synthesized by radical copolymerization of methyl methacrylate and 3-perylenylmethyl methacrylate,[39] the chemical structure of which is shown in Figure 2.1. Fractional precipitation of the obtained polymer from toluene/methanol was carried out to obtain the PMMA-Pe with a relatively narrow molecular weight distribution. The molecular weight was characterized by size exclusion chromatography (SEC) with the exclusion limit of 2×10^7 (Shodex), which was calibrated by PMMA standards (Scientific Polymer Science). The weight- and number-average molecular weights (M_w and M_n) were evaluated to be 5.14×10^6 and 4.16×10^6, respectively, and the polydispersity index, M_w/M_n, was 1.23. The molar fraction of the perylene moiety was 0.77 %, indicating that about 300 perylene molecules were tagged to each PMMA-Pe chain. A small amount of PMMA-Pe was added to a toluene solution of the unlabeled PMMA, and the resulting mixture was spin-cast on a glass plate to form a thin film. The concentration of the polymer solution and the spinning rate were adjusted to obtain the films with a thickness of 7–100 nm. The sample films were annealed at 150 °C for several days to reach the equilibrium before the SNOM measurement. A thickness of less than 7 nm was not available by the spin-coating method because of dewetting of PMMA from the substrate during the annealing. Therefore, the Langmuir-Blodgett technique was employed to

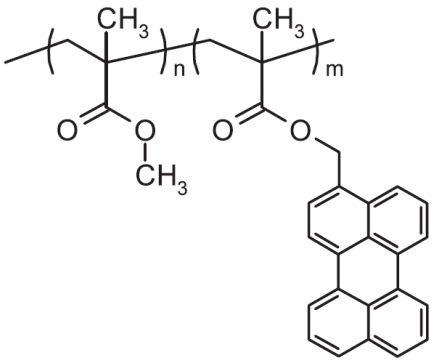

Figure 2.1. Chemical structure of perylene-labeled PMMA. The molar fraction of dye-labeled unit, m/(m + n), is evaluated to be 7.7×10^{-3} from the UV-Vis absorption.

prepare the monolayer of PMMA with the thickness of ca. 1 nm.[40] A benzene solution of the labeled/unlabeled PMMA mixture was spread dropwise on the surface of purified water (NANOpure II, Barnstead) at 20 °C. After the evaporation of the solvent the monolayer was compressed by a Teflon bar up to the surface pressure of 5 mN m^{-1} at a speed of 10 mm min^{-1}. The monolayer of the PMMA was transferred by the horizontal dipping onto the glass substrate. For the evaluation of the spatial resolution of the apparatus, the single rhodamine B molecule was used to examine the point spread function. Rhodamine B was spin-coated on a clean glass plate from the ethanol solution at the concentration of 10^{-9} M.

2.2.2. SNOM Measurement

The author used a commercially available instrument (α-SNOM, WITec) equipped with a cantilever probe with an aperture at the end of the pyramidal tip, the diameter of which was 60 nm. A He-Cd laser (442 nm, IK5351R-D, Kimmon Electric) and a diode-pumped solid state laser (532 nm, GSHG-3010, Kochi Toyonaka Giken) were used as the light sources for the excitation of perylene and rhodamine B,

respectively. The excitation laser beam was delivered to the SNOM head through a single mode optical fiber and focused on the backside of the aperture to generate the optical near-field. Besides the excitation light for the fluorescence measurement, the laser beam at 780 nm was incident on the cantilever. The reflected beam was detected with a four-segmented photo-diode to measure the cantilever deflection, from which the force between the sample and the SNOM probe was evaluated. The SNOM probe was scanned in contact with the sample surface at a constant force by regulating the vertical position of the probe tip, resulting in the surface topography image. While scanning with the SNOM probe, the fluorescence from perylene was collected with a microscope objective (60×, 0.8 NA, Nikon), passed through a long-pass filter (AELP454, Omega Optical), and detected with a photomultiplier (H8631, Hamamatsu Photonics).

2.3 RESULTS AND DISCUSSION

2.3.1. Comparison of Confocal Microscopy and SNOM Images

For the quantitative discussion of the conformation of the chain contour, the spatial resolution is a parameter of utmost importance. First, the resolution of the SNOM system was evaluated from the measurement of a single dye molecule, which can be considered as an infinitely small object compared to the size of the SNOM probe. Therefore, the observed pattern for a single molecule corresponds to the point spread function of the imaging system. The spatial resolution of the probe is defined as the full width at half maximum (FWHM) for the individual molecules. Figure 2.2 shows the fluorescence images of single rhodamine B molecules observed by the conventional confocal microscopy and SNOM. Each molecule was observed as a bright spot on the micrograph, and it showed discrete blinking and photo-bleaching during the measurement. This indicates that the observed bright spots correspond to the individual

dye molecules. The single rhodamine molecule in the confocal image was observed as a circular spot with a diameter of 300 nm due to the diffraction-limited spatial resolution of about the half of its excitation wavelength. On the other hand, SNOM enables one to observe the individual molecules as small as 75 nm, which is the sufficiently high spatial resolution to observe the conformation of the single polymer chain with a relatively high molecular weight. Since the resolution is greatly dependent on the probe tip, all of the samples were observed using the identical probe used to obtain the SNOM image shown in Figure 2.2b.

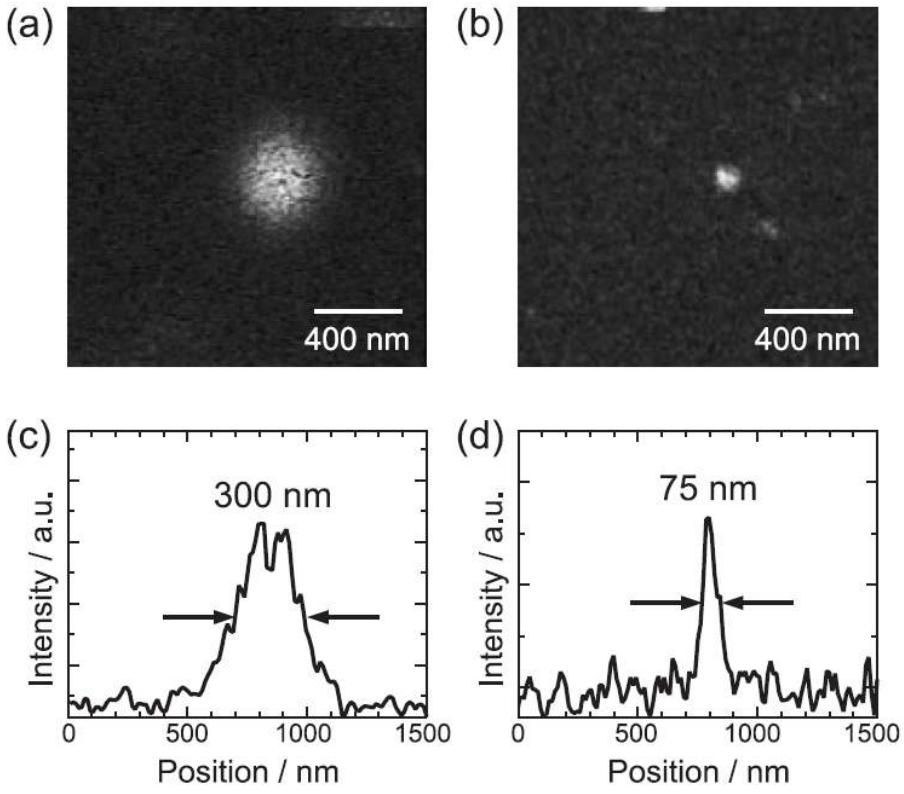

Figure 2.2. Fluorescence SNOM images for the single rhodamine B molecule observed by confocal microscopy (a) and SNOM (b). The fluorescence intensity profiles are shown in the lower panels c and d for the confocal and SNOM images, respectively. The rhodamine B molecule in panel b was observed as circular spots with the diameter of 75 nm, which is the spatial resolution of $\lambda/7$, where λ is the excitation wavelength.

2.3.2. SNOM Imaging of a Single PMMA Chain

Figure 2.3 shows the fluorescence SNOM image of the PMMA thin films with a thickness of 15 nm, where the perylene-labeled PMMA chains were dispersed in an unlabeled polymer matrix at different concentrations. The topographic image obtained simultaneously showed a smooth and featureless surface with a root-mean-squared roughness less than 0.3 nm (the image is not shown here), indicating a homogeneous thin film without any defect. The thickness of the sample film was evaluated from the height difference between the sample surface and the substrate exposed by scratching the film. Since the optical near-field generated from the SNOM probe penetrates into the sample film, the labeled PMMA chain embedded in the unlabeled PMMA matrix can be selectively imaged. At a high concentration of the labeled PMMA, the fluorescence signal of the labeled chain was observed uniformly from the whole area. At an extremely low concentration, the labeled polymer was observed as discrete bright spots as shown in Figure 2.3, and the number of fluorescence spots in the SNOM image decreased with the decrease of the concentration of the labeled polymer.

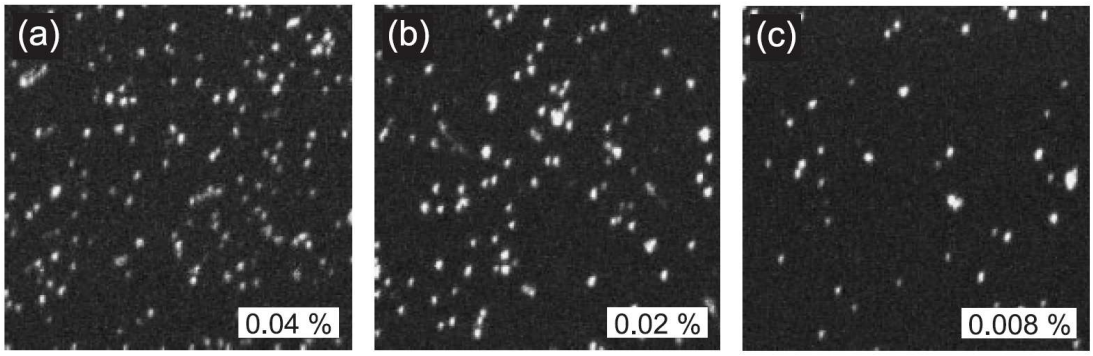

Figure 2.3. Fluorescence SNOM images of the PMMA-Pe chains dispersed in the unlabeled PMMA matrix. The concentration of the labeled chain is 0.04 (a), 0.02 (b), and 0.008 % (c). The observed area was 20 × 20 μm^2.

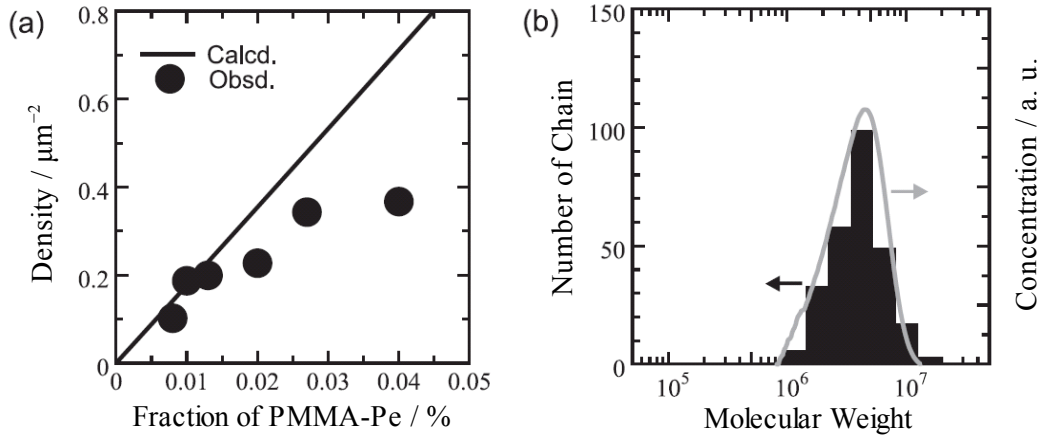

Figure 2.4. Number density of the observed fluorescence spot and the calculated value of the PMMA-Pe chain (a) and the histogram of the integrated fluorescence intensity for each PMMA-Pe chain (b). In panel a, the closed circles and the solid line represent the observed and calculated values, respectively. In panel b, the thick bars are the intensity histogram, and the gray solid curve exhibits the molecular weight distribution observed by SEC, where the chain number concentration was plotted against the molecular weight.

Each fluorescence spot was confirmed to correspond to the individual PMMA-Pe chain. Figure 2.4a shows the relationship between the dye-labeled chain fraction in the PMMA film and the number of fluorescence spots in a unit area. The number of perylene-labeled PMMA chains can be estimated from the concentration of the labeled PMMA in the unlabeled PMMA matrix. The solid line represents the number of single perylene-labeled PMMA chains in a unit area of 1 × 1 μm^2 calculated from the concentration of the labeled polymer. In a low concentration range, the number of observed fluorescence spots was in good agreement with the calculated value for the PMMA-Pe chain. This indicates that each fluorescence spot corresponds to the individual PMMA-Pe chain. For the sample with a thickness of 15 nm, at a concentration higher than 0.015 % the density of the fluorescence spot was less than the

calculated line as shown in Figure 2.4a; therefore, for the 15-nm thick film, the observation of the single chain was performed under a concentration condition of 0.015 %. This threshold concentration is dependent on the film thickness. Even at the same concentration of PMMA-Pe in the unlabeled matrix, the number of labeled chains in an observed unit area is proportional to the sample thickness. Hence, the concentration dependence of the area density of the fluorescence spot was carefully examined for each film thickness, and the SNOM measurement was performed at a sufficiently low concentration of the labeled chain to ensure the single chain observation.

Moreover, the integrated fluorescence intensity from each spot was examined. The number of perylene molecules in the single PMMA-Pe chain is proportional to the molecular weight, because the perylene moiety was randomly introduced to the polymer chain. The low fraction of the dye moiety in each chain results in the negligible interaction among the perylene molecules. Thus the fluorescence intensity from the single chain is proportional to its molecular weight:

$$I_i = kM_i, \tag{2.1}$$

where I_i and M_i are the integrated fluorescence intensity and the molecular weight for the i-th chain, respectively, and k is a constant determined by the fluorescence quantum yield of perylene, the detection efficiency of the signal collection, etc. Therefore, assuming that the bright spot corresponds to the single chain, the histogram of the fluorescence intensity corresponds to the molecular weight distribution. Figure 2.4b shows the fluorescence intensity histogram and the molecular weight distribution observed by SEC. The emission intensity histogram and the molecular weight distribution are in good agreement. These data also support the single PMMA-Pe chain observation in the SNOM image, indicating that the molecular weight of the single chain can be evaluated by the SNOM measurement.

2.3.3. Single Chain Conformation in the Various Film Thickness

Figure 2.5 shows the high-resolution SNOM images of the single PMMA-Pe chains in the thin film. The molecular weight of each chain was estimated to be ca. 4.0 × 10^6 from the comparison between the fluorescence intensity and the molecular weight distribution curve shown in Figure 2.4b. In Figure 2.5, the polymer chains with similar molecular weight showed various shapes, and a part of the chains took a stretched conformation because of the broad conformational distribution of the flexible PMMA chain. The chain dimension in the *x*-*y* plane weighted by the fluorescence intensity, R_{xy}, was evaluated for each PMMA-Pe chain in the SNOM image according to the following equation.

$$R_{xy}^2 = \frac{\sum_j I_j (\mathbf{r}_j - \mathbf{r}_0)^2}{\sum_j I_j}, \tag{2.2}$$

where $\mathbf{r}_j$ and I_j are the position vector and the fluorescence intensity for the *j*-th pixel in the SNOM image, and $\mathbf{r}_0$ is the position vector of the center of mass defined as

$$\mathbf{r}_0 = \frac{\sum_j I_j \mathbf{r}_j}{\sum_j I_j}. \tag{2.3}$$

Since the dye moiety was randomly introduced in the PMMA-Pe chain as mentioned above, the fluorescence intensity at each pixel is proportional to the chain segment number therein. Therefore, R_{xy} is corresponding to the radius of gyration of the PMMA-Pe chain projected in the *x*-*y* plane parallel to the film surface. For example, R_{xy} for the PMMA chains shown in Figure 2.5a-5d is estimated to be 122, 160, 180, and 256 nm, respectively.

Here the author discusses the thickness dependence of the chain dimension in the film plane. At first, the relationship between the unperturbed dimension of the PMMA chain and the thickness range of the film used in the current work should be

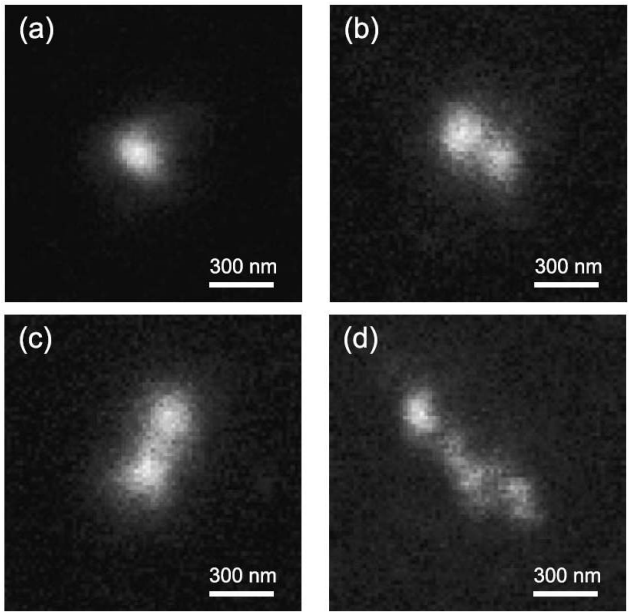

Figure 2.5. SNOM images of the single PMMA-Pe chains in an ultra-thin film. The scanned area is 1.4 × 1.4 μm^2 for each image. The molecular weight (M) and the value of R_{xy} for each chain were evaluated as follows: (a) $M = 4.2 \times 10^6$ and $R_{xy} = 122$ nm; (b) $M = 4.2 \times 10^6$ and $R_{xy} = 160$ nm; (c) $M = 4.0 \times 10^6$ and $R_{xy} = 180$ nm; (d) $M = 3.6 \times 10^6$ and $R_{xy} = 256$ nm.

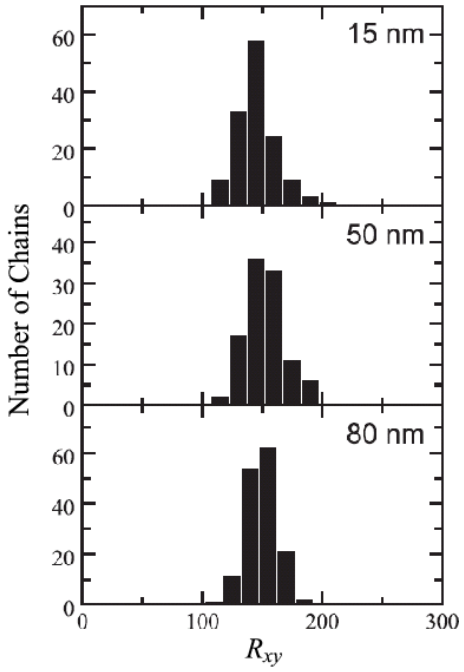

Figure 2.6. Histogram of the lateral chain dimension for the PMMA-Pe chains in the ultra-thin films with the thickness of 15, 50, and 80 nm. The PMMA chains with a molecular weight of 4 × 10^6 were selected in the SNOM images and analyzed to construct the histogram.

considered. By a SANS study, O'Reilly et al. showed that the radius of gyration of PMMA in the bulk state can be expressed by an empirical equation: $R_g = 0.025 M_w^{0.5}$ / nm.[41] The PMMA sample used here is estimated to have an R_g of 56 nm considering the molecular weight. The maximum thickness of the spin-cast film used here is 100 nm, which is the comparable to the unperturbed chain dimension in the bulk state. Figure 2.6 shows the histogram of R_{xy} for the PMMA-Pe chain in the films with a thickness of 15, 50, and 80 nm. This corresponds to the probability distribution function of the chain dimension projected to the *x*-*y* plane, which cannot be obtained from scattering experiments. The histogram for each thickness has a peak value at R_{xy} of 140 nm and the width of the distribution of about 30 nm. Figure 2.7 summarizes the thickness dependence of the average value of R_{xy}. The filled circles in Figure 2.7 are the data for the ultra-thin film samples with thickness range of 1–100 nm. The results clearly

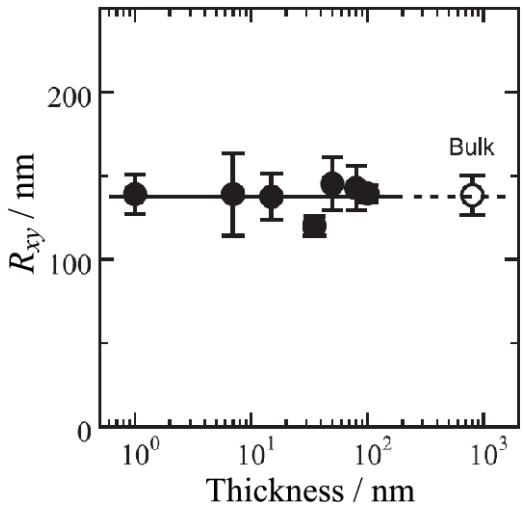

Figure 2.7. Thickness dependence of the chain dimension of PMMA in the parallel direction to the film surface. The filled circle indicates the value of R_{xy} for the ultra-thin film. The error bar is the standard deviation evaluated from the histogram of R_{xy}. The open circle represents the data for the PMMA-Pe chains in the bulk state.

indicate that chain dimension in the lateral direction is not dependent on the film thickness in the ultra-thin film region. Now the author compares R_{xy} between the ultra-thin film and the bulk state. For the measurement of the PMMA chain in an unperturbed conformation, a sample thicker than several hundred nanometer should be used because of the large molecular weight of PMMA-Pe used here. However, the SNOM imaging of a thick sample is practically difficult due to the limited penetration depth of the near-field illumination from the film surface. Therefore, the author prepared the thick PMMA sample (1 μm) where the PMMA-Pe chains were located near the surface in an unperturbed conformation.[41] The value of R_{xy} in the bulk state was evaluated to be 138 nm. The open circle in Figure 2.7 is R_{xy} in the three-dimensional bulk. As clearly shown in this figure, the value of R_{xy} in bulk is almost the same value as that in the ultra-thin films, indicating that the chain dimension in the parallel directions to the film surface is not dependent on the film thickness. Although the polymer chain is spatially restricted in the height direction, R_{xy} in the ultra-thin films is a similar value in the unperturbed state. This result is consistent with the previous studies on the conformation of PS using SANS.[19,20] The recent Monte Carlo simulation showed the stretched dimension by ~ 40 % in the parallel direction to the film surface in the quasi-two-dimensional region with the thickness less than approximately $R_g/3$.[15,43] In the current direct observation of the single chain, it should be noted that the similar value of R_{xy} was obtained for the monolayer sample, where the PMMA chain was strictly restricted in a two-dimensional plane, suggesting that the PMMA chain takes a contracted conformation in the two-dimensional state.

In a three-dimensional bulk state, the polymer chain takes a random coil conformation. In terms of the conformation of an individual chain, the single PMMA chain with a molecular weight of 10^6 occupies the space larger than 100 nm. Considering the molecular volume of the single chain, there is much free space to allow

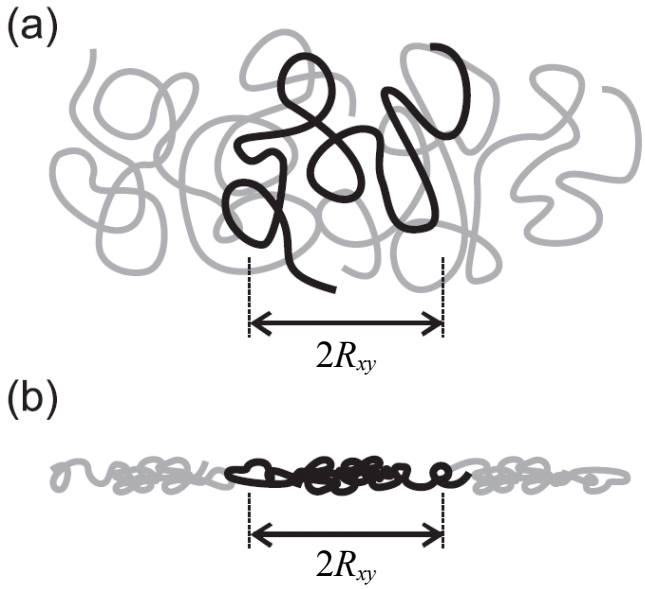

Figure 2.8. Schematic drawing of the chain conformations in the bulk (a) and ultra-thin film (b). To clarify the contour of the single chain, one chain is described as the solid curve. Few interlacements among the chains exist in the ultra-thin film, whereas there are a lot of interlacements in the bulk state.

the intrusion of the neighboring chains as schematically shown by the solid contour in Figure 2.8a. In the bulk system, such free space is filled with the surrounding chains (the gray curves in Figure 2.8a), resulting in interlacement of the polymer chains. Under the spatial confinement in the ultra-thin film, on the other hand, the direct observation of the single PMMA chain revealed that an in-plane dimension was similar to that in the bulk state in spite of the spatial confinement in the height direction, suggesting the decrease in the pervaded volume of a single chain. Since the mass density of the thin film is almost the same as that in the bulk state,[44] the single chain does not have enough free space occupied by the neighboring chains as shown in Figure 2.8b. Consequently, the interlacement among the surrounding polymer chains is reduced in the ultra-thin film.[9,43,45] The direct observation of the single PMMA chain

indicates little interaction among the polymer chains in the ultra-thin film. Such a characteristic conformation in the confined geometry results in unique macroscopic properties different from those of the bulk material.[8,46]

2.4. CONCLUSION

The real-space imaging by SNOM revealed the conformation of the single PMMA chain confined in the ultra-thin film, the thickness of which was less than the unperturbed chain dimension. In the thickness range of 1–100 nm, the radius of gyration in the direction normal to the confinement was not significantly different from the unperturbed dimension in the three-dimensional bulk state. This result indicates that the polymer chain restricted in an ultra-thin film has few interlacements with the surrounding chains.

References and Note

1. J. L. Keddie, R. A. L. Jones, and R. A. Cory, *Faraday Discuss.*, **98**, 219 (1994).
2. J. L. Keddie, R. A. L. Jones, and R. A. Cory, *Europhys. Lett.*, **27**, 59 (1994).
3. T. Kajiyama, K. Tanaka, and A. Takahara, *Macromolecules*, **30**, 280 (1997).
4. K. Tanaka, A. Taura, S. R. Ge, A. Takahara, and T. Kajiyama, *Macromolecules*, **29**, 3040 (1996).
5. K. Tanaka, Y. Tsuchimura, K. Akabori, F. Ito, and T. Nagamura, *Appl. Phys. Lett.*, **89**, 061916 (2006).
6. O. K. C. Tsui and H. F. Zhang, *Macromolecules*, **34**, 9139 (2001).
7. Y. Grohens, L. Hamon, G. Reiter, A. Soldera, and Y. Holl, *Eur. Phys. J. E*, **8**, 217 (2002).
8. L. Si, M. V. Massa, K. Dalnoki-Veress, H. R. Brown, and R. A. L. Jones, *Phys. Rev. Lett.*, **94**, 127801 (2005).
9. P. G. de Gennes, "*Scaling Concepts in Polymer Physics*", Cornell University Press, Ithaca, New York (1979).
10. S. K. Kumar, M. Vacatello, and D. Y. Yoon, *J. Chem. Phys.*, **89**, 5206 (1988).
11. J. Reiter, G. Zifferer, and O. F. Olaj, *Macromolecules*, **22**, 3120 (1989).
12. I. A. Bitsanis and G. ten Brinke, *J. Chem. Phys.*, **99**, 3100 (1993).
13. A. Yethiraj, *Macromolecules*, **36**, 5854 (2003).
14. M. Müller, *J. Chem. Phys.*, **116**, 9930 (2002).
15. A. Cavallo, M. Müller, J. P. Wittmer, A. Johner, and K. Binder, *J. Phys.: Condens. Matter*, **17**, S1697 (2005).
16. J. Kraus, P. Müller-Buschbaum, T. Kuhlmann, D. W. Schubert, and M. Stamm, *Europhys. Lett.*, **49**, 210 (2000).
17. A. Brulet, F. Boue, A. Menelle, and J. P. Cotton, *Macromolecules*, **33**, 997 (2000).
18. K. Shuto, Y. Oishi, T. Kajiyama, and C. C. Han, *Macromolecules*, **26**, 6589 (1993).

19. R. L. Jones, S. K. Kumar, D. L. Ho, R. M. Briber, and T. P. Russell, *Nature*, **400**, 146 (1999).
20. R. L. Jones, S. K. Kumar, D. L. Ho, R. M. Briber, and T. P. Russell, *Macromolecules*, **34**, 559 (2001).
21. B. Maier and J. O. Rädler, *Phys. Rev. Lett.*, **82**, 1911 (1999).
22. B. Maier and J. O. Rädler, *Macromolecules*, **33**, 7185 (2000).
23. N. Sato, Y. Osawa, S. Ito, and M. Yamamoto, *Polym. J.*, **31**, 488 (1999).
24. H. Aoki, M. Anryu, and S. Ito, *Polymer*, **46**, 5896 (2005).
25. X. R. Wang and V. J. Foltz, *J. Chem. Phys.*, **121**, 8158 (2004).
26. W. A. Kuhlman, E. A. Olivetti, L. G. Griffith, and A. M. Mayes, *Macromolecules*, **39**, 5122 (2006).
27. S. S. Sheiko, *Adv. Polym. Sci.*, **151**, 61 (2000).
28. J. Kumaki and T. Hashimoto, *J. Am. Chem. Soc.*, **120**, 423 (1998).
29. J. Kumaki, T. Kawauchi, and E. Yashima, *Macromolecules*, **39**, 1209 (2006).
30. E. Abbe, *Arch. Mikrosk. Anat.*, **9**, 413, (1873).
31. E. Betzig and J. K. Trautman, *Science*, **257**, 189 (1992).
32. M. Ohtsu, ed., "*Near-Field Nano/Atom Optics and Technology*", Springer, Tokyo (1998).
33. M. A. Paesler and P. J. Moyer, "*Near-Field Optics: Theory, Instrumentation, and Applications*", John Wiley & Sons, New York (1996).
34. R. C. Dunn, *Chem. Rev.*, **99**, 2891 (1999).
35. H. Aoki, Y. Sakurai, S. Ito, and T. Nakagawa, *J. Phys. Chem. B*, **103**, 10553 (1999).
36. H. Aoki and S. Ito, *J. Phys. Chem. B*, **105**, 4558 (2001).
37. H. Aoki, T. Hamamatsu, and S. Ito, *Appl. Phys. Lett.*, **84**, 356 (2004).
38. S. Ito and H. Aoki, *Adv. Polym. Sci.*, **182**, 131 (2005).
39. H. Aoki, S. Tanaka, S. Ito, and M. Yamamoto, *Macromolecules*, **33**, 9650 (2000).

40. G. Gabrielli, M. Puggelli, and P. Baglioni, *J. Colloid Interface Sci.*, **86**, 485 (1982).
41. J. M. O'Reilly, D. M. Teegarden, and G. D. Wignall, *Macromolecules*, **18**, 2747 (1985).
42. The unlabeled PMMA was cast from the toluene solution to form a 1-μm thick film on a glass substrate. A spin-cast film containing the labeled PMMA with a thickness of 70 nm was floated on pure water and transferred onto the thick film of the unlabeled PMMA. Then it was covered with the 40-nm spin cast film of the unlabeled PMMA. The sample film was annealed at 150 °C for a few days to reach equilibrium. From a separate experiment, the translational diffusion coefficient is estimated to be 10^{-19} cm^2 s^{-1}; therefore, the labeled PMMA chain is located near the surface with an equilibrium conformation.
43. H. Meyer, T. Kreer, A. Cavallo, J. P. Wittmer, and J. Baschnagel, *Eur. Phys. J. Special Topics*, **141**, 167 (2007).
44. W. E. Wallace, N. C. B. Tan, W. L. Wu, and S. Satija, *J. Chem. Phys.*, **108**, 3798 (1998).
45. H. R. Brown and T. P. Russell, *Macromolecules*, **29**, 798 (1996).
46. N. Sato, S. Ito, and M. Yamamoto, *Macromolecules*, **31**, 2673 (1998).

Chapter 3

Conformational Relaxation of Single Polymer Chains Confined in Two-Dimensional Plane Studied by Scanning Near-Field Optical Microscopy

3.1. INTRODUCTION

Polymer monolayers have attracted much attention because they allow one to fabricate well-defined nanometric architectures with thermal durability compared with those made from conventional long-chain fatty acids.[1] Poly(alkyl methacrylate) is well-known to form a stable monolayer at air/water interface because it has an amphiphilic ester group in each monomer unit.[2] The main chain is constrained on the water surface, resulting in a restricted conformation in quasi-two dimensions. Thermal stability of the polymer monolayer is of crucial importance from the viewpoint of the practical application of such highly controlled molecular assemblies. However, the two-dimensional conformation of the polymer chains in a monolayer is entropically unstable compared to the three-dimensional conformation. Therefore, they suffer inevitably from the thermal relaxation after the deposition on solid substrates. In the past few decades, the thermal stability of LB films has been examined by small-angle X-ray scattering,[3,4] X-ray reflectivity,[5] polarized infrared spectroscopy,[6,7] optical second-harmonic generation method,[8] and the energy-transfer technique.[9] Several research groups reported the structural relaxation of polymer LB films in nanometer dimensions by thermal treatment and suggested that the chain conformation was rearranged from a two-dimensionally restricted form to a three-dimensional equilibrium conformation by the local motion of polymer segments.[5,10,11]

In contrast to the methods used in the previous studies, the direct observation of the individual chains is expected to provide clear evidences on the chain conformation and could be helpful to understand the previous results obtained from the ensemble averaged measurements. Recently, several studies on the direct observation of a single polymer chain by atomic force microscopy (AFM) have been reported. The high spatial resolution of AFM enables us to observe the contour of a single polymer chain.[12-14] Since AFM detects only the topographic information of the sample surface, it is unable to observe the single polymer chain embedded in a bulk medium. To observe single chain conformation, we must employ a novel technique to distinguish the objective polymer chain from the surrounding ones. The fluorescence labeling is a promising method to overcome this requirement.[15,16] The introduction of a small amount of fluorescence chromophores into a polymer chain enables us to image the single fluorescent chains owing to the high sensitivity of fluorescence detection. However, the spatial resolution of a conventional fluorescence microscope is limited to a half of the excitation wavelength by the diffraction barrier.[17] This has limited its application for the single chain imaging except huge bio-macromolecules such as DNA.[15,16] Scanning near-field optical microscopy (SNOM) has been developed as a novel technique for achieving a high spatial resolution beyond the diffraction limit of light.[18-20] SNOM is one of scanning probe microscopy, which are equipped with the probe tip having an aperture smaller than the wavelength of light. The near-field light emanating from such a small aperture is confined in the vicinity of the probe tip end, which allows us to illuminate the nanometric space under the sample surface. Therefore SNOM is suitable to investigate the polymer chain conformations in a bulk medium.[21,22]

In this chapter, the author presents the direct measurement of the real-space image of an individual poly(methyl methacrylate) (PMMA) chain by SNOM and discusses the conformational relaxation of the PMMA chains in a monolayer by thermal

treatment on the basis of the annealing time dependence of the chain dimension and the segment distribution. The SNOM observation in the depth direction is also carried out and the thermally-induced rearrangement of the segment distribution is investigated in comparison with the translational diffusion of the whole chain.

3.2. EXPERIMENTAL SECTION

3.2.1. Sample Preparation

Perylene-labeled poly(methyl methacrylate) (PMMA-Pe) was synthesized by radical copolymerization of methyl methacrylate (Wako) and 3-perylenyl methyl methacrylate.[23] The details on the synthesis are written in chapter 2. The weight average molecular weight, M_w, and the molecular weight distribution, M_w/M_n, were 3.0×10^6 and 1.3, respectively. The molar fraction of the perylene moiety introduced in a PMMA chain was evaluated to be 0.84 % from UV-Vis absorption measurement. PMMA-Pe was dispersed in a monolayer of unlabeled PMMA ($M_w = 2.2 \times 10^6$, American Polymer Standards) in concentrations from 0.1 to 0.5 wt% to observe the individual labeled chains separately. A mixed benzene solution of the labeled and unlabeled PMMA at a total polymer concentration of 0.1 g L^{-1} was spread on ultra pure water (NANO Pure II, Barnstead) at 20 °C to form a monolayer on the water surface. The monolayer was compressed to a surface pressure of 5 mN m^{-1} and transferred onto a 40-μm thick film of unlabeled PMMA by the horizontal dipping method, which was prepared by casting from a 1,2-dichloroethane solution on a clean glass plate. The sample film was annealed at 170 °C in vacuo. The structure of a sample film is illustrated in Scheme 3.1.

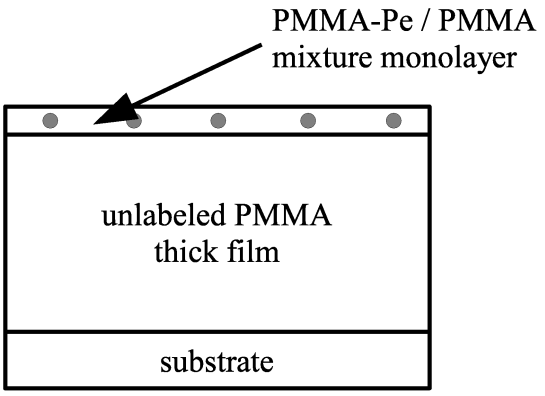

Scheme 3.1. Schematic illustration of the structure of the sample film used in this study. The ratio of PMMA-Pe/PMMA mixture ranges from 0.1 to 0.5 wt%.

3.2.2. SNOM Measurement

SNOM imaging was performed by a commercially available instrument (α-SNOM, WITec) using a cantilever SNOM probe with a 60-nm aperture. A 438-nm laser beam (BCL-015-440, CrystaLaser) was coupled into the sub-wevelength aperture to generate the optical near-field for the excitation of the perylene moiety in the PMMA-Pe chain. The fluorescence from the sample was collected by a microscope objective (60×, 0.80NA, Nikon) from the backside of the substrate and guided to a photomultiplier (H8631, Hamamatsu Photonics) through a long-pass filter (AELP 454, Omega Optical). The SNOM probe was scanned with a contact mode on the sample surface, and the height image of the surface was simultaneously obtained with the fluorescence image. All SNOM measurements were carried out using the same probe in an ambient condition.

3.3. RESULTS AND DISCUSSION

3.3.1. SNOM Imaging of a Single PMMA Chain in the Lateral Directions

Figure 3.1a shows the fluorescence SNOM image of a sample film before annealing. The individual perylene-labeled PMMA chains embedded in the unlabeled PMMA monolayer were observed as bright spots in the fluorescence image. The height image of the sample surface for the same area showed no topographic feature, indicating the homogeneous deposition of the monolayer on the thick PMMA film. Each fluorescence spot corresponds to a single PMMA-Pe chain, being confirmed from the statistical analysis.[21] The SNOM images in Figure 3.1 show a broad distribution of the fluorescence intensity from the single chain. This variation in the signal intensity is due to the molecular weight distribution of the sample polymer. The number of dye moieties in a labeled chain is proportional to the length of the chain yielded by random copolymerization of methyl methacrylate and 3-perylenyl methyl methacrylate,[21] resulting in the fluorescence intensity proportional to the molecular weight. Figure 3.1b depicts the fluorescence SNOM image after 48 h annealing at 170 °C. In this large field image, the shapes and sizes of the spots after annealing are similar to those before annealing.

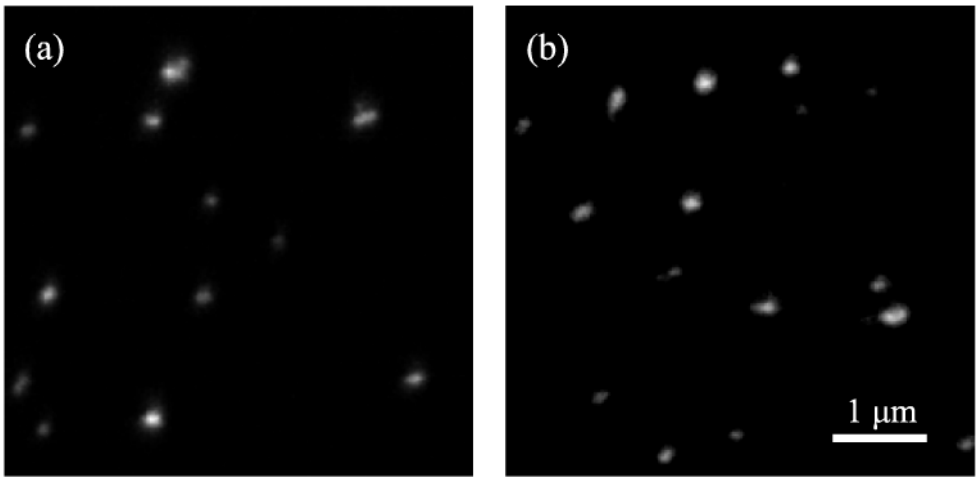

Figure 3.1. Fluorescence SNOM images of the single PMMA chains dispersed in the unlabeled PMMA matrix before (a) and after 48 h annealing (b) at 170 °C.

In order to obtain more detailed information about the chain conformation, the dimension of the single chain in the close-up image was analyzed. Since the fluorescent moiety is randomly introduced along the PMMA-Pe chain as mentioned above, the fluorescence intensity at each pixel corresponds to the segment density therein. In the SNOM measurement, the optical near-field penetrates below the sample surface by a few hundred nanometers. Therefore, the chain conformation in the SNOM image is given as the projection of the individual chain onto the film plane. The normalized second moment tensor of the fluorescence intensity distribution, **M**, is expressed as

$$\mathbf{M}=\begin{pmatrix} M_{xx} & M_{xy} \\ M_{yx} & M_{yy} \end{pmatrix}, \tag{3.1}$$

$$M_{xx}=\frac{1}{I_0}\sum_j I_j(x_j-x_0)^2, \quad M_{yy}=\frac{1}{I_0}\sum_j I_j(y_j-y_0)^2,$$

$$M_{xy}=M_{yx}=\frac{1}{I_0}\sum_j I_j(x_j-x_0)(y_j-y_0),$$

where I_0 is the total intensity from the single polymer chain, and (x_j, y_j) and (x_0, y_0) are the position of the j-th pixel and the center of mass in the orthogonal coordinate system. The coordinate of the intensity-weighted center of mass of the single polymer chain is

$$x_0=\frac{1}{I_0}\sum_j I_j x_j, \quad y_0=\frac{1}{I_0}\sum_j I_j y_j. \tag{3.2}$$

The tensor **M** is a parameter related to the polymer conformation.[24] The trace of **M** corresponds to the squared radius of gyration for the projection of the PMMA-Pe chain in the x-y plane;

$$R_{xy}^2=\mathrm{tr}(\mathbf{M}). \tag{3.3}$$

Figure 3.2 shows the histograms of R_{xy} for 100 chains in the PMMA monolayer at the annealing times of 0 and 48 h. The histogram before annealing has a peak at 130 nm and the standard deviation of 28 nm. After annealing of 48 h, the distribution function of R_{xy} showed a peak at 130 nm with the standard deviation of 30 nm. Figure 3.3 summarizes the annealing time dependence of the average value of R_{xy}, clearly showing that the chain dimension in the lateral direction is not dependent on the annealing time. In terms of the ensemble averaged R_{xy} value, it seems that the chain conformation was not altered by annealing above the glass transition temperature.

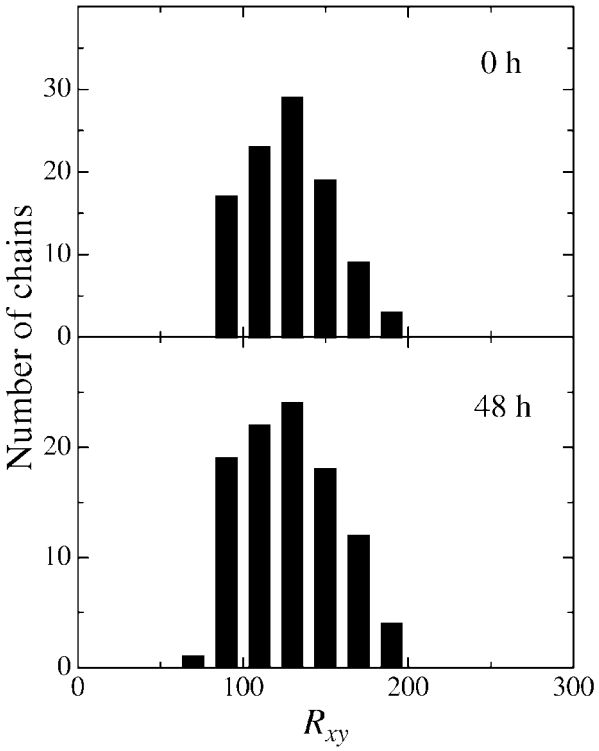

Figure 3.2. Histogram of the lateral chain dimension for the PMMA chains before and after annealing.

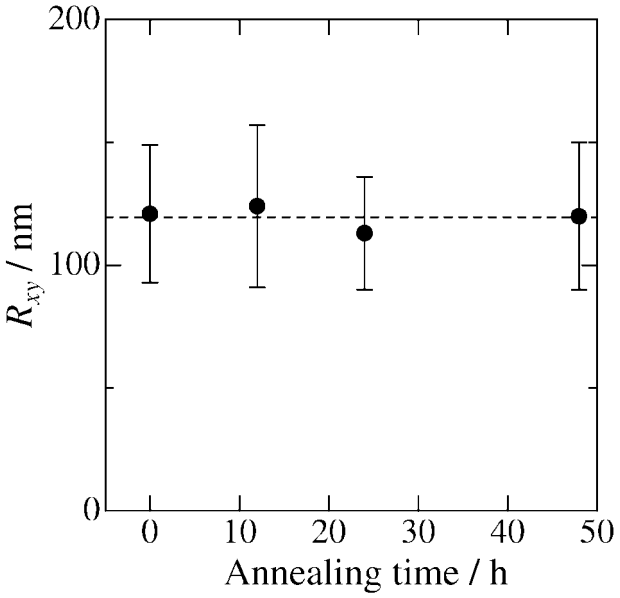

Figure 3.3. Annealing time dependence of the chain dimension of PMMA in the parallel direction to the film surface. The error bar indicates the standard deviation.

For the more detailed discussion, the author observed some polymer chains before and after annealing as depicted in Figure 3.4. On the thermal activation, R_{xy} for the PMMA chains varied from 89 to 87 nm for the chain A in Figure 3.4, 209 to 189 nm for B, and 177 to 174 nm for C. The variation in R_{xy} for the most of the polymer chains was less than 10 nm and the largest change of R_{xy} for the same single polymer chains before and after annealing was 20 nm, which is smaller than the standard deviation of the conformational distribution. In terms of R_{xy}, the chain dimension in the lateral direction was not altered significantly. However, the spatial distribution of the segment density was different between the chains before and after annealing. The brightness distribution before annealing for the chains B and C looks homogeneous in the ellipsoidal area, but after annealing it is enhanced at the center. In order to discuss the segment distribution for each polymer chain, the author introduced the two-dimensional kurtosis, K,[25,26] which is related to the forth moment of the intensity distribution defined as

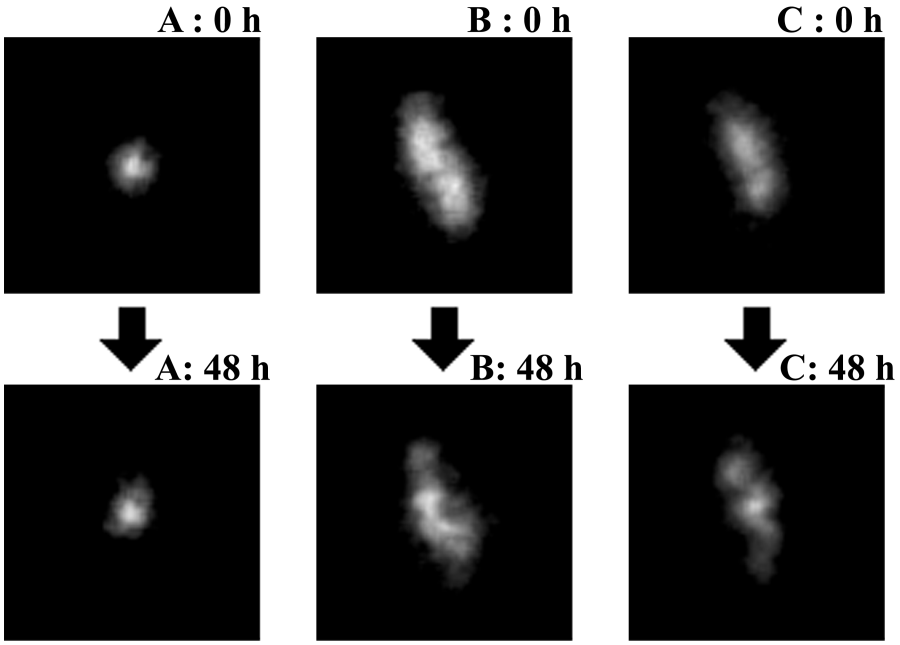

Figure 3.4. Fluorescence SNOM images of the same single PMMA chains before (the upper side) and after (the lower side) annealing for 48 h. Chain A : R_{xy} = 89 nm, K = −1.29 (upper) and R_{xy} = 87 nm; K = −1.22 (lower). Chain B : R_{xy} = 209 nm; K = −1.77 (upper) and R_{xy} = 189 nm; K = −1.28 (lower). Chain C : R_{xy} = 177 nm; K = −1.52 (upper) and R_{xy} = 174 nm; K = −1.05 (lower). The dimension of all images is 1.5 × 1.5 μm.

$$K=\frac{1}{(1-\rho^2)^2}\left\{\frac{M_{xxxx}}{M_{xx}^2}+\frac{M_{yyyy}}{M_{yy}^2}+2\frac{M_{xxyy}}{M_{xx}M_{yy}}+4\rho\left(\rho\frac{M_{xxyy}}{M_{xx}M_{yy}}-\frac{M_{xxxy}}{\sqrt{M_{xx}^3M_{yy}}}-\frac{M_{xyyy}}{\sqrt{M_{xx}M_{yy}^3}}\right)\right\}-8\,, \qquad (3.4)$$

where

$$M_{xxxx}=\frac{\sum_j I_j(x_j-x_0)^4}{\sum_j I_j},\quad M_{xxxy}=\frac{\sum_j I_j(x_j-x_0)^3(y_j-y_0)}{\sum_j I_j},\quad M_{xxyy}=\frac{\sum_j I_j(x_j-x_0)^2(y_j-y_0)^2}{\sum_j I_j},$$

$$M_{xyyy}=\frac{\sum_j I_j(x_j-x_0)(y_j-y_0)^3}{\sum_j I_j},\quad M_{yyyy}=\frac{\sum_j I_j(y_j-y_0)^4}{\sum_j I_j},\quad \rho=\frac{M_{xy}}{\sqrt{(M_{xx}M_{yy})}}.$$

The kurtosis parameter is a measure of the "sharpness" relative to the Gaussian distribution; a higher value of K indicates a narrower distribution, while a lower value of K presents a broader distribution compared to a Gaussian function. After the annealing for 48 h, the K parameter increased from −1.29 to −1.22 for the chain A, −1.77 to −1.28 for B, and −1.52 to −1.05 for C. The increase in K for the PMMA chains indicates that the thermally induced conformational relaxation took place and the chain segment was rearranged to a Gaussian distribution around the center of mass of the polymer chain. This result suggests that the two-dimensional conformation of the PMMA chain in a monolayer expands to the entropically stable three-dimensional random coil conformation, while keeping the chain dimension, R_{xy}, in the lateral directions.

3.3.2. SNOM Measurement of the Cross-Section of the Sample Film

In order to discuss the conformational change of the PMMA chains confined in a monolayer toward the bulk substrate, the cross-section of the specimen was observed by SNOM. The sample film was removed from the glass substrate and sliced vertically to the surface plane with a microtome. Figure 3.5 shows the fluorescence SNOM images and the depth profiles of the ultra-thin specimen (ca. 70 nm in thickness). Just after the deposition of the monolayer, the PMMA-Pe chain was localized at the sample surface as a single molecule monolayer with the thickness of ca. 1 nm.[27] The SNOM image showed the much broader intensity profile compared to the actual thickness of the PMMA monolayer due to the spatial resolution of the apparatus. The SNOM image results from the convolution of spatial distribution of the fluorescent object and the point spread function (PSF) of the microscope. Because the thickness of the PMMA monolayer is negligible compared to the resolution of SNOM, the profile at t = 0 corresponds to the PSF of SNOM, and it was well fitted to a Gaussian profile with the

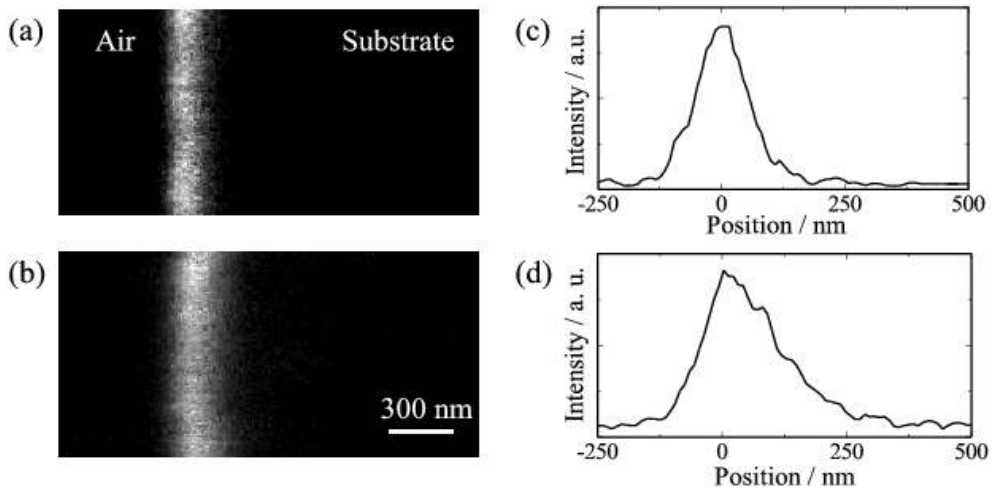

Figure 3.5. Fluorescence SNOM images observed from the direction normal to the sample surface. The annealing time is 0 h (a) and 48 h (b). The fluorescence intensity profiles are shown in the right panels (c) and (d) for the 0 h annealing time (a) and 48 h (b), respectively.

full width at half maximum (FWHM) of 100 nm. On the other hand, the SNOM image after annealing showed an asymmetric profile, indicating that the PMMA-Pe segments on the surface diffused into the bulk substrate. Here, the fluorescence intensity profiles at the various annealing time were analyzed. At first, we defined the z-axis in the depth direction toward the bulk substrate and set the origin at the position of the maximum fluorescence intensity. The distribution of the PMMA-Pe chain along the z-axis was modeled as

$$\rho(z)=\begin{cases}\rho_0\exp\left(-\dfrac{z^2}{2\sigma^2}\right) & (z\geq 0)\\ 0 & (z<0)\end{cases} \tag{3.5}$$

where σ^2 shows the spatial distribution of the chain segment of PMMA-Pe. The fluorescence intensity was fitted to the convolution of $\rho(z)$ and PSF. Figure 3.6 summarizes the annealing time dependence of σ^2, showing that σ^2 increases with time

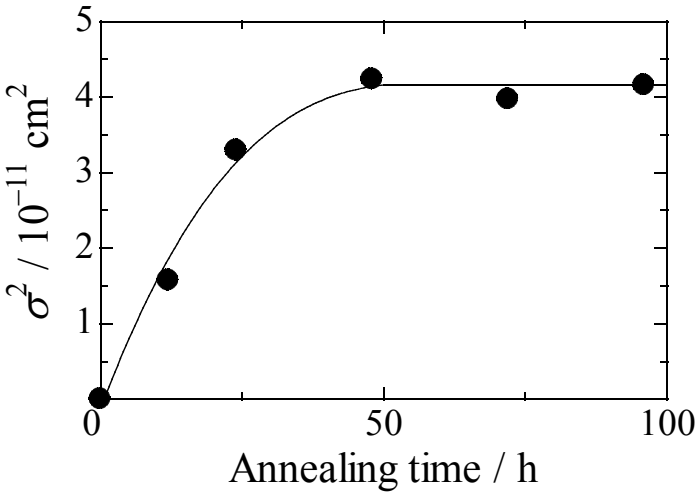

Figure 3.6. Annealing time dependence of the spatial distribution of the chain segment of PMMA-Pe.

and then saturated at 48 h. The polymer diffusion in bulk can be well described by reptation model proposed by Edwards[28] and de Gennes.[29] In this model, the polymer chain is constrained in a virtual tube composed by the entanglement network of the neighboring chains and the random motion occurs in the tube. For the longer time than the reptation time τ, the diffusion obeys the Fick's law. In this system, the annealing time is far shorter than the reptation time, which was estimated to be 6×10^3 h,[30] indicating that the observed motion is not characterized by the reptational diffusion. Furthermore, the diffusion coefficient of the large molecular weight PMMA used in this experiment is calculated as the order of 10^{-17}–10^{-18} cm^2 s^{-1} at 170 °C,[30-32] whereas the apparent diffusion coefficient until 48 h in Figure 3.6 was 1×10^{-16} cm^2 s^{-1}. The apparent diffusion coefficient is one or two orders larger than the translational diffusion coefficient of PMMA, indicating that we should consider very fast diffusion mechanism besides the reptational one. Zhang et al. examined chain dynamics at the period shorter than the reptation time using both the Rouse and the reptational relaxation models.[33] They reported that the time range at $t < \tau$ involves the relaxation of non-equilibrium

chain conformation and the segmental motion is dominant for the diffusion process. The polymer chain before annealing is in a non-equilibrium state because the chain is constrained on the surface and takes a two-dimensional conformation. Hence, the increase in σ^2 before 48 h in Figure 3.6 shows the conformational relaxation from the two-dimensional conformation to a more entropically favorable three-dimensional conformation by the thermal activation.

Figures 3.7a and 7b illustrate a conformation of the polymer chain confined in a monolayer and a conformation during rearrangement from two-dimensional form to three-dimensional one, respectively. Figures 3.7c and 7d show the segment density distribution of the single polymer chain in lateral directions before and after annealing, respectively. The polymer chain confined in two-dimensional monolayer is not allowed to cross over other chains due to the constraint in the height direction. Therefore, the polymer chain tends to exclude others in order not to make the free space in plane, and

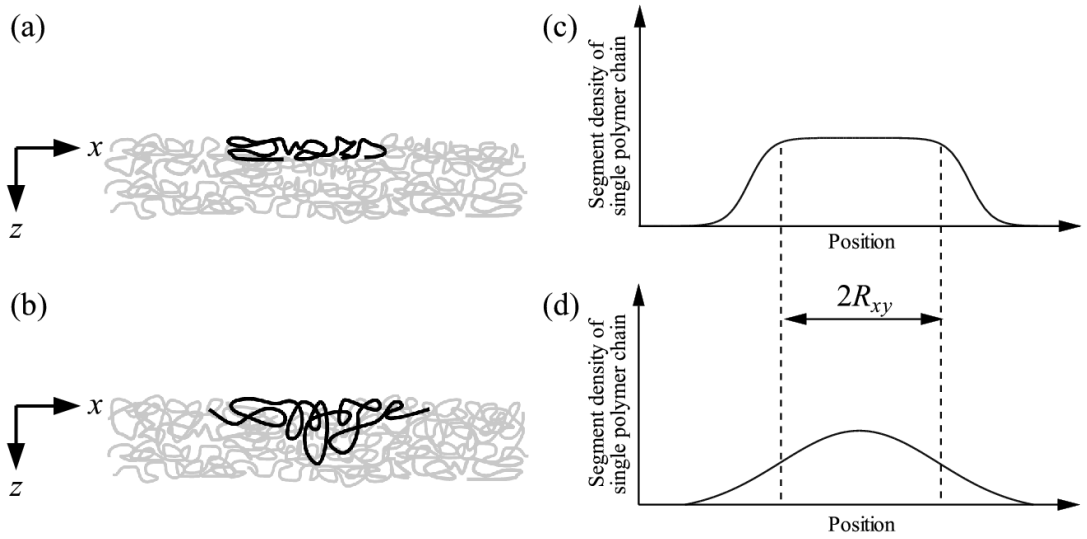

Figure 3.7. Schematic illustration of the thermally induced conformational relaxation from a two-dimensional form (a) to a three-dimensional one (b). The probe chains are shown in the solid curves. Schematic profiles of segment density of the single polymer chain are shown in right panels (c) and (d) for the before and after annealing, respectively.

consequently it takes a self-contracted conformation. Such a contracted conformation of two-dimensional polymer chain has been predicted by de Gennes' scaling theory[34] and confined by several experiments so far.[35,36] Although each chain is segregated from other ones in plane, it has to cover relatively large area of the surface determined by the limiting molecular area of the monomer unit and the degree of polymerization, because the volume of the chain and the density of the ultra-thin film must be constant even in the low dimensions. Considering these two-dimensional characteristics above mentioned, it is safely said that the polymer segments are homogeneously distributed inside the single polymer domain with a relatively large area. However, once the polymer chain becomes free from the restriction on the same kind bulk substrate, it starts interlacing with other chains and relaxes into a three-dimensional random coil. The mixing with surrounding polymer chains causes chain expansion mainly to the depth direction, that is the dimension newly released by deposition. Although our experimental time range is still short to attain the equilibrium state, the present results clearly show the characteristics of the two-dimensional polymer chains and conformational rearrangement process to an entropically favorable form in three-dimensions.

3.4 CONCLUSION

Real SNOM images of individual PMMA chains allowed one to discuss the characteristics of two-dimensional polymer chains and their conformational rearrangement after deposition on the solid substrate. The results are summarized as follows.

1) The conformation of polymer chain during rearrangement from a two-dimensional monolayer to three-dimensional random coils was directly observed by SNOM.

2) The averaged chain dimension in the lateral directions was not significantly altered by thermal treatment.

3) The chain segment was rearranged to a Gaussian distribution around the center of mass of the polymer chain after annealing.

4) The polymer chains penetrated into the bulk substrate at a rate faster than the translational diffusion of the entire polymer chains.

There are still intensive arguments on the particular characteristics of polymeric materials at the surface/interface and ultra-thin films thinner than the molecular dimensions, because it is crucially of important for design and fabrication of nanometric architectures. The current study revealed the relaxation mechanism of low dimensional chains in such a restricted space, and also the significance of direct imaging at the molecular level for investigating these advanced research fields.

References and Note

1. R. H. Tredgold, *Thin Solid Films*, **152**, 223 (1987).
2. S. Ito, M. Mabuchi, N.Sato, and H. Aoki, *Bull. Chem. Soc. Jpn.*, **78**, 371 (2005).
3. H. Ringsdorf, G. Schmidt, and J. Schneider, *Thin Solid Films*, **152**, 207 (1987).
4. M. B. Biddle, J. B. Lando, H. Ringsdorf, G. Schmidt, and J. Schneider, *Colloid Polym. Sci.*, **266**, 806 (1988).
5. Y.-K. See, J. Cha, T. Chang, and M. Ree, *Langmuir*, **16**, 2351 (2000).
6. J. Schneider, H. Ringsdorf, and J. F. Rabolt, *Macromolecules*, **22**, 205 (1989).
7. J. Schneider, C. Erdelen, H. Ringsdorf, and J. F. Rabolt, *Macromolecules*, **22**, 3475 (1989).
8. H. Hsiung, R. Beckerbauer, and J. M. Rodriguez-Parada, *Langmuir*, **9**, 1971 (1993).
9. M. Mabuchi, K. Kawano, S. Ito, and M. Yamamoto, *Macromolecules*, **31**, 6077 (1998).
10. M. Mabuchi, K. Kawano, S. Ito, M. Yamamoto, M. Takahashi, and T. Masuda, *Macromolecules*, **31**, 6083 (1998).
11. R. Kügler and W. Knoll, *Macromol. Chem. Phys.*, **203**, 923 (2002).
12. J. Kumaki, Y. Nishikawa, and T. Hashimoto, *J. Am. Chem. Soc.*, **118**, 3321 (1996).
13. J. Kumaki and T. Hashimoto, *J. Am. Chem. Soc.*, **125**, 4907 (2003).
14. Y. Roiter and S. Minko, *J. Am. Chem. Soc.*, **127**, 15688 (2005).
15. B. Maier and J. O. Rädler, *Phys. Rev. Lett.*, **82**, 1911 (1999).
16. B. Maier and J. O. Rädler, *Macromolecules*, **34**, 5723 (2001).
17. E. Abbe, *Arch. Mikrosk. Anat.*, **9**, 413 (1873).
18. E. Betzig and J. K. Trautman, *Science*, **257**, 189 (1992).
19. M. Ohtsu, ed., "*Near-Field Nano/Atom Optics and Technology*", Springer, Tokyo (1998).
20. M. A. Paesler and P. J. Moyer, "*Near-Field Optics: Theory, Instrumentation, and*

Applications", Wiley, New York (1996).

21. H. Aoki, M. Anryu, and S. Ito, *Polymer*, **46**, 5896 (2005).
22. T. Ube, H. Aoki, S. Ito, J. Horinaka, and T. Takigawa, *Polymer*, **48**, 6221 (2007).
23. H. Aoki and S. Ito, *J. Phys. Chem.*, **105**, 4558 (2001).
24. J. Rudnick and G. Gaspari, Science, 237, 384 (1987).
25. N. F. Zhang, M. T. Postek, R. D. Larrabee, A. E. Vladár, W. J. Keery, and S. N. Jones, *Scanning*, **21**, 246, (1999).
26. K. V. Mardia, *Biometrika*, **57**, 519 (1970).
27. G. Gabrielli, M. Puggelli, and P. Baglioni, *J. Colloid Interface Sci.*, **86**, 485 (1982).
28. S. F. Edwards, *Proc. Phys. Soc.*, **92**, 9 (1967).
29. P. G. de Gennes, *J. Chem. Phys.*, **55**, 572 (1971).
30. T. Masuda, K. Kitagawa, and S. Onogi, *Polym. J.*, **1**, 418 (1970).
31. In the reference 32, the translational diffusion coefficients of PMMA with various molecular weights at 145 °C are shown. Since many researcher showed that the diffusion constant of polymers decreased with the inverse second power of the molecular weight, the diffusion coefficient of PMMA at 145 °C was estimated to be on the order of 10^{-19}–10^{-20} cm^2 s^{-1}. Then, the translational diffusion coefficient at 170 °C was estimated to be on the order of 10^{-17}–10^{-18} cm^2 s^{-1} using time-temperature superposition principle with the shift factor of PMMA in the reference 30.
32. Y. Liu, G. Reiter, K. Kunz, and M. Stamm, *Macromolecules*, **26**, 2134 (1993).
33. H. Zhang and R. P. Wool, *Macromolecules*, **22**, 3018 (1989).
34. P. G. de Gennes, "*Scaling Concepts in Polymer Physics*", Cornell University Press, Ithaca, New York (1979).
35. N. Sato, S. Ito, and M. Yamamoto, *Polym. J.*, **28**, 784 (1996).
36. N. Sato, S. Ito, and M. Yamamoto, *Macromolecules*, **31**, 2673 (1998).

Chapter 4

Localization and Orientation of Homopolymer in Block Copolymer Lamella Studied by Scanning Near-Field Optical Microscopy

4.1. INTRODUCTION

Melts of block copolymers undergo disorder−order transition when the product of the Flory−Huggins interaction parameter (χ) and the degree of polymerization (N) exceeds 10.6.[1] Confined by the covalent bond between blocks, block copolymers can only phase-separate on the microscopic scale and self-assemble into various ordered structures such as spheres, cylinders, and lamellae.[2] The scale of block copolymer self-assembly is directly related to the sizes of the blocks. Therefore, the periodicity of self-assembled patterns formed by block copolymers is normally in the 10−100 nm range.

In recent years, there has been strong interest in studying homopolymer blends with block copolymers. When a homopolymer A dissolves in a matrix of a block copolymer A-*b*-B, where the two constituent polymers A and B are immiscible, the homopolymer will be confined to the A-rich domain formed by the block copolymer. This confinement results in entropy loss of the system. As an energetic compensation, individual homopolymers may have preferred locations, conformations, and orientations in the block domains.

Studies of homopolymer localization in block copolymer lamellae have been widely explored both theoretically[3,4] and experimentally by small-angle X-ray and neutron scattering,[5-8] transmission electron microscopy,[9] atomic force microscopy,[10] specular neutron reflectivity,[11,12] and fluorescence resonance energy transfer.[13] If the concentration of the homopolymer is low enough, the presence of the homopolymer will

not alter the lamellar structure of the block copolymer. The location of the homopolymer in the block copolymer lamella mainly depends on the molecular weights of the homopolymer A (M_A) and block A of the block copolymer (M_{bA}). Briefly, if $M_A < M_{bA}$, the homopolymer distributes throughout the A-rich domain. As M_A increases, A tends to concentrate in the center of the A-rich domain.[14] All of the related research has concentrated on characterizing the localization and spatial distribution of the homopolymer chains in the block domains. The conformation and orientation of the homopolymer chains confined to the block domains have not been studied due to the lack of suitable experimental techniques.

Characterization of polymer chain conformations requires a technique that has both high spatial resolution and the capability to distinguish the target polymer chain from the rest of the matrix. Fluorescence technique appears to be a very promising tool in the studies such as polymer conformation, morphology, and blend miscibility.[15,16] The merit of this technique is its high sensitivity associated with fluorescence detection. One needs only a trace amount of the fluorescent chromophore to acquire information about a system, and the system itself will not be distorted significantly by the presence of the chromophore. Among fluorescence techniques, fluorescence microscopy is very powerful in detecting a single dye-labeled polymer chain in a nonfluorescent matrix. But because of the diffraction limit,[17] the highest resolution of a conventional fluorescence microscope can only reach about half of its excitation wavelength. This significantly limits its application in characterizing the conformation of a single polymer chain.

Scanning near-field optical microscopy (SNOM) is a novel technique that breaks the optical diffraction barrier. As a member of the family of scanning probe microscopies, SNOM is equipped with a quasi-point light source that has a diameter much smaller than the wavelength of the excitation light. By scanning the sample

surface at a very close distance, SNOM can reach a resolution down to tens of nanometers.[18,19] The advantage of SNOM over other microscopy techniques arises not only from its ability to create high resolution, spectrally resolved optical images that allows one to study the objects within nanometer scale, but also from its nature of operating with light. As a complement to other techniques such as scanning tunneling microscopy, scanning electron microscopy, and atomic force microscopy, SNOM is extremely useful in nanoscience related to different optical properties, such as fluorescence, absorption, and polarization. In recent years, SNOM has been widely applied to many fields in polymer science such as studies on phase separation in polymer blend,[20] single-chain characterizations in polymer monolayers,[21] and investigations on the ordered structure of block copolymers.[22,23]

In this chapter, the author describes SNOM measurements on imaging single poly(methyl mathacrylate) (PMMA) homopolymer chains embedded in lamellar domains formed by polystyrene-*block*-poly(methyl methacrylate) (PS-*b*-PMMA). The localization, shape, and orientation of single PMMA chains in the PMMA-rich domain of the block copolymer lamella is discussed.

4.2. EXPERIMENTAL SECTION

4.2.1. Sample Preparation

Perylene-labeled poly(methyl methacrylate) (PMMA-Pe) was synthesized by radical copolymerization of methyl methacrylate and 3-perylenyl methyl methacrylate.[24] The details on the synthesis are written in chapter 2. The weight average molecular weight, M_w, and the molecular weight distribution, M_w/M_n, were 3.0×10^6 and 1.3, respectively. The molar fraction of the perylene moiety introduced in a PMMA chain was evaluated to be 0.84 % from UV-Vis absorption measurement. Symmetric PS-*b*-

PMMA (molecular weight: 8.68×10^5 (PS)−8.57×10^5 (PMMA); PDI: 1.3) was purchased from Polymer Source and used without further purification. Four sets of PMMA-Pe/PS-*b*-PMMA mixtures (molar ratios of PMMA-Pe/PS-*b*-PMMA: 1.6×10^{-5}, 3.7×10^{-5}, 6.4×10^{-5}, and 9.0×10^{-5}) were prepared, and each of them was dissolved in chloroform (reagent grade, Wako) to form a 2 wt% solution. The polymer solutions were spread on clean glass plates. After drying, all of the films were annealed sequentially in chloroform vapor at room temperature (72 h)[25,26] and in vacuum at 170 °C (24 h). In this way, the author obtained a thick film (30 μm), with long-range ordered lamellar structure. PMMA-Pe/PMMA thick film was prepared in a similar way, but without the solvent treatment. PMMA standard (American Polymer Standards, M_n = 1.7×10^6) was used as the matrix. The author controlled the concentration of PMMA-Pe in PMMA at 0. 0025 wt %. The polymer solution (1 wt% in toluene) was spread on glass plate and slowly dried at room temperature for 72 h. The dried thick film was then annealed in vacuum at 130 °C for 24 h and at 170 °C for 48 h. All prepared thick films were removed from the glass substrates and sliced into ultra-thin films (50 nm) by microtoming (Ultracut UTC, Leica microsystems). The sliced ultra-thin films were then mounted on glass plates for the SNOM measurements.

4.2.2 SNOM Measurements

SNOM imaging was performed using a commercial α-SNOM (WITec) with a 441-nm laser (BCL-015-440, CrystaLaser) as the excitation source. A cantilever probe was used to scan the sample surface in contacting mode. The probe has a nanoaperture (60 nm) at the tip end, and the light passing through the aperture excites the perylene chromophores inside the polymer film. The signal light from the specimen was collected by a microscope objective (60×, 0.8 NA, Nikon) and split by a beam sampler. 4 % of the collected signal was directed to an analog PMT (H5784, Hamamatsu

Photonics) to obtain the transmission image, and the rest was detected by a photon counting PMT (H8631, Hamamatsu Photonics) after passing through a long-pass filter (LP02-442RS-25, Semrock) to acquire the fluorescence image. All images were recorded at a pixel size of 3.9 nm × 3.9 nm and a pixel dwell time of 3.9 ms. The surface topography (TP), fluorescence (FL), and transmission (TRANS) images were simultaneously obtained from the scanning area.

4.3. RESULTS AND DISCUSSION

4.3.1. SNOM Imaging of a Single PMMA Chain

The FL images show that all fluorescent spots are homogeneously distributed throughout the sliced thin films. For each FL image (dimensions: 15 × 15 μm), the number density of the fluorescent spots by counting the number of fluorescent spots in the image was calculated. Figure 4.1 shows the observed number density of fluorescent spots at different PMMA-Pe/PS-*b*-PMMA ratios. The number density of fluorescent spots is in good agreement with the number density of PMMA-Pe chains in PS-*b*-PMMA matrix, based on the polymer molar ratio. This indicates that one fluorescent spot in the SNOM FL images corresponds to a single PMMA-Pe chain embedded in the block copolymer matrix.

Figure 4.2 shows a set of SNOM images obtained simultaneously from an area (1 × 1 μm) in a sliced PS-*b*-PMMA ultra-thin film doped with PMMA-Pe. The TP image (a) shows no surface feature and can hardly provide any useful information about the morphology or polymer chain conformation. The TRANS image (b) clearly shows the alternative local contrast between the two block domains of the PS-*b*-PMMA. This contrast may originate from the different refractive indices of PS (1.59) and PMMA (1.49).[27] The bright areas correspond to the PMMA domains and the dark parts are the

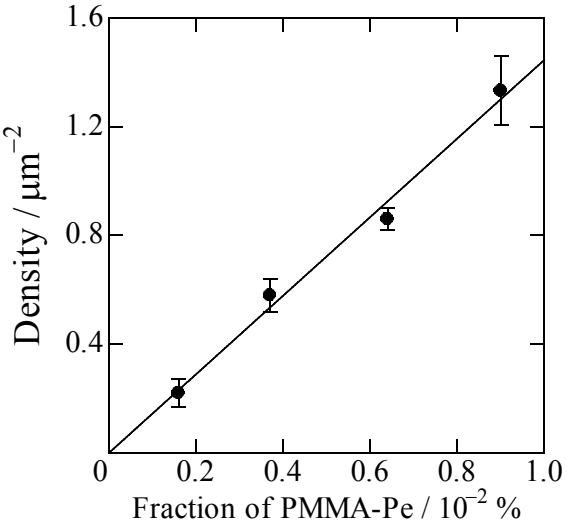

Figure 4.1. Number densities of fluorescent spots (solid squares with error bars) obtained from SNOM FL images at different PMMA-Pe/PS-*b*-PMMA ratios. The density value with the error bar at each ratio is the averaged value with standard deviation. The solid line is the calculated number density of PMMA-Pe chains in the PS-*b*-PMMA matrix, based on the molar ratio of PMMA-Pe to PS-*b*-PMMA.

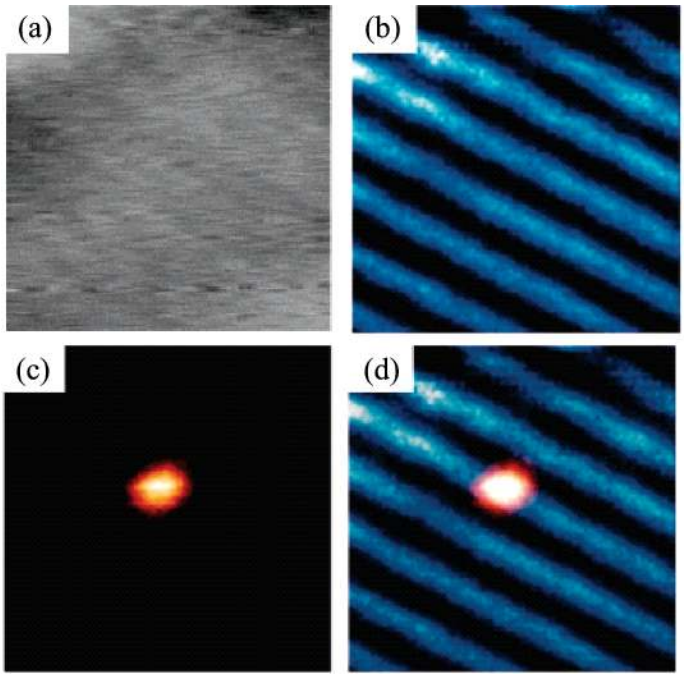

Figure 4.2. Topography (a), transmission (b), fluorescence (c), and superimposed (d) (b and c) images of a scanning area in a PMMA-Pe/PS-*b*-PMMA thin film. The dimension of all images is 1 μm × 1 μm. The blue and dark parts in the image correspond to PMMA and PS, respectively. The bright spot in (c) corresponds to a single PMMA-Pe chain embedded in the PS-*b*-PMMA matrix.

areas occupied by the PS blocks.[28] The bright spot in the FL image (c) corresponds to the single PMMA-Pe chain embedded in the block copolymer lamella. (d) is a pseudo-colored superimposed image of (b) and (c), which indicates the location and orientation of the homopolymer chain in the PMMA-rich domain layer of the PS-*b*-PMMA lamella.

4.3.2 Analyses of SNOM Images.

4.3.2.1. Conformation, Orientation, and Center of Mass of a Single PMMA Chain.

In order to analyze the chain conformations of the PMMA-Pe chains shown in the acquired FL images.[29,30] As shown in Figure 4.3, the author selects an area including the bright spot in the FL image and read the fluorescence intensity at every pixel throughout this area. The normalized second moment tensor of the fluorescence intensity distribution, **M**, is expressed as

$$\mathbf{M}=\begin{pmatrix} M_{xx} & M_{xy} \\ M_{yx} & M_{yy} \end{pmatrix}, \tag{4.1}$$

$$M_{xx}=\frac{1}{I_0}\sum_{i,j} I_{ij}\left(x_{ij}-x_0\right)^2, \qquad M_{yy}=\frac{1}{I_0}\sum_{i,j} I_{ij}\left(y_{ij}-y_0\right)^2,$$

$$M_{xy}=M_{yx}=\frac{1}{I_0}\sum_{i,j} I_{ij}\left(x_{ij}-x_0\right)\left(y_{ij}-y_0\right),$$

where I_0 is the sum of the intensity of the selected area and (x_{ij}, y_{ij}) is the Cartesian coordinate of the pixel (i, j) in the image. The coordinate of the intensity-weighted center of mass (CM) of the PMMA-Pe chain is

$$x_0=\frac{1}{I_0}\sum_{i,j} I_{ij}x_{ij}, \qquad y_0=\frac{1}{I_0}\sum_{i,j} I_{ij}y_{ij}, \tag{4.2}$$

The tensor **M** is a measure of the size and shape of the PMMA-Pe polymer chain. In this way, the investigated polymer chain spot can be represented as an ellipse with long

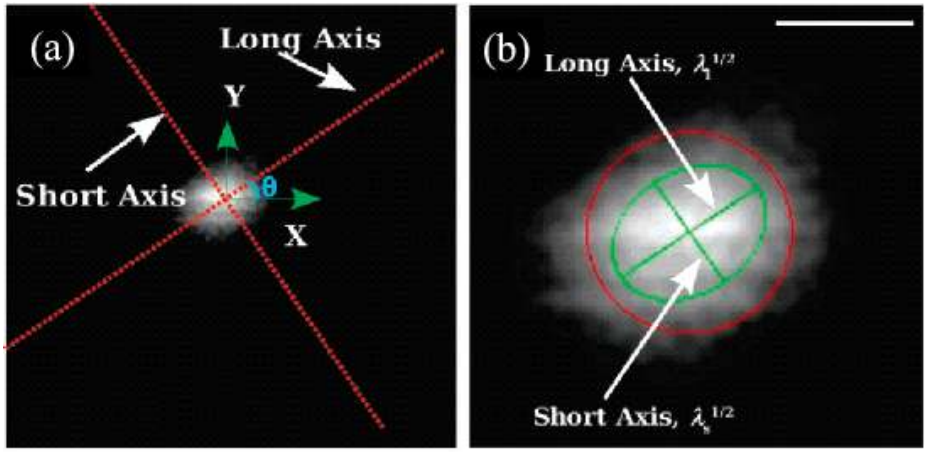

Figure 4.3. Determination of the orientation and the center of mass of a PMMA-Pe chain. (a) Duplicated FL image of Figure 4.2c (dimension: 1 × 1 μm). The bright white spot corresponds to a single PMMA-Pe chain. The chain orientation, indicated as the long axis, is calculated on the basis of the method described in the text. The short axis is perpendicular to the chain orientation. The center of mass of the PMMA-Pe chain is located at the intersection of the two axes. The orientational angle (θ) of the polymer chain is indicated in the figure. (b) Enlarged image of the PMMA-Pe chain shown in (a). The radius of the red circle is the calculated R_{xy} of the PMMA-Pe chain. The green ellipse is drawn with the square roots of the two eigenvalues (λ_l and λ_s) as the long and short axes. The long axis defines the orientation of the PMMA-Pe chain. The scale bar in (b) is 100 nm.

and short principal axes. The eigenvalues of the long (λ_l) and the short (λ_s) principal axes are given by

$$\lambda_{l,s} = \frac{\mathrm{tr}(\mathbf{M}) \pm \sqrt{\mathrm{tr}(\mathbf{M})^2 - 4\det(\mathbf{M})}}{2}, \tag{4.3}$$

where tr(**M**) and det(**M**) are the trace and the determinant of **M**. The trace of **M** corresponds to the squared radius of gyration for the projection of the PMMA-Pe chain in the *x*-*y* plane;

$$R_{xy}^2 = \mathrm{tr}(\mathbf{M}) . \tag{4.4}$$

The orientation of the PMMA-Pe chain is defined as the orientational angle (θ) of the long principal axis relative to the positive x-axis

$$\theta = \arctan\left(\frac{\lambda_1 - M_{xx}}{M_{xy}}\right). \tag{4.5}$$

4.3.2.2. Determination of Lamellar Spacing and Lamellar Orientation.

The periodical spacing and the orientation of the PS-*b*-PMMA lamella were determined from the fast Fourier transform (FFT) of the TRANS images, as shown in Figure 4.4.[31] Figure 4.4a is the duplicated TRANS image of Figure 4.2b, which shows the lamellar structure formed by the PS-*b*-PMMA block copolymer. FFT (inset of Figure 4.4a) of the TRANS image shows an ordered pattern of the lamellar structure in the reciprocal space. The author drew a line that passes through the pattern and counted the intensity along the line. The direction of the line indicates the orientation of the

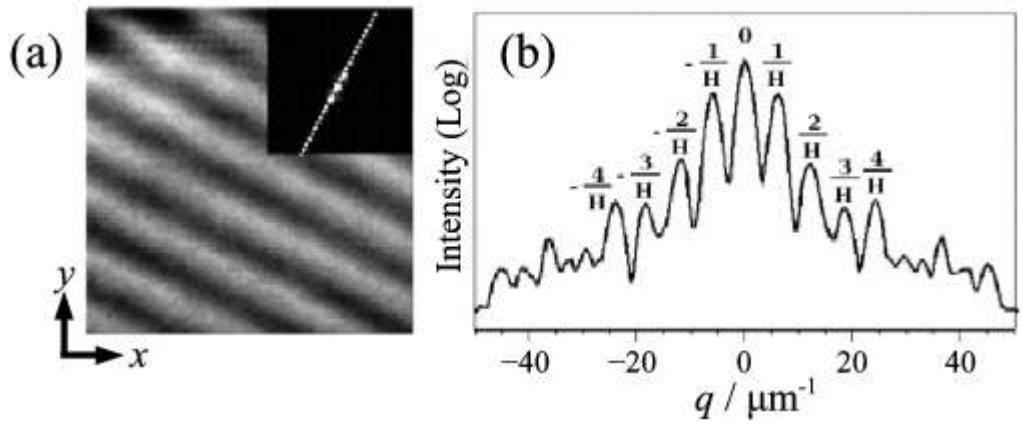

Figure 4.4. Determination of the orientation and the spacing of a sample lamellar structure formed by PS-*b*-PMMA. (a) TRANS image and its fast Fourier transform (FFT) image (inset). The white dotted line passes through the pattern in the FFT image and shows the orientation of the lamellar structure (lamellar normal). (b) Intensity distribution along the dotted line shown in the inset of (a). The ordered peaks are indicated in the figure. H is the lamellar spacing.

lamellar structure (lamellar normal). The author defined the angle between the orientation of the PMMA-Pe chain and the lamellar normal as the relative orientational angle of the PMMA-Pe chain embedded in the PS-*b*-PMMA lamella.[32] The lamellar spacing of PS-*b*-PMMA is 156 ± 6 nm, calculated from the distance between the characteristic peaks in the intensity distribution profile, as shown in Figure 4.4b.

4.3.2.3. Determination of the CM Location of a PMMA-Pe Chain in the Lamella.

The author located the CM of the PMMA-Pe chain, calculated from Figure 4.3 and equation 4.2, in the TRANS image. In Figure 4.5a, the CM of PMMA-Pe is indicated as a white circle in the TRANS image. The black solid line passes through the CM and has the same orientation as the block copolymer lamellar normal. The author tracked the transmission intensity in the TRANS image across the PMMA-rich domain along this solid line. The transmission intensity distribution, shown as the open circles in Figure 4.5b, was then fitted to a modified Helfand−Tagami hyperbolic function[33,34]

$$I(x)=a+b\left[\tanh\frac{2\{(x-c)+d\}}{\delta}-\tanh\frac{2\{(x-c)-d\}}{\delta}\right]. \qquad (4.6)$$

In equation 4.6, $I(x)$ is the fitted transmission intensity distribution across the PMMA-rich domain, along the solid line shown in Figure 4.5a. x is the coordinate along the solid line. a, b, c, d, and δ are the floating parameters used in the fitting. Among those parameters, c refers to the distance between the CM and the center of the PMMA-rich domain layer in the direction of the lamellar normal. δ is the width of the interface between the PS and PMMA domains. The author defined the full width at half-maximum (FWHM) of the fitted profile as the width of the PMMA-rich domain.

Using the above methodology of the SNOM image analysis, 100 PMMA-Pe chains located at different areas in the PS-*b*-PMMA lamellae were analyzed. The author calculated the orientational angle of each PMMA-Pe chain relative to the lamellar

normal and the relative position of the PMMA-Pe chain located in the PMMA-rich domain of the copolymer matrix. All information was compiled to construct the relationship between the chain orientation and the location of PMMA-Pe in the PS-*b*-PMMA lamella.

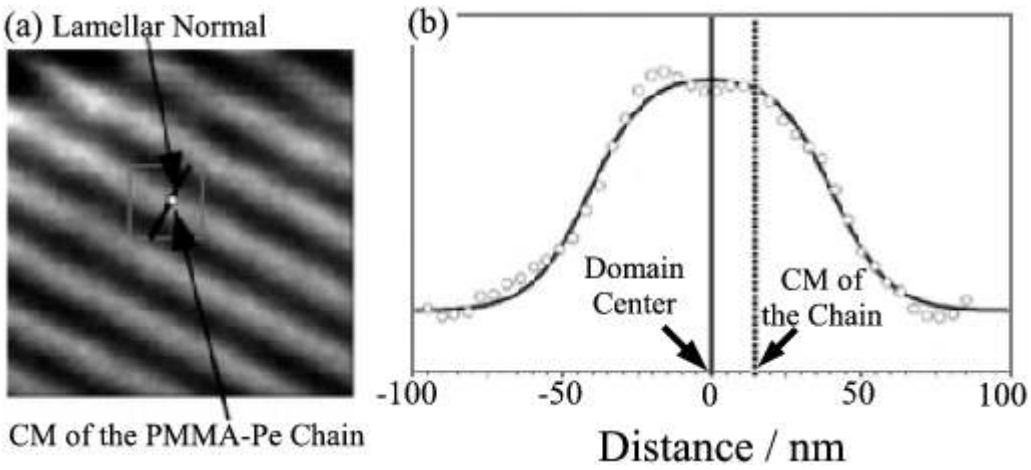

Figure 4.5. Location of the center of mass (CM) of a PMMA-Pe homopolymer chain in the PS-*b*-PMMA lamella (a) and cross-section profile in the normal direction to the lamella (b). (a) TRANS image duplicated from Figure 4.2b. The CM of the Pe-PMMA is shown as the white spot. The solid line is the line path used to calculate the cross-section profile of the transmission intensity. It passes through the CM of the PMMA-Pe and has the same orientation as the PS-*b*-PMMA lamellar normal. (b) Cross-section distribution (open circles) of the transmission intensity recovered from (a) along the solid line. The solid curve in (b) is the fitted intensity profile (equation 4.6). The author set the origin of the distance coordinate to the center of the PMMA-rich layer. The coordinate of the dashed line represents the distance between the CM of the PMMA-Pe and the center of the PMMA-rich domain.

4.3.3. Localization of PMMA Homopolymer Chains in the Lamella.

Russell and co-workers investigated the localization of PMMA homopolymers in PS-*b*-PMMA block copolymer lamellae, using specular neutron reflectivity.[11,12] According to their results, the localization of PMMA homopolymer in the PS-*b*-PMMA lamella depends on the molecular weights of the PMMA ($M_{\text{h-PMMA}}$) and the PMMA block of the PS-*b*-PMMA ($M_{\text{b-PMMA}}$): If $M_{\text{h-PMMA}}$ is small compared to $M_{\text{b-PMMA}}$, the PMMA homopolymer tends to distribute throughout the PMMA domain homogeneously; if $M_{\text{h-PMMA}}$ is comparable to $M_{\text{b-PMMA}}$, the homopolymer tends to distribute in the domain with the highest concentration at the center; if $M_{\text{h-PMMA}}$ is much larger than $M_{\text{b-PMMA}}$, the PMMA chains segregate from the block domain and form relatively small domains distributed throughout the film. In the present measurement, the author is interested in characterizing a single polymer chain in a copolymer matrix. The extremely low PMMA homopolymer concentration in the matrix is unfavorable for the aggregation of PMMA homopolymer. As a consequence, individual homopolymer chains will be isolated in the copolymer matrix. The location and conformation of the single polymer chain depend on the local enthalpic interactions between the homopolymer chain and the surrounding block copolymer chains.

Figure 4.6 shows a histogram of the localization of the 100 PMMA-Pe chains in PS-*b*-PMMA. In this figure, the population of PMMA-Pe chains is plotted against the distance between the CM of the PMMA-Pe chain and the center of the PMMA-rich domain layer. The average size of half of a PMMA domain was found to be 41 ± 5 nm. It is easily seen that the PMMA homopolymer chains are neither homogeneously distributed in the PMMA-rich domain nor all confined to the center of the block domain layer. The FL images show that segments of the PMMA-Pe chains distribute throughout the PMMA-rich domain. It was found that more than 90% of the CMs of PMMA homopolymer chains were located in the PMMA-rich domain, and the center of

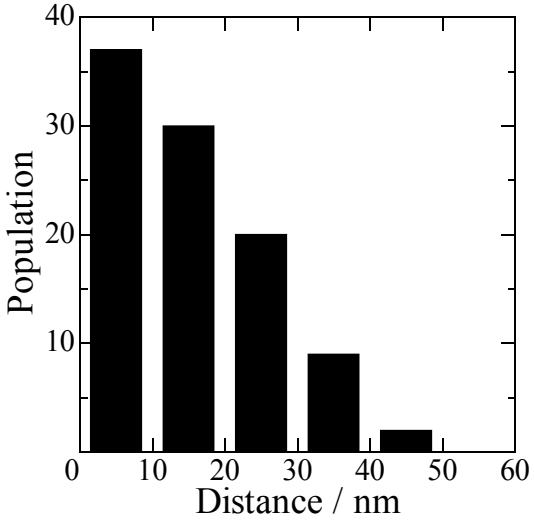

Figure 4.6. Histogram of the localization of PMMA homopolymer in the PMMA-rich domain of the PS-*b*-PMMA block copolymer lamella. The population of PMMA homopolymer chains is plotted against the distance between the CM of a PMMA homopolymer chain and the center of the PMMA-rich domain (parameter *c* in equation 4.6). The average size of half of the PMMA-rich domain is 41 ± 5 nm (half of the FWHM in equation 4.6).

the PMMA-rich domain had the highest CM population. A few PMMA homopolymer chains protrude from the PMMA-rich domain and entangle with the PS block chains. The embedded PMMA-Pe homopolymers have an average R_{xy} of 88 ± 13 nm. This value is smaller than the R_{xy} of the PMMA-Pe in the PMMA matrix (117 ± 13 nm).[35] The synthesized PMMA-Pe has a molecular weight (M_n = 2 300 000) 3 times larger than that of the PMMA block (M_n = 857 000) of the PS-*b*-PMMA sample. The difference of the two R_{xy}'s clearly shows the confinement effect of the block copolymer lamella on the conformation of the embedded PMMA-Pe homopolymer.[36] Segments of the individual homopolymer chains crowd into the PMMA-rich domain layers due to the repulsive interaction between PMMA homopolymer and PS. The FL images also show that the compression of the PMMA-Pe chain is not homogeneous, resulting in a certain

orientation along the calculated long principal axis. The average square roots of the two eigenvalues of the PMMA-Pe chains were found to be 67 ± 10 and 56 ± 8 nm in the direction parallel with and perpendicular to the chain orientation, respectively. The difference is small and independent of the CM location of the PMMA homopolymer chains, indicating that the restricted PMMA-rich domain in a PS-*b*-PMMA lamella only has a moderate effect on the anisotropic deformation of the embedded PMMA homopolymer chains.

4.3.4. Relative Orientation of PMMA Homopolymer Chains in the Lamella.

Although the deformation of the homopolymer chains inside the block domain is less than the expectation, the orientation of an embedded PMMA-Pe chain can still be accurately determined using the method described in the section of image analysis. The author constructed a relationship between the orientation and location of homopolymer chains embedded in the PMMA-rich domains of the block copolymer lamella. As shown in Figure 4.7a, for each PMMA-Pe chain, the angle between the chain orientation and the lamellar normal was plotted against the relative CM position of the homopolymer chain in the block domain. It was found a weak tendency that the homopolymer chains oriented themselves depending on their locations in the PMMA-rich domain layer. When the CM of PMMA homopolymer is at the center of the PMMA-rich domain layer, the homopolymer prefers an orientation parallel to the lamella phase; i.e., the orientation has an angle of 90° from the lamellar normal. When the PMMA homopolymer chain is situated close to the interface, its orientation tends to be perpendicular to the lamella phase.

Figure 4.7b shows the shape parameter, defined as the square root of the ratio between the two eigenvalues of the long (λ_l) and the short (λ_s) principal axes, of a PMMA-Pe homopolymer chain relative to its location in the block copolymer lamellae.

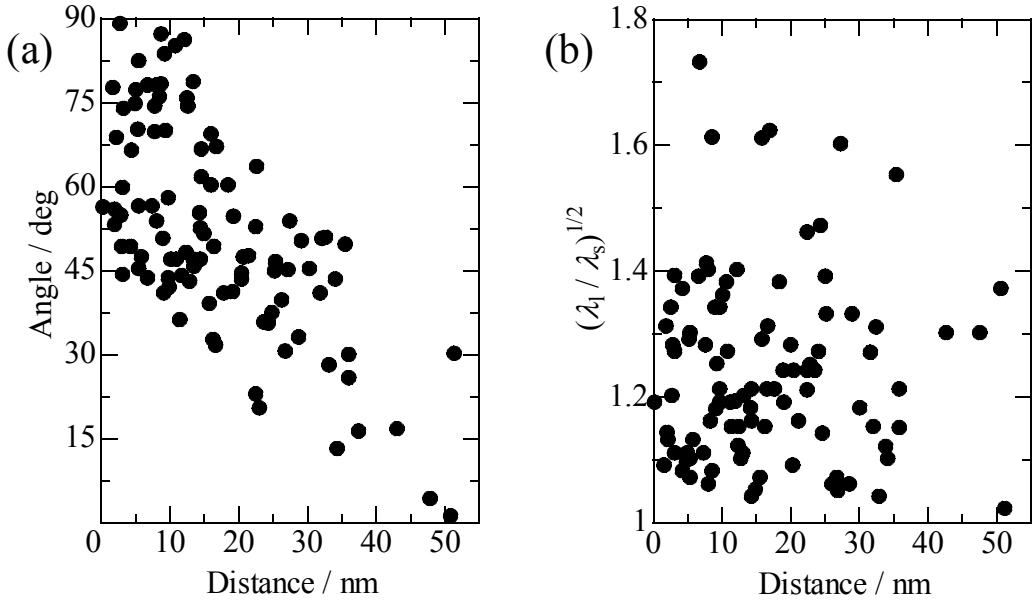

Figure 4.7. (a) Plot of chain orientation of PMMA-Pe against the CM location in the PMMA-rich domains of PS-*b*-PMMA lamellae. The *y*-axis shows the relative angle between the chain orientation and the lamellar normal. The *x*-axis shows the distance between the CM of PMMA-Pe and the center of the corresponding PMMA-rich domain layer. (b) Plot of the shape parameter (defined as the square root of the ratio between the two eigenvalues of the long (λ_l) and the short (λ_s) principal axes) of a PMMA-Pe homopolymer chain against its CM location in the PS-*b*-PMMA block copolymer lamellae. The *x*-axis has the same meaning as that in (a).

Although it was found that the PMMA homopolymer chain had weak preferred orientation depending on its location in the block copolymer lamella, the shape of a homopolymer chain seems to have no relationship with its CM location. Moreover, the blurring effect, caused by the finite dimension of the aperture on the SNOM probe, always exists in the fluorescence imaging. This blurring effect makes the fluorescent object more roundlike than its real shape. As a consequence, it is difficult to compare the shape determined from the FL image to the real shape of the PMMA-Pe homopolymer chain. Here the author only showed the determined shape parameters of the PMMA-Pe chains, and was reluctant to draw further conclusions about the shape of the homopolymer chains.

Figure 4.8 illustrates the position dependence of the PMMA homopolymer chain orientation in the PS-*b*-PMMA block copolymer lamella. It is well-known that the system free energy of a neat, phase-separated block copolymer system can be split into an interfacial and a stretching contribution.[1] The interfacial free energy includes the contact enthalpy between the blocks and the confinement entropy originating from the selective location of the block chains in the ordered structure. The stretching energy is caused by the extension of the block chain, which tends to compensate for the unfavorable contact with the different block type. The chain stretching effect causes preferred orientation of the block chains perpendicularly to the lamellar phase.[5] When an ordered structure is formed, all energetic contributions balance each other to minimize the overall free energy of the system. If the PMMA homopolymer chains sparsely locate in a matrix of PS-*b*-PMMA lamellae, the individual chains are confined to the PMMA-rich domain due to the repulsive interaction between the PS block and the PMMA homopolymer chain. This confinement results in entropy loss of the system, and as an energetic compensation, the PMMA homopolymer chain will have preferred location and orientation in the PMMA-rich domain. Since the investigated PMMA-Pe

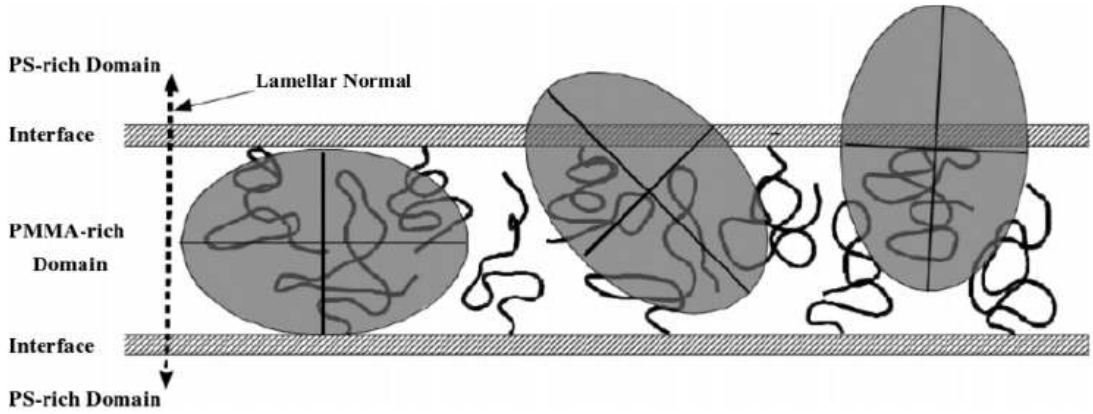

Figure 4.8. Sketch showing the relationship between the orientation and location of PMMA homopolymer chains inside a PMMA-rich domain layer. The black coils represent the PMMA block chains. The elliptical shadows stand for the PMMA homopolymer chains with specific conformation and orientation inside the block domain. The longer black line in each shadow indicates the orientation of the specific PMMA homopolymer chain. The CM of the PMMA homopolymer chain is located at the intersection of the two black lines in each shadow.

has a molecular weight 3 times larger than that of the PMMA block, to minimize the system energy, the PMMA homopolymer chains tend to locate at the center of the PMMA-rich domain. Meanwhile, the PMMA homopolymer chains are compressed and, most likely, anisotropically deformed in the direction parallel with the lamella phase due to the large molecular weight of the homopolymer. In a neat block copolymer lamella, the simulation results showed that the segments close to the end of the block chain had more rotational freedom than those close to the block junction.[37] If the homopolymer chain is at the center of the domain layer, it is in an environment that allows the homopolymer chain to rotate more freely upon annealing. The homopolymer chain can easily rotate and rearrange itself to minimize the local free energy in its neighborhood. The homopolymer chain will, therefore, have preferred orientation parallel to the lamella phase.

Although most of the PMMA homopolymer chains locate at the center of the PMMA-rich domain, present results show that, for some homopolymer chains, part of the chain segments are in areas close to the block interface, or even in the PS domain, due to fluctuations. When most of the segments of the homopolymer chain are localized close to the block interface, the rotational movement of the homopolymer chain is much retarded by block chains (lack of rotational freedom). Segments can rearrange alongside the block chains only during annealing. The block chains have preferred orientations perpendicular to the lamellar phase due to the chain stretching effect, and the homopolymer chains close to interfacial area will also have preferred orientations perpendicular to the lamella.

4.4. CONCLUSION

In this chapter, the localization and orientation of single PMMA homopolymer chains confined in a PS-*b*-PMMA block copolymer lamella are studied. The results show that most of the dispersed PMMA homopolymer chains are localized in the PMMA-rich layers. Although the PMMA homopolymer chains are deformed due to the confinement of the block domains of the block copolymer, the extent of the deformation is neither significant nor dependent on the chain location. The orientational preference of the homopolymer chain in the block domain is reported for the first time. The orientation of the homopolymer chain has a weak dependence on the location of the homopolymer inside the block domain. When the homopolymer is situated at the center of the PMMA domain, it has an orientation parallel to the lamellar phase. With the increase of the distance between the CM of homopolymer chain and the domain center, the homopolymer chain tends to orient itself perpendicularly to the interface. This is a result of the rotational freedom of the homopolymer in the block domain.

References and Notes

1. F. S. Bates and G. H. Fredrickson, *Annu. Rev. Phys. Chem.* **41**, 525 (1990).
2. I. W. Hamley, "*The Physics of Block Copolymers*", Oxford University Press, New York (1998).
3. K. R. Shull and K. I. Winey, *Macromolecules*, **25**, 2637 (1992).
4. J. D. Vavasour and M. D. Whitemore, *Macromolecules*, **34**, 3471 (2001).
5. Y. Matsushita, K. Mori, R. Saguchi, Y. Nakao, I. Noda, and M. Nagasawa, *Macromolecules*, **23**, 4313 (1990).
6. H. Hasegawa, T. Hashimoto, H. Kawai, T. P. Lodge, E. J. Amis, C. J. Glinka, and C. C. Han, *Macromolecules*, **18**, 67 (1985).
7. Y. Matsushita, K. Mori, Y. Mogi, R. Saguchi, I. Noda, M. Nagasawa, T. Chang, C. J. Glinka, and C. C. Han, *Macromolecules*, **23**, 4317 (1990).
8. S. Koizumi, H. Hasegawa, and T. Hashimoto, *Macromolecules*, **27**, 7893 (1994).
9. K. I. Winey, E. L. Thomas, and L. J. Fetters, *Macromolecules*, **25**, 2645 (1992).
10. K. A. Orso and P. F. Green, *Macromolecules*, **32**, 1087 (1999).
11. A. M. Mayes, T. P. Russell, S. K. Satija, and C. F. Majkrzak, *Macromolecules*, **25**, 6523 (1992).
12. K. R. Shull, A. M. Mayes, and T. P. Russell, *Macromolecules*, **26**, 3929 (1993).
13. Y. Rharbi, J. Zhang, J. G. Spiro, L. Chen, M. A. Winnik, J. D. Vavasour, M. D. Whitmore, and R. Jérôme, *Macromolecules*, **36**, 1241 (2003).
14. S. Koizumi, H. Hasegawa, and T. Hashimoto, *Macromolecules*, **27**, 6532 (1994).
15. M. A. Winnik, ed., "*Photophysical and Photochemical Tools in Polymer Science*", Reidel, Dordrecht (1985).
16. T. Tanaka, ed., "*Experimental Methods in Polymer Science*" Academic, San Diego (2000).
17. E. Abbe, *Arch. Mikrosk. Anat.*, **9**, 413 (1873).

18. E. Betzig and J. K. Trautman, *Science*, **257**, 189 (1992).
19. R. Dunn, *Chem. Rev.*, **99**, 2891 (1999).
20. H. Aoki, Y. Kunai, S. Ito, H. Yamada, and K. Matsushige, *Appl. Surf. Sci.*, **188**, 534 (2002).
21. H. Aoki, M. Anryu, and S. Ito, *Polymer*, **46**, 5896 (2005).
22. M. J. Fasolka, L. S. Goldner, J. Hwang, A. M. Urbas, P. DeRege, T. Swager, and E. L. Thomas, *Phys. Rev. Lett.*, **90**, 016107 (2003).
23. M. B. Raschke, L. Molina, T. Elsaesser, D. H. Kim, W. Knoll, and K. Hinrichs, *ChemPhysChem*, **6**, 2197 (2005).
24. H. Aoki and S. Ito, *J. Phys. Chem. B*, **105**, 4558 (2001).
25. S. H. Kim, M. J. Misner, T. Xu, M. Kimura, and T. P. Russell, *Adv. Mater.*, **16**, 226 (2004).
26. Y. Xuan, J. Peng, L. Cui, H. Wang, B. Li, and Y. Han, *Macromolecules*, **37**, 7301 (2004).
27. J. Brandrup and E. H. Immergut, eds., "*Polymer Handbook, 3rd ed.*", John Wiley & Sons, New York (1989).
28. A dye-tagged symmetrical PS-*b*-PMMA block copolymer, of which the PMMA block was labeled by rhodamine chromophore, was synthesized and the sliced rhodamine-tagged PS-*b*-PMMA films with ordered lamellar structure were prepared. A 532-nm laser was used as the light source to detect the fluorescence of the rhodamine dyes inside the film. From the FL and TRANS images simultaneously obtained from a scanning area, the areas with higher intensity (brighter areas) in the TRANS image was identified as the domain occupied the PMMA block.
29. B. Maier and J. O. Rädler, *Phys. Rev. Lett.*, **82**, 1911 (1999).
30. B. Maier and J. O. Rädler, *Macromolecules*, **34**, 5723 (2001).

31. The FFT on the TRANS images was performed via Gwyddion, a free SPM data analysis framework developed under the terms of the GNU General Public License.
32. The angle between chain orientation and the orientation of the lamellar structure is in the 0−90° range. For a calculated value (α) larger than 90°, the author uses 180° − α as the angle.
33. E. Helfand and Y. Tagami, *J. Chem. Phys.*, **56**, 3592 (1972).
34. E. Helfand and Z. R. Wasserman, *Macromolecules*, **9**, 879 (1976).
35. The author followed the same method to calculate the FWHM of PMMA-Pe in the PMMA matrix. FL images show that the PMMA-Pe has no preferred orientation in the PMMA matrix. The author analyzed 40 fluorescent spots, each of which corresponds to single PMMA-Pe chains, and averaged all R_{xy} values.
36. The values of R_{xy} obtained from the analysis of the FL image contain the blurring effect of fluorescence due to the finite dimension of the aperture on the SNOM probe. As a consequence, the determined values of R_{xy} are larger than those measured by the small-angle neutron scattering (SANS).
37. J. Yang, M. A. Winnik, and T. Pakula, *Macromol. Theory Simul.*, **14**, 9 (2005).

Part II

Chapter 5

Conformation of Single Block Copolymer Chain in a Two-Dimensional Microphase-Separated Structure Studied by Scanning Near-Field Optical Microscopy

5.1. INTRODUCTION

Block copolymers consisting of the immisible polymers are well known to self-assemble into a variety of ordered structures such as sphere, cylinder, and lamella.[1,2] Since the domain size of the microphase-separated structure is directly related to the length of the blocks, the periodicity of the microphase-separated patterns is in the order of 10–100 nm. The theoretical and experimental investigations of the microphase separation of block copolymers have extensively explored.[3-9] Although the majority of the works has concentrated upon bulk systems, the recent interests are directed to thin films. The phase separation in the thin films differs appreciably from that in the bulk system due to the polymer segment/interface interactions and the conformational entropy of the polymer chain derived from the spatial confinement. Thus, the microphase separation in thin film has been a subject of the intensive interest in the phenomenological aspects of self-assembly in a confined state.[10-12] An ultimate form of the polymer thin film is a two-dimensional monolayer, which can be prepared by Langmuir-Blodgett technique. When a polymer consisting of amphiphilic monomers is spread on water, the main chain is adsorbed on the water surface, resulting in the monolayer with thickness of the size of the monomer unit. The polymer monolayer can be regarded as a model of the two-dimensional system of polymers. In the previous studies,[13-15] the two-dimensional microphase-separated structures deposited on a

substrate was visualized by atomic force microscopy (AFM). The domain size was significantly larger than that in three-dimensional systems, suggesting that the chain conformation is different from that in a three-dimensional bulk state. Since the conformation of the block chain forming the microphase-separated structure is one of the most fundamental issues to understand the morphology, it has been extensively investigated by small angle neutron scattering (SANS).[16-20] For example, Hasegawa et al. showed that the block chain in the lamellar structure is stretched to the perpendicular direction to the phase interface, whereas it is shrunk along the direction parallel to the domain interface so as to keep the volumes occupied by their segments unchanged.[21,22] The results of such scattering measurements show the spatially averaged chain conformation; therefore, it has been difficult to estimate the conformation at a specific point such as the defect of the phase separation structure. Recently the combined method of the experiments and numerical simulation allowed us to estimate the chain conformation at a particular point in the real domain.[23,24] Morita et al. used the information on the lamellar domain experimentally obtained from the transmission electron microtomography as a boundary condition for the self-consistent field simulation and estimated the single block chain conformation in the bent lamella at the grain boundary.[23] They reported that the block chain at the inner interface, which was bent toward the block chain, stretched out compared to that at the outer interface. However, the direct measurement of the conformation of the block copolymer chain has not been reported because of the difficulty of the experiment.

In contrast to the scattering and the numerical method, real space imaging of the individual chains is expected to provide us the clear evidences on the chain conformation. To observe the block chain conformation in the phase-separated structure, a novel technique to distinguish the objective polymer chain from its surrounding ones is required. Fluorescence technique is the versatile one in the studies

of the polymer conformation and morphology.[25-27] The introduction of a small amount of fluorescent chromophores into the target polymers enables us to image the single fluorescence polymer chains owing to the high sensitive fluorescence detection. However, the spatial resolution of conventional fluorescence microscopy is limited to a half of the wavelength of light by the diffraction barrier.[28] This has limited its application for the single chain imaging except huge bio-macromolecules such as DNA.[29,30] Scanning near-field optical microscopy (SNOM) is a novel technique for achieving a high spatial resolution beyond the diffraction limit of light.[31,32] SNOM is a scanning probe microscopy technique, which is equipped with the probe tip having an aperture smaller than the wavelength of excitation light. The near-field light emanating from such a small aperture is confined in the vicinity of the probe tip end, which enables us to focus the light in a nanometric area of a sample surface. Therefore, SNOM is one of the most suitable methods for investigating the polymer chain conformation in a bulk medium[33] and has been widely applied to many fields in polymer science such as studies on phase separation in polymer blend[35,36] and the ordered structure of block copolymers.[37-39]

In the current chapter, the conformation of PiBMA block chain in poly(octadecyl methacrylate)-*block*-poly(isobutyl methacrylate) (PODMA-*b*-PiBMA) monolayer is discussed. The single PiBMA sub-chain was directly observed by SNOM and the conformation is investigated in terms of the PiBMA block from the localization and orientation of the single PiBMA sub-chain in a two-dimensional microphase-separated structure. The curvature dependence of the PiBMA sub-chain localization in the curved lamella and the orientation of the PiBMA sub-chain are examined.

5.2 EXPERIMENTAL SECTION

5.2.1. Synthesis of Diblock Copolymers

Poly(octadecyl methacrylate)-*block*-poly(isobutyl methacrylate) (PODMA-*b*-PiBMA) was synthesized by atom transfer radical polymerization, the chemical structure of which is shown in Figure 5.1a. Isobutyl methacrylate (Tokyo Chemical Industry) was polymerized from the initiator of *p*-toluenesulfonyl chloride (Aldrich) with CuCl(I) (Wako) and 4, 4'-dinonyl-2, 2'-bipyridyl (Aldrich) as the catalyst complex at 70 °C. The obtained polymer, PiBMA, was reprecipitated from toluene into methanol three times and dried in vacuo. The number-average degree of polymerization (DP_n) of the PiBMA part was determined by size exclusion chromatography (D-7000F, Hitachi) with THF as the eluent calibrated by polystyrene (American Polymer Standards) and poly(isobutyl methacrylate) secondary standards (Aldrich). The block copolymerization of octadecyl methacrylate (Tokyo Chemical Industry) was initiated from the chloride terminal of the PiBMA in anisole at 90 °C. The obtained block copolymer was dissolved in chloroform and passed through an alumina column to remove the catalyst

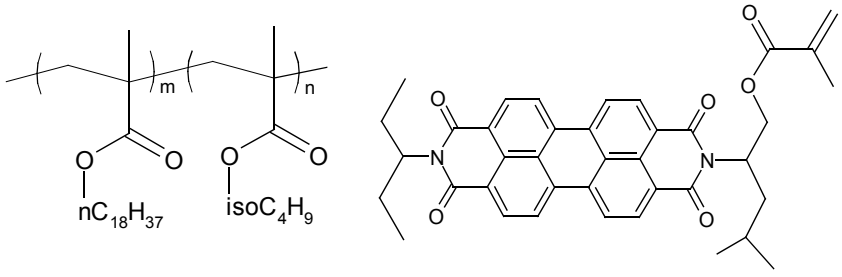

Figure 5.1. Chemical structures of PODMA-*b*-PiBMA (a) and PDI-labeled methacrylate (b).

and reprecipitated from chloroform into methanol three times. For the single block chain observation by SNOM, the author also synthesized the dye-labeled PODMA-*b*-PiBMA, the PiBMA sub-chain of which was selectively labeled with perylene diimide derivative (PDI). The PDI-labeled PiBMA (P(iBMA/PDI)) was prepared by the random copolymerization of isobutyl methacrylate and PDI-labeled methacrylate (Figure 5.1b) by the same procedure as the unlabeled PiBMA. The block copolymerization of octadecyl methacrylate from P(iBMA/PDI) yielded the PDI-labeled PODMA-*b*-PiBMA (PODMA-*b*-P(iBMA/PDI)). The degree of polymerization of the PODMA block was estimated from the molar ratio of isobutyl and octadecyl groups by the 400-MHz ^{1}H NMR (JNM-EX400, JEOL) measurement. The fraction of the fluorescent moiety, *f*, introduced into the polymer chain was evaluated by UV-Vis absorption (U3500, Hitachi) spectra. Characterization of the sample polymer is summarized in Table 5.1.

Table 5.1. Characterization of sample polymers

	$DP_n / 10^3$		*f* / %
	PODMA	PiBMA	
PODMA-*b*-PiBMA	1.98	2.02	
PODMA-*b*-P(iBMA/PDI)	2.08	1.94	0.90[a]

[a] The fraction in the PiBMA part.

5.2.2. Monolayer Preparation

A monolayer of PODMA-*b*-PiBMA was prepared by the Langmuir-Blodgett method. A mixed benzene solution of the dye-labeled and unlabeled PODMA-*b*-PiBMA's at a total concentration of 0.05 g L^{-1} was spread on ultra-pure water (NANOpure II, Barnstead) at 20 °C. The ratio of the labeled polymer to the unlabeled one was in the concentration range from 0.1 to 0.5 wt% to observe the individual

labeled chains separately. After the solvent was evaporated, the temperature of the subphase was raised to 40 °C and kept constant for 3 h for promoting the phase separation on the water surface. After cooling the temperature of the subphase to 20 °C, the phase separated monolayer was compressed by Teflon bars up to a surface pressure of 5 mN m^{-1}. The monolayer of PODMA-*b*-PiBMA was transferred by vertical dipping onto a glass substrate.

5.2.3. SNOM Measurement

SNOM imaging was performed using a cantilever probe with a 60-nm aperture (α-SNOM, WITec). All the SNOM measurements were carried out by the same cantilever in an ambient condition. The sample film was scanned in a contact mode. A 532-nm laser beam (GSHG-3015, Kochi Toyonaka Giken) was coupled to the sub-wevelength aperture to generate the optical near-field for the excitation of the perylenediimide moiety in the samples. The signal light from the sample was collected by a microscope objective (60×, 0.80NA, Nikon) from the backside of the substrate and guided to an avalanche photo diode (SPCM-AQR-14, Perkin Elmer) after passing through two long-pass filters (LP02-532RS-25, Semrock) to acquire the fluorescence image. The surface topography was obtained simultaneously with the fluorescence image.

5.3. RESULTS AND DISCUSSION

5.3.1. AFM Measurement

The microphase-separated structure of a PODMA-*b*-PiBMA monolayer can be observed in the surface topography because of the height difference between the PiBMA and PODMA domains of ca. 2 nm.[40,41] Figure 5.2 shows the topography images of the

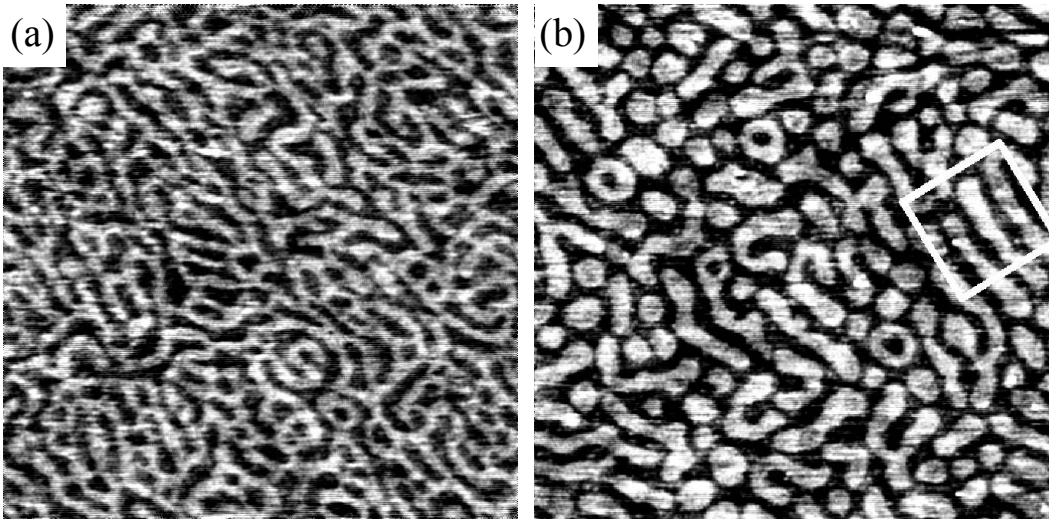

Figure 5.2. AFM images for the PODMA-*b*-P(iBMA/PDI)/PODMA-*b*-PiBMA mixture monolayer before (a) and after (b) annealing. The dimension of images is 5 × 5 μm.

phase-separated PODMA-*b*-PiBMA monolayers before and after annealing, which were obtained using a sharp cantilever probe. The bright area corresponds to the PODMA domain which has a larger thickness than PiBMA, indicating the clear phase-separated structure with a regular spacing. A monolayer of the block copolymer before annealing forms a network-like structure but that after annealing forms a disordered lamellar structure. The domain spacing after annealing was larger than that before annealing. From the fast Fourier transform analysis, the domain spacings of the phase separation structures before and after annealing were evaluated to be 260 nm and 360 nm, respectively. In spreading the polymer solution on water at 20 °C, the PODMA block chains aggregate with each other and form the solid-like domain since the octadecyl group crystallizes below 30 °C.[42] Therefore, the topographic image of a monolayer of the block copolymer before annealing shows the structure frozen in a non-equilibrium state. At the annealing temperature of 40 °C, the crystallized octadecyl group melts and

the PODMA block can behave as a liquid-like monolayer, resulting in the evolution of the phase separation to form a lamellar structure with the large domain size. The parallel lamellar structure is the most stable for the symmetric diblock copolymer system.[2] However, as shown in the square in Figure 5.2b, parallel lamella was observed in the length scale less than a few micrometers. The polymer chain in a monolayer cannot diffuse freely in two dimensions because it is not allowed to have a crossover among the other chains. Therefore, it is difficult to rearrange the block chain to the most energetically favorable position. Consequently, the most parts of the lamellar structure showed the bent lamellar structure with constant domain spacing.

5.3.2. SNOM Imaging of a Single PiBMA Sub-chain

Figure 5.3 shows the SNOM images of a PODMA-*b*-PiBMA monolayer after annealing, where a small amount of the dye-labeled chains were dispersed. The disordered lamella of the microphase-separated structure can be seen in the surface topography of Figure 5.3a. In this topography, the PODMA domain is observed to be wider compared to that shown in Figure 5.2b, because this image was obtained using an apertured probe. The apex of the SNOM probe is not sharp, resulting in the broadening of the higher domain. Figure 5.3b shows the fluorescence SNOM image, where the P(iBMA/PDI) block chain was observed as a bright fluorescent spot. The number of the spots well agreed with the calculated value of the P(iBMA/PDI) block chain from the surface area and the degree of the polymerization,[33] indicating that each fluorescence spot is corresponding to the individual P(iBMA/PDI) sub-chain. Figure 5.3c is the superimposed image of Figures 5.3a and 5.3b, showing that the bright spot in the fluorescence image is located in the PiBMA domain. The single block chain in the microphase-separated structure of the PODMA-*b*-PiBMA monolayer was clearly observed by SNOM.

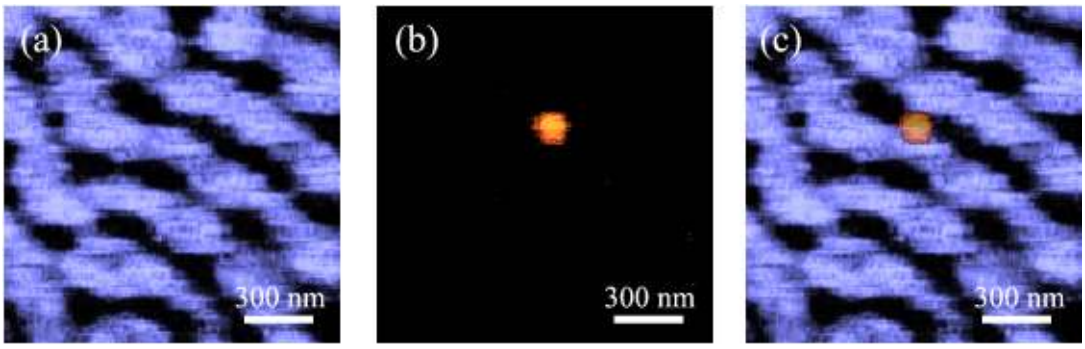

Figure 5.3. Topographic (a), fluorescence (b), and superimposed (c) SNOM images of the same scanning area in the PODMA-*b*-P(iBMA/PDI)/PODMA-*b*-PiBMA monolayer. The light and dark parts in (a) correspond to PODMA and PiBMA, respectively. The bright spot in (c) corresponds to a single P(iBMA/PDI) block chain. The superimposed image (c) shows the P(iBMA/PDI) block chain in the microphase-separated structrue.

Now the relative position of the PiBMA block chain in the PiBMA domain is discussed. The location of the single PiBMA block chains was evaluated as the first moment of the fluorescence intensity distribution.

$$\mathbf{r}_0 = \frac{1}{I_0} \sum_j I_j \mathbf{r}_j \,, \tag{5.1}$$

$$I_0 = \sum_j I_j \,,$$

where I_j and $\mathbf{r}_j$ are the fluorescence intensity and the position vector for the j-th pixel, respectively. Since the dye moiety is randomly introduced along the main chain of the labeled polymer, $\mathbf{r}_0$ corresponds to the center of mass (CM) of the PiBMA block chain in the two-dimensional plane. The relative location of the CM of a PiBMA block to the lamellar domain was determined by the following procedure. The CM of the PiBMA chain was located in the simultaneously obtained topographic SNOM image and the line passing through the CM was drawn in the direction normal to the domain interface. The author defined the origin as the middle point of the PiBMA domain on the above line

and measured the distance from the origin to the CM. As mentioned above, the PODMA-*b*-PiBMA monolayer does not form a long-range lamellar structure; therefore, the curvature of the interface should be taken into account. The absolute value of the curvature κ was defined as the reciprocal of the radius of the most fitted circle to the domain interface nearer to the CM of the chain. A positive value of κ denotes that the center of the fitted circle is located at the same side as the chain relative to the interface, and a negative κ means the opposite side as shown in Figure 5.4. In other words, the positive κ means that the interface is bent towards the PiBMA block chain, and vice versa. Figure 5.5a shows the histogram of the CM location of the PiBMA block chains in the parallel lamella, which shows the interface with $|\kappa| < 0.3\ \mu m^{-1}$. It shows that the CM is not homogeneously distributed in the PiBMA domain and the peak positions of the CM population located at the middle between the PiBMA domain center and the PiBMA/PODMA interface. This result suggests that the block chains with about half length of the PiBMA domain form the two-dimensional parallel lamellar structure as shown in Figure 5.5b.

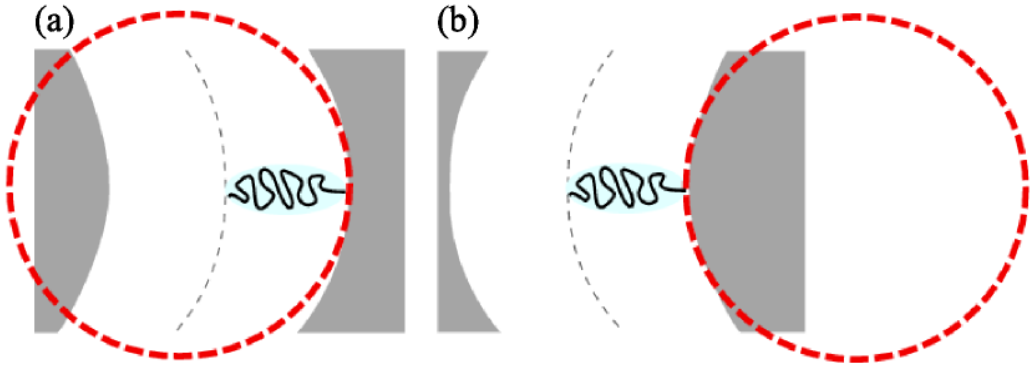

Figure 5.4. Schematic illustration of the positive curvature ($\kappa > 0$) (a) and the negative curvature ($\kappa < 0$). The representative circle is the most fitted one to the domain interface nearer to the CM of the block chain.

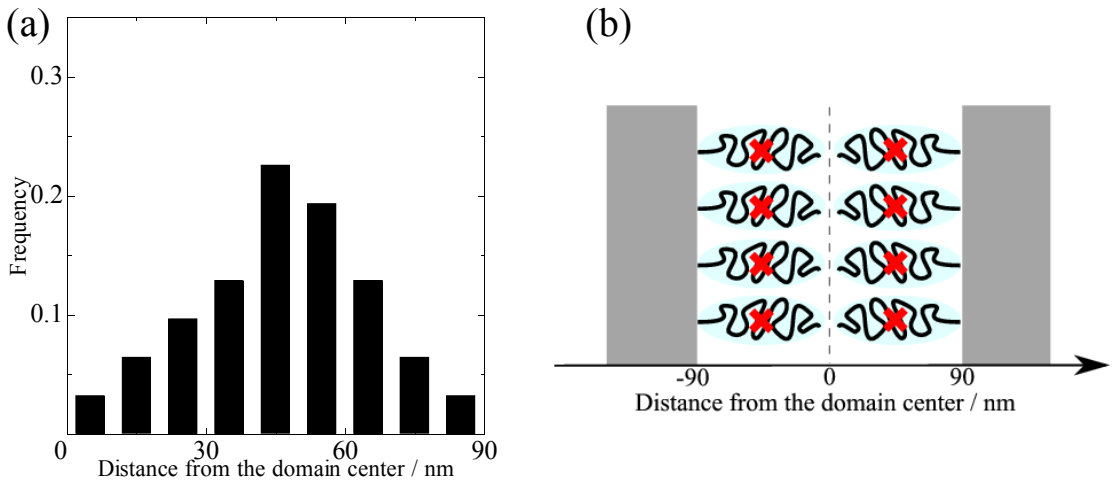

Figure 5.5. Histogram of the localization of PiBMA block chains in the parallel lamella (a) and schematic illustration of the lamellar structure (b). The red crosses in (b) represent the CM of the block chains.

5.3.3. Curvature Dependence of PiBMA Sub-Chain Localization

Figure 5.6 shows the histogram of the localization of the PiBMA sub-chain sub-chain at the bent interface. The CM positions in the bent lamellar domain are located between the PiBMA domain center and PiBMA/PODMA interface, suggesting that the two-dimensional bent lamellar structures are also composed of the block chains confronting one another. However, the peak position of the histogram is different from that for the parallel lamella (Figure 5.5a). In the case of $\kappa > 0$, the peak position of the CM population was shifted toward the the PiBMA domain center, suggesting that the PiBMA sub-chain takes a more stretched conformation than that in the parallel lamella. On the other hand, in the case of $\kappa < 0$, the peak position of the CM population was shifted toward the PiBMA/PODMA interface. This result implies that the PiBMA block chain in the bent lamella with $\kappa < 0$ takes a less stretched conformation than that in the parallel lamella. The conformation of the single block chain in two-dimensional lamella is schematically illustrated in Figure 5.7. Figure 5.8 shows the relationship between the

interfacial curvature and the CM location of the individual block chains. The CM position of the PiBMA block chains depends on the magnitude of the interfacial curvature and shifts toward the PiBMA domain center with increasing κ. This result indicates that the block chain in the two-dimensional lamella takes a more stretched conformation at the interface with large κ.

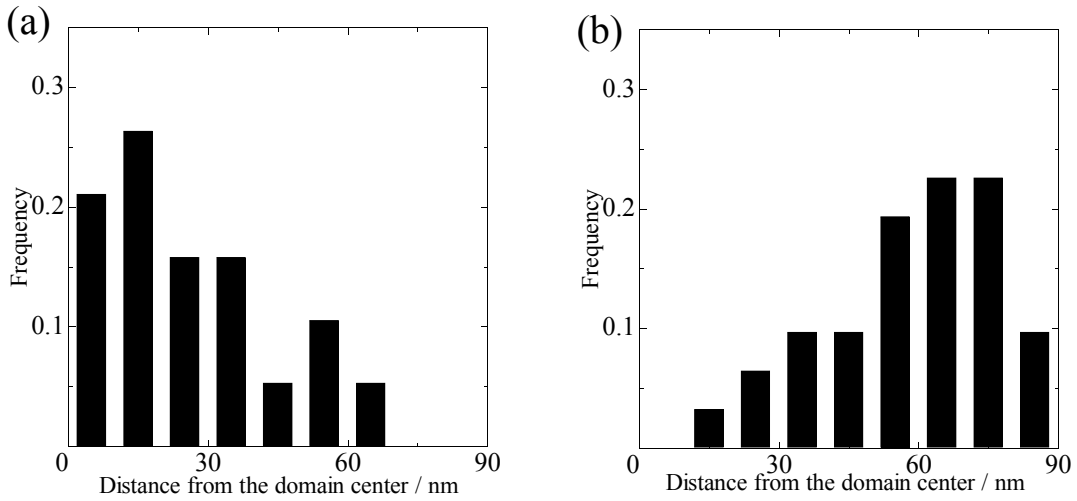

Figure 5.6. Histograms of the localization of PiBMA block chains in the bent lamellae with $\kappa > 0$ (a) and $\kappa < 0$ (b).

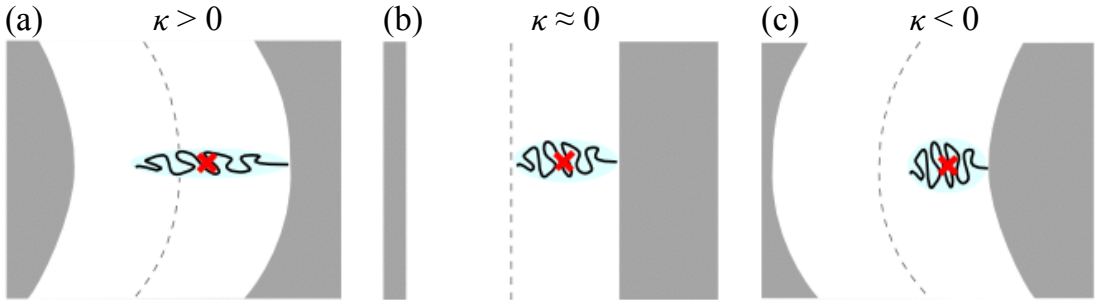

Figure 5.7. Schematic illustration of the conformation of the PiBMA block chains in the lamellae with (a) $\kappa > 0$, (b) $\kappa \approx 0$, and (c) $\kappa < 0$. The red crosses represent the CM of the block chains.

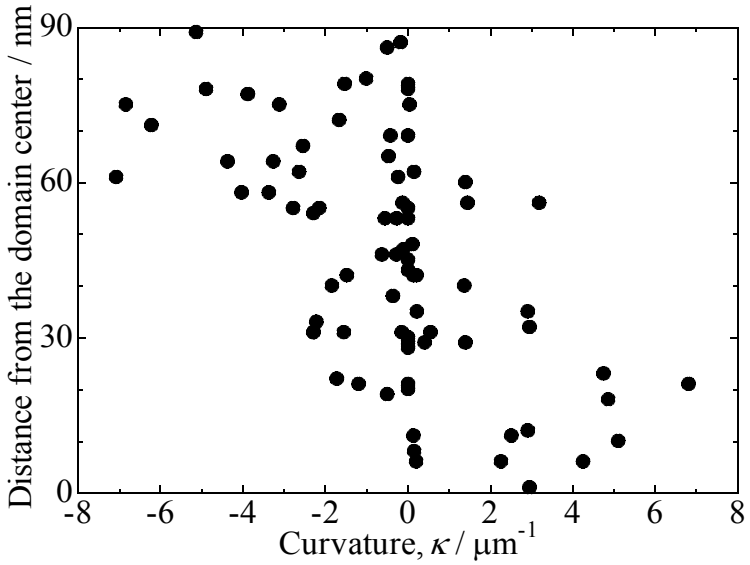

Figure 5.8. Relationship between the interfacial curvature and the distance from the PiBMA domain center to the CM of the PiBMA block chains. Each point corresponds to a single polymer chain.

5.3.4. Relative Orientation of PiBMA Sub-Chain

The orientational angle of the PiBMA block chain to the lamella interface was determined as follows. The investigated polymer chain was coarse-grained as an ellipse, and the relative orientation of the PiBMA block chain was evaluated as the angle, θ, between the long principal axis of the ellipse and the normal line against the domain interface.[43] Figure 5.9 shows the relationship between the interfacial curvature and the orientational angle of the PiBMA chains. The PiBMA block chain in the bent lamellar with $\kappa > 0$ shows the preferential orientation of $\theta < 30$ °. This result indicates that the block chains in the bent lamella with $\kappa > 0$ takes a stretched conformation toward the perpendicular direction to the domain interface. On the other hand, the PiBMA block chain shows the random orientation in the bent lamella with $\kappa < 0$, indicating that the PiBMA block chain in the bent lamella with $\kappa < 0$ has more orientational freedom than that in the bent lamella with $\kappa > 0$.

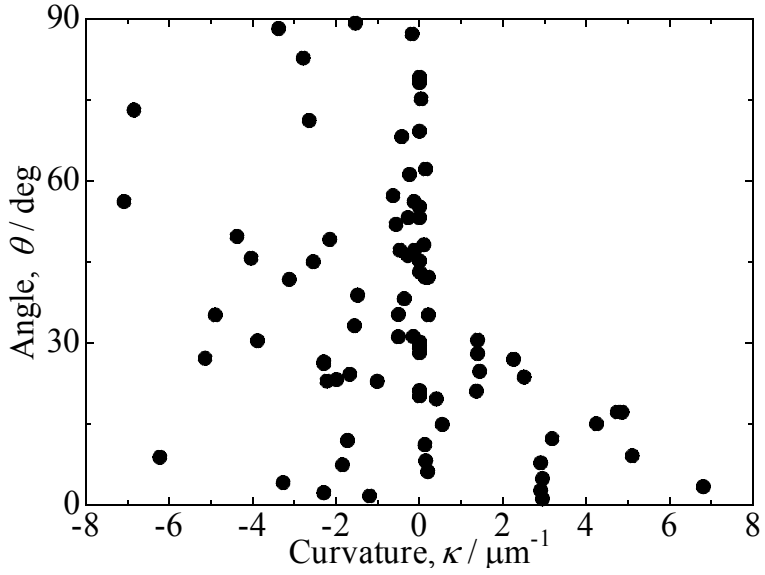

Figure 5.9. The relationship between the interfacial curvature and the orientational angle of PiBMA block chain in the PiBMA domain.

In a three-dimensional microphase-separated structure of diblock copolymers, the polymer chain takes an anisotropic conformation, which is slightly stretched in the perpendicular direction to the phase boundary.[21,22] This is due to the steric hindrance among the block chains aligned at the domain boundary. However, since the chain stretching can be partially relaxed by the mixing among the neighboring chains; therefore, the anisotropy of the chain conformation is as small as 2.[21,22] On the other hand, the previous studies suggested that the polymer chain in a monolayer took a significantly stretched conformation.[13-15] In the current case, the PiBMA sub-chain is estimated to have a conformation as large as 6 × 90 nm considering the occupation area of a single chain and the lamella size of the phase separation structure. In such a two-dimensional system, the polymer chain is not allowed to have the crossover with the other chains, indicating few interlaces among the polymer chains. Therefore, the steric hindrance among the chains located at the domain boundary would be relaxed only by

stretching in the perpendicular direction to the interface. When the domain interface is bent toward the PiBMA domain ($\kappa > 0$), the steric hindrance increases due to the reduction of the interstice among the neighboring PiBMA sub-chains. The hindrance would be reduced by the more stretched chain conformation. Consequently, the CM position of the PiBMA sub-chain is located away from the domain interface and the chain is highly oriented perpendicular to the interface for the positive curvature. On the other hand, at the domain interface with the negative curvature, the reduction of the hindrance between the PiBMA sub-chains causes a less stretched conformation, resulting in the random chain orientation.

5.4. CONCLUSION

The conformation of the single PiBMA block chain in a two-dimensional PODMA-*b*-PiBMA lamella was studied by SNOM. The real space imaging by SNOM allow to discuss the conformation of the individual block chains at the local point in the phase-separated structure. It was found that the CM position and the orientation of the PiBMA sub-chain in the lamellar structure were dependent on the curvature of the PiBMA/PODMA interface. The CM position of the block chain in the lamella with $\kappa > 0$ shifted toward the domain center with increasing κ and the block chain oriented perpendicularly to the domain interface, indicating that the block chain takes a more stretched conformation as the interfacial curvature increases. In the case of $\kappa < 0$, the CM position of block chain was closer to the domain interface when the κ was smaller. The block chain had random orientation irrespective of the magnitude of the interfacial curvature. These result from the less stretched conformation of the block chains compared with the conformation in the lamella with $\kappa > 0$. The steric hindrance among the chains located at the domain interface causes the different conformations of the

block chains in the lamellae. The direct observation of the single block chain provides the further insight about the chain conformation in the phase separated structure.

References

1. I. W. Hamley, "*The Physics of Block Copolymers*", Oxford University Press, New York (1998).
2. F. S. Bates and G. H. Fredrickson, *Annu. Rev. Phys. Chem.*, **41**, 525 (1990).
3. L. Leibler, *Macromolecules*, **13**, 1602 (1980).
4. T. Ohta and K. Kawasaki, *Macromolecules*, **19**, 2621 (1986).
5. J. Cho, *Macromolecules*, **34**, 1001 (2001).
6. Y. Matsushita, K. Mori, R. Saguchi, Y. Nakao, I. Noda, and M. Nagasawa, *Macromolecules*, **23**, 4313 (1990).
7. T. Wolff, C. Burger, and W. Ruland, *Macromolecules*, **26**, 1707 (1993).
8. M. F. Schulz, A. K. Khandpur, F. S. Bates, K. Almdal, K. Mortensen, D. A. Hajduk, and S. M. Gruner, *Macromolecules*, **29**, 2857 (1996).
9. K. Niihara, H. Sugimori, U. Matsuwaki, F. Hirato, H. Morita, M. Doi, H. Masunaga, S. Sasaki, and H. Jinnai, *Macromolecules*, **41**, 9318 (2008).
10. G. Krausch, *Mater. Sci. Eng. R-Rep.*, **14**, 1 (1995).
11. M. J. Fasolka, and A. M. Mayes, *Annu. Rev. Mater. Res.*, **31**, 323 (2001).
12. P. F. Green and R. Limary, *Adv. Colloid Interface Sci.*, **94**, 53 (2001).
13. J. Kumaki and T. Hashimoto, *J. Am. Chem. Soc.*, **120**, 423 (1998).
14. S. Kadota, K. Aoki, S. Nagano, and T. Seki, *J. Am. Chem. Soc.*, **127**, 8266 (2005).
15. S. Kadota, K. Aoki, S. Nagano, and T. Seki, *Colloids Surf. A*, **284-285**, 535 (2006).
16. R. W. Richards and J. L. Thomason, *Polymer*, **22**, 581 (1981).
17. Y. Matsushita, K. Mori, Y. Mogi, R. Saguchi, I. Noda, M. Nagasawa, T. Chang, C. J. Glinka, and C. C. Han, *Macromolecules*, **23**, 4317 (1990).
18. N. Torikai, Y. Matsushita, S. Langridge, D. Bucknall, J. Penfold, and M. Takeda, *Physica B*, **283**, 12 (2000).
19. L. Wu, T. P. Lodge, and F. S. Bates, *Macromolecules*, **39**, 294 (2006).

20. S. Koizumi and T. Hashimoto, *Physica B*, **213**, 703 (1995).
21. H. Hasegawa, T. Hashimoto, H. Kawai, T. P. Lodge, E. J. Amis, C. J. Glinka, and C. C. Han, *Macromolecules*, **18**, 67 (1985).
22. H. Hasegawa, H. Tanaka, T. Hashimoto, and C. C. Han, *Macromolecules*, **20**, 2120 (1987).
23. H. Morita, T. Kawakatsu, M. Doi, T. Nishi, and H. Jinnai, *Macromolecules*, **41**, 4845 (2008).
24. K. S. Lyakhova, A. V. Zvelindovsky, G. J. A. Sevink, and J. G. E. M. Fraaije, *J. Chem. Phys.*, **118**, 8456 (2003).
25. M. A. Winnik, ed. "*Photophysical and Photochemical Tools in Polymer Science*", Reidel, Dordrecht (1985).
26. T. Tanaka, ed. "*Experimental Methods in Polymer Science*" Academic, San Diego (2000).
27. S. Ito and H. Aoki, *Adv. Polym. Sci.*, **182**, 131 (2005).
28. E. Abbe, *Arch. Mikrosk. Anat.*, *9*, 413 (1873).
29. B. Maier and J. O. Rädler, *Phys. Rev. Lett.*, **82**, 1911 (1999).
30. B. Maier and J. O. Rädler, *Macromolecules* **2001**, *34*, 5723-5724.
31. E. Betzig and J. K. Trautman, *Science*, **257**, 189 (1992).
32. M. Ohtsu, ed. "*Near-field Nano/atom Optics and Technology*", Springer, Tokyo (1998).
33. H. Aoki, M. Anryu, and S. Ito, *Polymer*, **46**, 5896(2005).
34. H. Aoki, S. Morita, R. Sekine, and S. Ito, *Polym. J.*, *40*, 274 (2008).
35. H. Aoki, Y. Sakurai, S. Ito, and T. Nakagawa, *J. Phys. Chem. B*, **103**, 10553 (1999).
36. H. Aoki and S Ito, *J. Phys. Chem. B*, **105**, 4558 (2001).
37. H. Aoki, Y. Kunai, S. Ito, H. Yamada, and K. Matsushige, *Appl. Surf. Sci.*, **18**, 534 (2002).

38. M. J. Fasolka, L. S. Goldner, J. Hwang, A. M. Urbas, P. DeRege, T. Swager, and E. L. Thomas, *Phys. Rev. Lett.*, **90**, 016107 (2003).
39. M. B. Raschke, L. Molina, T. Elsaesser, D. H. Kim, W. Knoll, and K. Hinrichs, *ChemPhysChem*, **6**, 2197 (2005).
40. S. J. Mumby, J. D. Swalen, and J. F. Rabolt, *Macromolecules*, **19**, 1054 (1986).
41. K. Naito, *J. Colloid Interface Sci.*, **131**, 218 (1989).
42. T. Nakahara, K. Motomura, and R. Matuura, *J. Polym. Sci. A-2*, **4**, 649 (1966).
43. T. Ube, H. Aoki, S. Ito, J. Horinaka, and T. Takigawa, *Polymer*, **48**, 6221 (2007).

Chapter 6

Chain End Distribution Block Copolymer in Two-Dimensional Microphase-Separated Structure Studied by Scanning Near-Field Optical Microscopy

6.1. INTRODUCTION

Block copolymers are well known to form a variety of the ordered nano-structures via self-organization.[1,2] Since such nano-structures have the potential for practical application,[3] the morphology of block copolymers has been extensively explored in thin films as well as in bulk.[4-9] With decreasing the film thickness, the effect of the spatial confinement on polymer chains increases. Therefore, the behavior of polymers in thin films differs appreciably from that in bulk.[10-12] A polymer monolayer prepared by Langmuir-Blodgett technique has a molecularly ultimate thickness because the main chain consisting of amphiphilic groups is adsorbed on the water surface. Thus, polymer monolayer can be regarded as a model of two-dimensional system of polymers. The two-dimensional microphase-separated structures deposited on a substrate are reported by several researchers.[13-15] The domain size in two dimensions was significantly larger than that in three-dimensional systems, suggesting that the chain conformation in the domains is different from three-dimensional one. To understand the chain conformation in more detail, the segment distribution of the specific parts of the block copolymers forming the phase-separated structure is a helpful information. Therefore, the localization of block segments has been investigated by small-angle neutron scattering,[16] neutron reflectivity,[17-19] and the energy transfer technique.[20] Several research groups reported that the partial segments near the free-end of block copolymers

were localized at the center of lamellae with a fairly wide distribution, while the segments of block chain adjacent to the chemical junction point are strongly localized at the lamellar interface.[17-20] Computational studies also showed the similar results.[21,22]

In contrast to such techniques, the direct observation is expected to provide clear evidences on the polymer nano-structure. In the past, direct observation of the two-dimensional morphology of polymer monolayers has been carried out so far by Brewster angle microscopy [23,24] and atomic force microscopy.[25,26] Recently, scanning near-field optical microscopy (SNOM) has attracted much attention from researchers in various field. SNOM is an emerging scanning probe technique, which allows optical measurement with high resolution beyond the diffraction limit of light.[27-29] SNOM is equipped with the probe tip having an aperture smaller than the wavelength. The light incidence to the aperture generates an optical near-field restricted in the space of the aperture size, which allows one to illuminate the nanometric space under the sample surface. The introduction of a small amount of fluorescence chromophores into the specific segments in a polymer chain allows us to obtain the information on the location of the chain segment in a nanometer scale.[30-33] Thus, SNOM is expected to be a suitable method for investigating the segment distribution of the block copolymer in a two-dimensional phase-separated structure.

In this chapter, the spatial distribution of the chain end of the poly(isobutyl methacrylate) (PiBMA) in a two-dimensional microphase-separated structure of poly(octadecyl methacrylate)-*block*-poly(isobutyl methacrylate) (PODMA-*b*-PiBMA) diblock copolymer was observed by SNOM. Through the comparison with the distribution of the PiBMA block of PODMA-*b*-PiBMA, the PiBMA chain end distribution is discussed.

6.2. EXPERIMENTAL SECTION

6.2.1. Synthesis of Diblock Copolymers

Two kinds of dye-labeled PODMA-*b*-PiBMA diblock copolymers were synthesized: a single perylene diimide derivative (PDI) molecule is tagged at the free end of the PiBMA sub-chain (PODMA-*b*-PiBMA-PDI), and the dye moiety is randomly introduced along the contour of the PiBMA sub-chain (PODMA-*b*-P(iBMA/PDI)). The chemical structures of the labeled PODMA-*b*-PiBMAs are shown in Figure 6.1. The end-labeled PiBMA was synthesized by atom transfer radical polymerization of isobutyl methacrylate (iBMA) with CuCl(I)/4, 4'-dinonyl-2, 2'-bipyridyl at 70 °C from the initiating agent having the PDI moiety. The raw polymer obtained after the polymerization was reprecipitated from toluene into methanol three times and dried in

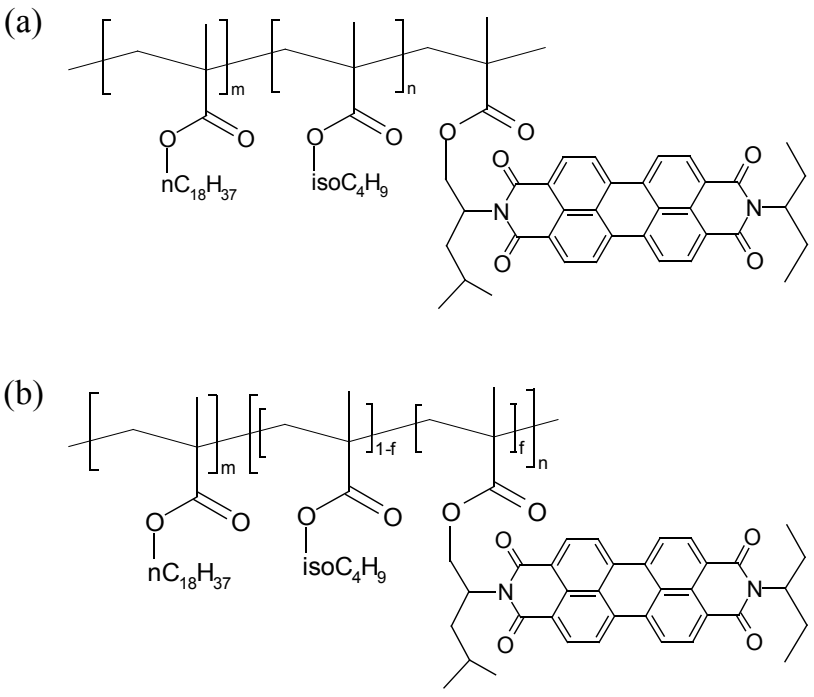

Figure 6.1. Chemical structures of PODMA-*b*-PiBMA-PDI (a), PODMA-*b*-P(iBMA/PDI) (b).

vacuo. The degree of polymerization (DP) of the PiBMA part was determined by size exclusion chromatography (D-7000F, Hitachi) with THF as the eluent calibrated by polystyrene (American Polymer Standards) and poly(isobutyl methacrylate) secondary standards (Aldrich). The block copolymerization of octadecyl methacrylate (ODMA) was carried out using CuCl(I) and 4, 4'-dinonyl-2, 2'-bipyridyl from the end-labeled PiBMA in anisole at 90 °C, yielding PODMA-*b*-PiBMA-PDI. PODMA-*b*-P(iBMA/PDI) was prepared by the random copolymerization of iBMA and PDI-labeled methacrylate followed by the block copolymerization of ODMA, where the polymerization condition was the same as PODMA-*b*-PiBMA-PDI. The number of the fluorescent moiety, N_f, introduced into the polymer chain was evaluated by UV-Vis absorption (U3500, Hitachi) before block copolymerization of ODMA. The obtained block copolymer was dissolved in chloroform and passed through an alumina column to remove the catalyst. The block copolymer was reprecipitated from chloroform into methanol three times and was dried in vacuo. The degree of polymerization of the PODMA block was evaluated from the molar ratio of ODMA and iBMA by 400-MHz ^{1}H NMR (JNM-EX400, JEOL) measurements. Characterization of the sample polymer is summarized in Table 6.1.

Table 6.1. Characterization of sample polymers

	$DP_n / 10^3$		N_f[a]
	PODMA	PiBMA	
PODMA-*b*-PiBMA-PDI	2.26	1.98	1
PODMA-*b*-P(iBMA/PDI)	1.86	1.71	15

[a] The Number of the fluorescent moiety in the PiBMA part.

6.2.2. Monolayer Preparation

A microphase-separated monolayer of PODMA-*b*-PiBMA was prepared by the Langmuir-Blodgett method. A benzene solution of the block copolymers at a concentration of 0.05 g L^{-1} was spread on ultra-pure water (NANOpure II, Barnstead) at 20 °C to form a monolayer on the water surface. After the solvent was evaporated, the temperature of the subphase was raised to 40 °C and kept constant for 3 h for promoting the microphase separation on the water surface. After cooling the temperature of the subphase to 20 °C, the phase-separated monolayer was compressed by Teflon bars up to a surface pressure of 5 mN m^{-1} at a speed of 10 mm min^{-1}. The phase-separated monolayer of PODMA-*b*-PiBMAs was transferred by vertical dipping onto a glass substrate.

6.2.3. SNOM Measurement

SNOM imaging was performed using a cantilever probe with a 60-nm aperture (α-SNOM, WITec). All SNOM measurements were carried out by the same cantilever in an ambient condition. The sample film was scanned in a contact mode. A 532-nm laser beam (GSHG-3015, Kochi Toyonaka Giken) was coupled to the sub-wevelength aperture to generate the optical near-field for the excitation of the PDI moiety in the samples. The signal light from the sample was collected by a microscope objective (60 ×, 0.80NA, Nikon) from the backside of the substrate and guided to a photomultiplier (H8631, Hamamatsu Photonics) after passing through two long-pass filters (LP02-532RS-25, Semrock) to acquire the fluorescence image.

6.3 RESULTS AND DISCUSSION

6.3.1. AFM Measurement

Figure 6.2 shows a topography image of a phase-separated PODMA-*b*-PiBMA-PDI monolayer. The two-dimensional microphase-separated structure was observed in the surface topography because there is a ca. 2 nm thickness difference between PiBMA and PODMA monolayers.[34,35] The bright area corresponds to the PODMA domain which has a larger thickness than PiBMA and the disordered lamellar structure with a regular spacing can be seen in Figure 6.2. The fast Fourier transform (FFT) of an image showed a peak corresponding to the domain spacing of 360 nm.

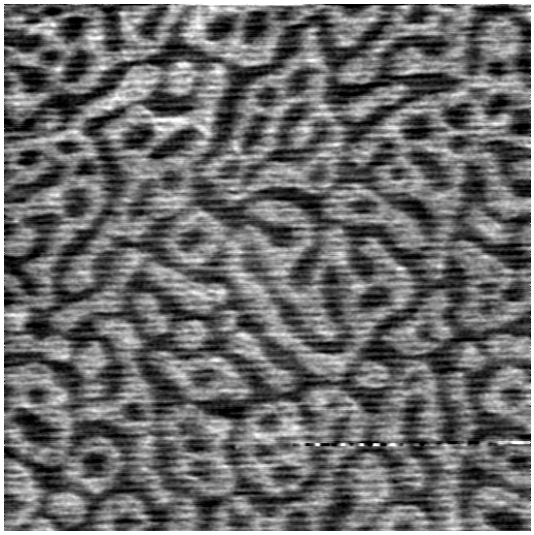

Figure 6.2. Topographic image of phase-separated PODMA-*b*-PiBMA-PDI monolayer.

6.3.2. SNOM Imaging of Microphase-Separated Monolayers

Figures 6.3a and 3b show the fluorescence SNOM images of the phase-separated monolayers of PODMA-*b*-P(iBMA/PDI) and PODMA-*b*-PiBMA-PDI, respectively. In

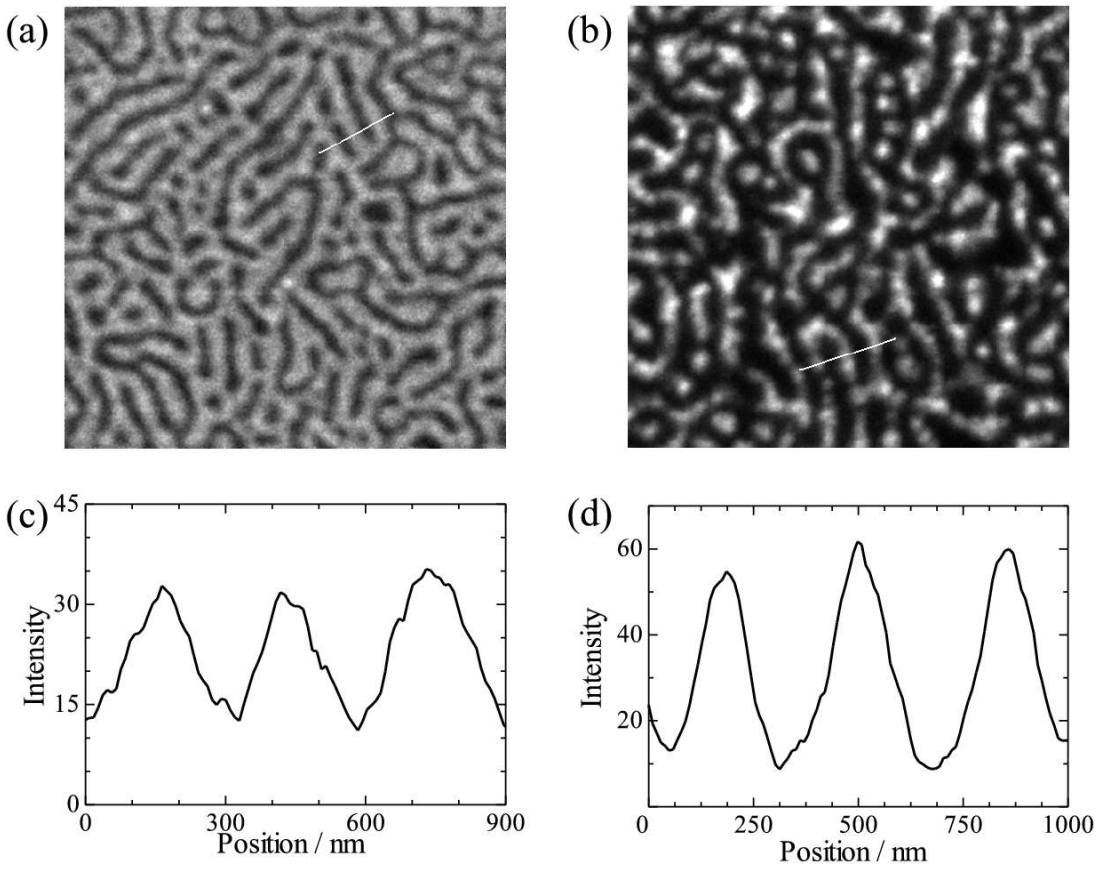

Figure 6.3. SNOM images of a the phase-separated PODMA-*b*-P(iBMA/PDI) (a) and PODMA-*b*-PiBMA-PDI monolayers (b). The dimension of both images is 5× 5μm. The fluorescence intensity profiles are shown in lower panels (c) and (d) obtained from the SNOM images (a) and (b), respectively.

Figure 6.3, the bright area corresponds to the spatial distribution of the PDI molecules. Figure 6.3a indicates the whole segment of the PiBMA chain because the dye moiety is incorporated along the main chain of the PiBMA block. On the other hand, Figure 6.3b depicts the spatial distribution of the chain end of PiBMA. The PiBMA domain appears as large as the PODMA domain in Figures 6.2 and 6.3a, indicating the microphase-separated structure of the symmetric PODMA-*b*-PiBMA. However, Figure 6.3b clearly

shows that the bright areas are smaller than the dark areas. This result suggests that the PiBMA block chain end is not homogeneously distributed in the PiBMA domain. Figures 6.3c and 3d show the signal intensity profiles along the line in Figures 6.3a and 3b, respectively, which were drawn perpendicular to the domain interface. The peak-to-peak (valley-to-valley) distances in Figures 6.3c and 3d were 300 ± 21 nm and 360 ± 18 nm, respectively. These values coincide with the result of the FFT analysis, suggesting that peak-to-peak (valley-to-valley) corresponds to the periodicity of the lamellar spacing of the block copolymer.

6.3.3. Evaluation of Chain End Distribution

The SNOM image corresponds to the convolution of the spatial distribution of the fluorescent object and the point spread function (PSF) of the microscope. Therefore, given the PSF of the microscope and the appropriate spatial distribution function of the fluorophores, one can reconstruct the fluorescence intensity profiles of the SNOM images. In order to determine the PSF of the microscope, the nanocrystal of CdSe, so-called the quantum dot (QD), was observed.[36] The size of QD is less than 10 nm, which is far smaller compared to the aperture size of the SNOM probe. Therefore, the observed fluorescence image of a QD corresponds to the PSF of the imaging system. The one-dimensional fluorescence intensity profile of a single QD in SNOM images was fitted to a modeled function of a sum of two Gaussian profiles

$$I(x) = p\exp\left(-\frac{x^2}{2\sigma_1^2}\right) + (1-p)\exp\left(-\frac{x^2}{2\sigma_2^2}\right), \qquad (6.1)$$

and the best fit parameters, $p = 0.57$, $\sigma_1 = 43$ nm, and $\sigma_2 = 140$ nm, were obtained.

Before the discussion of the PiBMA chain end distribution, the fluorescence intensity profile of the PODMA-*b*-P(iBMA/PDI) system is discussed, where the PDI moiety is homogeneously distributed in the PiBMA domain of the microphase-separated

structure. Since PiBMA and PODMA are incompatible with each other,[37,38] the distribution of the PiBMA block chains can be modeled as Figure 6.4b. At first, the author defined the *x*-axis in the direction perpendicular to the lamellar interface and set the origin at the middle point of the PiBMA domain. When the PiBMA domain has the spacings of $2W$ nm and the *x*-coordinate of the *i*th PiBMA domain center is W_i' nm, the distribution function of the PiBMA block chains along the *x*-axis is modeled as

$$\rho(x)=\sum_i \rho'(x-W_i'), \tag{6.2}$$

$$\rho'(u)=\begin{cases}\rho_0 & (|u|\le W)\\ 0 & (|u|>W)\end{cases}$$

where ρ_0 is the plane density of the PiBMA domain. Now, $2W$ of the phase-separated PODMA-*b*-P(iBMA/PDI) monolayer is 150 nm as mentioned above. Figure 6.4a shows the fluorescence intensity profile of the PODMA-*b*-P(iBMA/PDI) block copolymer. The solid circles represent the experimental data, while the solid line indicates the calculated profile convoluted by the PSF and the assumed distribution function of the PiBMA chains shown in Figure 6.4b. The calculated line gave good agreement with the experimental result, indicating that the fluorescence intensity profile of a SNOM image can be described by the convolution of the PSF of the microscope and the distribution of the PiBMA block chain.

If the PiBMA chain end homogeneously distributes in the PiBMA domain, the distribution function of the PiBMA chain end along the *x*-axis can be described by the equation 6.2. Figure 6.5a shows the fluorescence intensity profile for the PODMA-*b*-PiBMA-PDI copolymer experimentally obtained from a SNOM image (solid circles) and the calculated profile (solid curve), which corresponds to the uniform distribution function of PiBMA chain end with $2W$ = 180 nm shown in Figure 6.5b. Figure 6.5a indicates that the uniform distribution cannot reconstruct the SNOM image and that the

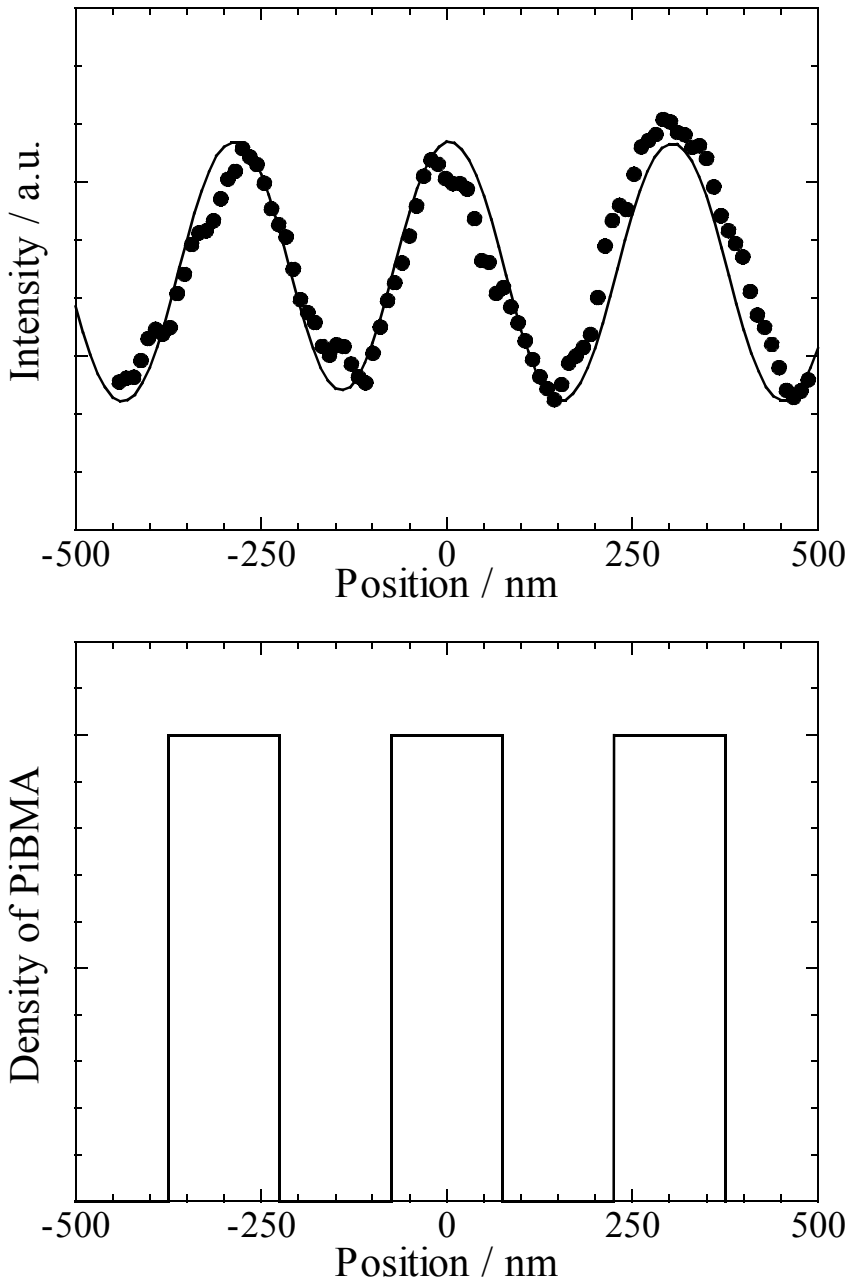

Figure 6.4. A fluorescence intensity profile of the PODMA-*b*-P(iBMA/PDI) block copolymer (solid circles) and a calculated profile (solid line) (a) and the density profile of the PiBMA block (b).

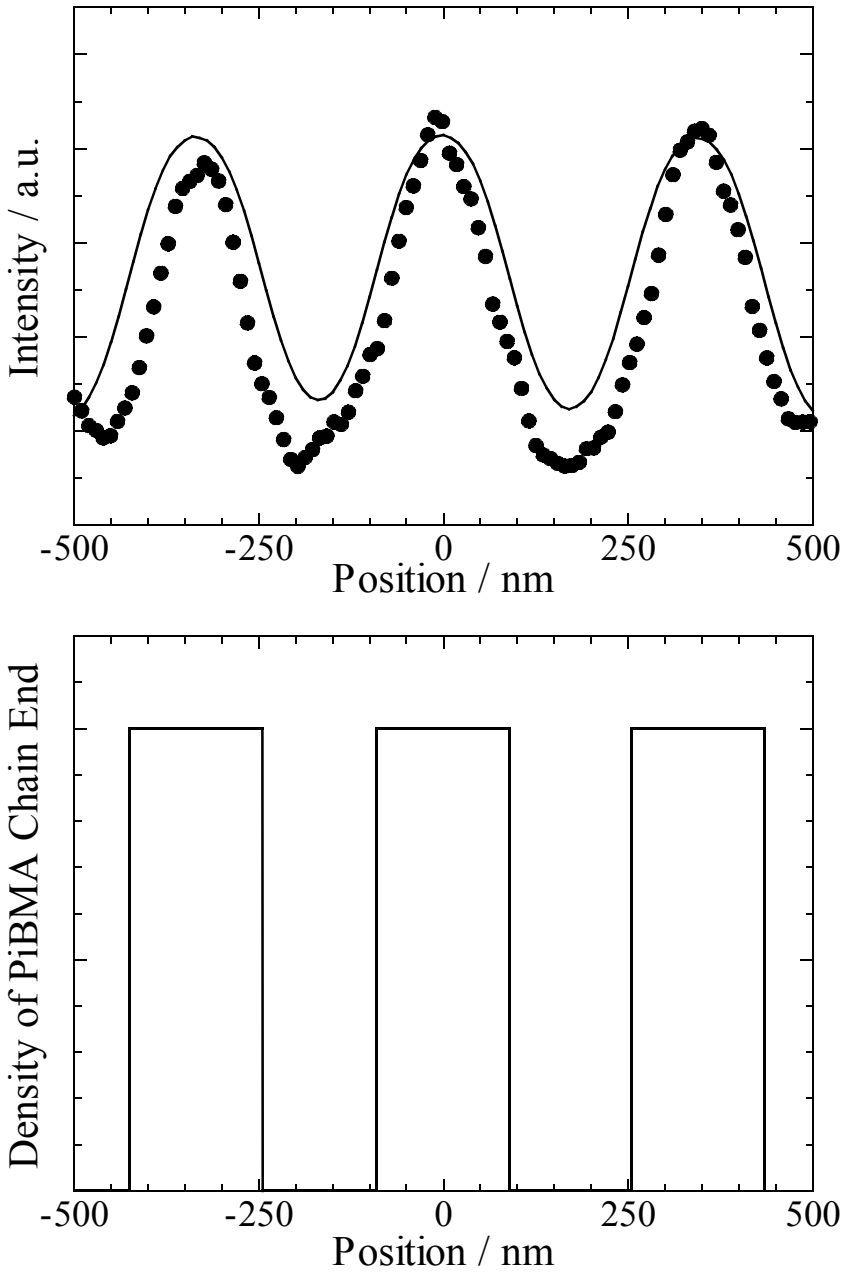

Figure 6.5. A fluorescence intensity profile of the PODMA-*b*-PiBMA-PDI block copolymer (solid circles) and a calculated profile (solid line) (a) and the density profile of the PiBMA chain end (b). The chain end distribution is assumed to be an uniform one.

domain width of the experimentally obtained from the fluorescence intensity profile is smaller than the calculated ones. This result indicates that the PiBMA chain end localizes near the PiBMA domain center. As a probable distribution of the block chain end, the author assumes a Gaussian distribution with a peak at the PiBMA domain center. The distribution function of the PiBMA chain end along the *x*-axis is modeled as

$$\rho(x)=\rho_0\sum_i \exp\left(-\frac{(x-W_i')^2}{2\sigma^2}\right), \tag{6.3}$$

where σ is the standard deviation of the assumed PiBMA chain end distribution. Figure 6.6a shows the experimentally obtained fluorescence intensity profile duplicated from Figure 6.5a (solid circles) and the best-fitted profile calculated from the distribution function shown in Figure 6.6b (solid curve). The standard deviation of the Gaussian distribution in Figure 6.6b was 25 nm. Considering that the PiBMA domain width is 180 nm, it is found that about 70 % of the PiBMA chain ends are contained within the 28 % (2σ) region of the PiBMA domain. In three-dimensions, on the other hand, 70 % of the chain ends was estimated to be contained within the 55–70 % of the domain thickness.[17,19,39] The result in this chapter shows that the PiBMA chain end in a two-dimensional microphase-separated structure is confined in the spatially narrow region near the middle of the PiBMA domain, although the chain end distribution of block copolymers has a concentration maximum at the domain center in both two- and three-dimensional systems.[17-22,39] In three-dimensional system, the chain ends reach back to fill the space in order to maintain uniform density and interlace with other chains. However, in the two-dimensional system the polymer chain is not allowed to have the crossover with the other chains, resulting in few interlaces among the polymer chains. Therefore, the steric hindrance among the neighboring chains would be relaxed only by stretching in the normal direction to the interface. In addition, the steric hindrance among the block chain near the domain interface is larger than that near the domain

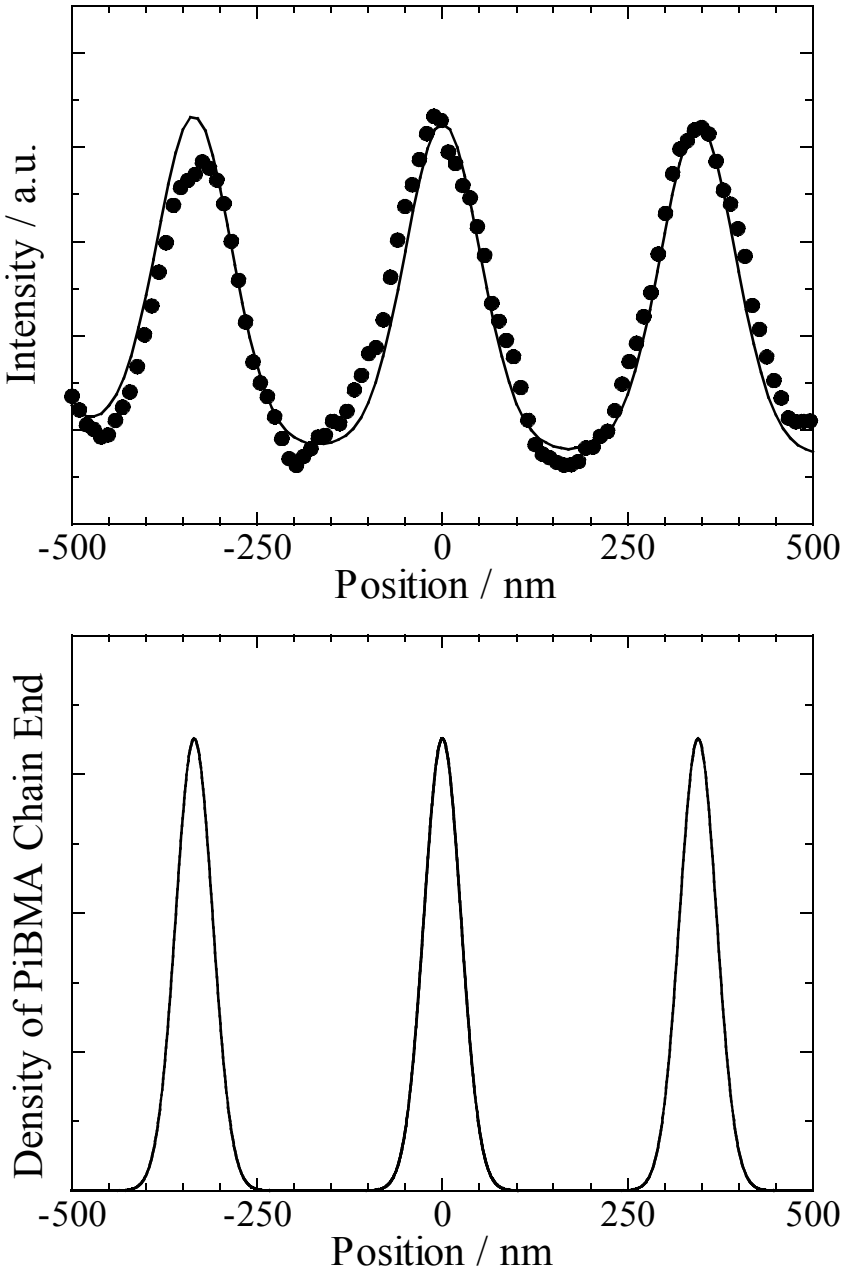

Figure 6.6. A fluorescence intensity profile of the PODMA-*b*-PiBMA-PDI block copolymer (solid circles) and a calculated profile (solid line) (a) and the density profile of the PiBMA chain end (b). The chain end distribution is assumed to be a Gaussian one.

center because the block chains are densely aligned at the domain boundary. Consequently, the PiBMA block chain ends in two-dimensional microphase-separated structure are not homogeneously distributed in the PiBMA domain and tend to localize near the PiBMA domain center.

6.4. CONCLUSION

The chain end distribution of the PiBMA block in a two-dimensional microphase-separated structure formed by PODMA-*b*-PiBMA diblock copolymer was studied by SNOM. The real-space imaging by SNOM allows to discuss the distribution of the specific parts of the block chains in the two-dimensional lamellar structure. The results showed that the chain end distribution of the block copolymer in two dimensions has the peak near the domain center, and the chain ends are confined in the narrower region near the domain center compared with the three-dimensional bulk state.

References and Note

1. I. W. Hamley, "*The Physics of Block Copolymers*", Oxford University Press, New York (1998).
2. F. S. Bates and G. H. Fredrickson, *Annu. Rev. Phys. Chem.*, **41**, 525 (1990).
3. M. Lazzari, G. Liu, and S. Lecommandoux, eds. "*Block Copolymers in Nanoscience*", Wiley-VCH, Weinheim (2006).
4. K. Fukunaga, T. Hashimoto, H. Elbs, and G. Krausch, *Macromolecules*, **35**, 4406 (2002).
5. B. H. Sohn and S. H. Yun, *Polymer*, **43**, 2507 (2002).
6. T. Xu, Y. Xhu, S. P. Gido, and T. P. Russell, *Macromolecules*, **37**, 2625 (2004).
7. D. M. Lambreva, R. Opitz, G. Reiter, P. M. Frederik, and W. H. de Jeu, *Polymer*, **46**, 4868 (2005).
8. Y.-Y. Wang, W. Chen, and T. P. Russell, *Macromolecules*, **41**, 7227 (2008).
9. L. He, L. Zhang, and H. Liang, *J. Polym. Sci. Polym. Phys. Ed.*, **47**, 1 (2009).
10. G. Krausch, *Mater. Sci. Eng. R-Rep.*, **14**, 1 (1995).
11. M. J. Fasolka and A. M. Mayes, *Annu. Rev. Mater. Res.*, **31**, 323 (2001).
12. P. F. Green and R. Limary, *Adv. Colloid Interface Sci.*, **94**, 53 (2001).
13. J. Kumaki and T. Hashimoto, *J. Am. Chem. Soc.*, **120**, 423 (1998).
14. S. Kadota, K. Aoki, S. Nagano, and T. Seki, *J. Am. Chem. Soc.*, **127**, 8266 (2005).
15. S. Kadota, K. Aoki, S. Nagano, and T. Seki, *Colloids Surf. A*, **284-285**, 535 (2006).
16. Y. Matsushita, K. Mori, R. Saguchi, I. Noda,and M. Nagasawa, *Macromolecules*, ***23***, 4387 (1990).
17. A. M. Mayers, R. D. Johnson, T. P. Russell, S. D. Smith, S. K. Satija, and C. F. Majkrzak, *Macromolecules*, **26**, 1047 (1993).
18. N. Torikai, Y. Matsushita, I. Noda, S. Karim, S. K. Satija, and C. C. Han, *Physica B*, **213&214**, 694 (1995).

19. N. Torikai, I. Noda, A. Karim, S. K. Satija, C. C. Han, Y. Matsushita, and T. Kawakatsu, *Macromolecules*, **30**, 2907 (1997).
20. S. Ni, N. Sakamoto, T. Hashimoto, and M. A. Winnik, *Macromolecules*, **28**, 8686 (1995).
21. K. Kawasaki and T. Kawakatsu, *Macromolecules*, **23**, 4006 (1990).
22. J. Yang, M. A. Winnik, and T. Pakula, *Macromol. Theory Simul.*, **14**, 9 (2005).
23. N. Sato, S. Ito, and M. Yamamoto, *Polym. J.*, **28**, 784 (1996).
24. N. Sato, S. Ito, and M. Yamamoto, *Macromolecules*, **31**, 2673 (1998)
25. T. Yuba, S. Yokoyama, M. Kakimoto, and Y. Imai, *Adv. Mater.*, **6**, 888 (1994).
26. R. K. Gupta and K. A. Suresh, *Eur. Phys. J. E*, **14**, 35, (2004).
27. E. Abbe, *Arch. Mikrosk. Anat.*, **9**, 413 (1873).
28. E. Betzig and J. K. Trautman, *Science*, **257**, 189 (1992).
29. M. Ohtsu, ed. "*Near-field Nano/atom Optics and Technology*", Springer, Tokyo (1998).
30. H. Aoki, Y. Kunai, S. Ito, H. Yamada, and K. Matsushige, *Appl. Surf. Sci.*, **18**, 534 (2002).
31. S. Ito and H. Aoki, *Adv. Polym. Sci.*, **182**, 131 (2005).
32. H. Aoki, M. Anryu, and S. Ito, *Polymer*, **46**, 5896 (2005).
33. T. Ube, H. Aoki, S. Ito, J. Horinaka, and T. Takigawa, *Polymer*, **48**, 6221 (2007).
34. S. J. Mumby, J. D. Swalen, and J. F. Rabolt, *Macromolecules*, **19**, 1054 (1986).
35. K. Naito, *J. Colloid Interface Sci.*, **131**, 218 (1989).
36. A thin film (20 nm) of poly(vinyl alcohol) (Wako, degree of polymerization 2000) containing QDs (Qdot 655 ITK, Invitrogen) at an extremely diluted concentration on a glass substrate was prepared by spin-coating.
37. H. Aoki, Y. Sakurai, S. Ito, and T. Nakagawa, *J. Phys. Chem. B*, **103**, 10553 (1999).
38. H. Aoki and S. Ito, *J. Phys. Chem. B*, **105**, 4558 (2001).

39. K. R. Shull, A. M. Mayes, and T. P. Russell, *Macromolecules*, **26**, 3929 (1993).

Chapter 7

Radiation-Induced Fabrication of Polymer Nanoporous Materials from Microphase-Separated Structure of Diblock Copolymers as a Template

7.1. INTRODUCTION

Block copolymers consisting of incompatible chains are known to generate nanoscale microdomains by microphase separation. In linear diblock copolymers the four equilibrium microphase-separated structures have been identified in numerous systems: BCC spheres, bicontinuous gyroid, hexagonally-packed cylinders, and lamellae.[1, 2] The shape, the size, and the separation distance of the domains can be easily controlled by the total length of the copolymer and the volume fraction of each block. Block copolymers that self-assemble into ordered arrays of nanometer-sized domains have attracted much attention due to this facility for tuning nanostructure and their potential use as templates for the fabrication of functional nanostructure.[3] Nanoporous materials have been shown to be useful for many applications such as separation membranes,[4] interlayer dielectrics,[5] catalysts,[6] and templates for lithography.[7] The first demonstrated example of nanoporous materials from an ordered block copolymer was reported in 1988.[8] In that work, a triblock copolymer film in a lamellar structure was treated with ozone to yield polymer nanoporous materials. After that work, many scientists have employed similar strategies to prepare nanoporous material.[9, 10]

There are two important processes in preparing nanoporous materials from microphase-separated block copolymers: cross-linking and etching. Etching of either component of a block copolymer creates pores in the matrix[11] while cross-linking

toughens the matrix to stand exposure to solvents and mechanical stress.[12] A variety of methods were employed for cross-linking and etching such as chemical reagents, UV light, and electron beam.[7, 13-20] Here the author used γ-rays for both cross-linking and etching of polymers. When irradiated with γ-rays, the polymer can undergo cross-linking and degradation at the same time, but in many cases either effect is predominant. In this aspect, polymers can be roughly classified into radiation cross-linking and radiation degrading polymers.[21] By preparing the block copolymers for which the minor component is a radiation degrading polymer and the major component is a radiation cross-linking polymer, the cross-linking and degradation for each block can be simultaneously induced by γ-irradiation, and polymer nanoporous materials can be fabricated. Thus, the γ-ray-induced fabrication is expected to serve as a one-step technique for preparing the nanoporous material from microphase-separated structure if appropriate block copolymers are selected. In addition, this method has another merit that residuals in the products can be reduced because this method requires no initiators and catalysts. In the present chapter, the author investigated two diblock copolymers, polybutadiene-*block*-poly(methyl methacrylate) (PB-*b*-PMMA) and polystyrene-*block*-poly(methyl methacrylate) (PS-*b*-PMMA), with the cylinder-type microphase-separated structure. PB and PMMA are classified into radiation cross-linking and radiation degrading polymers, respectively. PS is a radiation insensitive polymer because it requires much larger dose than other common radiation cross-linking polymers do, although PS is classified into a radiation cross-linking polymer in many cases. Here the author describes the γ-ray-induced fabrication of the polymer nanoporous materials from PB-*b*-PMMA through the cross-linking of PB component and the simultaneous degradation of PMMA component. The results of the solubility tests, IR spectroscopy, and electron microscopy observation are compared between PB-*b*-PMMA and PS-*b*-PMMA to confirm the successful fabrication of nanopores in the polymer film.

7.2. EXPERIMENTAL SECTION

7.2.1. Materials

Polybutadiene(1,4 addition)-*block*-poly(methyl methacrylate) (syndiotactic) diblock copolymer (PB-*b*-PMMA) was purchased from Polymer Source Inc. Number average molecular weight of each block is 1.52×10^5 and 1.53×10^5 for PB and PMMA, respectively. Polydispersity index of PB-*b*-PMMA determined by size exclusion chromatography (SEC) is 1.15. Polystyrene-block-poly(methyl methacrylate) diblock copolymer (PS-*b*-PMMA) was also purchased from Polymer Source Inc. Number average molecular weight of each block is 1.70×10^5 and 1.68×10^5 for PS and PMMA, respectively. Polydispersity index of PS-*b*-PMMA determined by SEC is 1.10. Polystyrene homopolymer (hPS) was purchased from Tosoh Corp. Number average molecular weight is 1.8×10^4 . Polydispersity index of PS is 1.01.

7.2.2. Sample Preparation

Film samples were prepared by casting from solutions. PB-*b*-PMMA was dissolved in toluene at a concentration of 3 wt%. PS-*b*-PMMA was dissolved in THF together with hPS. The PS weight fraction of PS-*b*-PMMA/hPS blend was 68 % to form the similar microphase-separated structure. The solutions were cast in Petri dishes and slowly dried at room temperature for the period of 4 weeks until the solvent was completely evaporated. The thickness of the as-cast film was about 700 μm. The film was transferred into a glass tube, degassed, and then irradiated 65 ˚C with γ-rays from the ^{60}Co γ-ray source at Research Reactor Institute, Kyoto University. The dose rate and total irradiation dose were 13.1 kGy h^{-1} and 1 MGy, respectively. To remove fragmentary molecules, irradiated PB-*b*-PMMA and PS-*b*-PMMA were immersed in dichloromethane and in ethanol, respectively, for 12 h and dried under vacuum.

7.2.3. Measurements

FT-IR spectra of the block copolymers were obtained on a JASCO FT/IR-460 Plus ST-L in the wavenumber range from 4000 to 250 cm^{-1} at room temperature using the KBr pellet method.

Ultra-thin specimens for the transmission electron microscopy (TEM) observation were prepared with a Reichert-Nissei Ultracut-S ultramicrotome. The ultra-thin specimens of PB-*b*-PMMA were exposed to OsO_4 vapor for 1 h to stain the PB domains, and those of PS-*b*-PMMA were exposed to RuO_4 vapor for 5 min to stain the PS domains. In some cases, PMMA domains were stained by I_2 vapor for 10 days at room temperature. TEM images were obtained on JEOL JEM2000FXZ at an acceleration voltage of 200 keV. The irradiated PB-*b*-PMMA films for scanning electron microscopy (SEM) measurement were freeze-fractured according to a conventional method and the fractured surfaces were sputter-coated with a 5-nm thick layer of Pt-Pd using a ion-coater (IB-3, EIKO). The nanostructure of the films was observed by SEM (JSM6335F, JEOL) operated at 5.0 keV.

7.3. RESULT AND DISCUSSION

7.3.1. Solubility Test and IR Spectra

As a preliminary test for the cross-linking, the THF solubility of the block copolymer films was investigated before and after γ-irradiation. THF is a good solvent for all components of the block copolymers. Both block copolymer films were completely dissolved in THF before the γ-irradiation but not after the γ-irradiation. These results indicate that the PB component and the PS component were cross-linked by the γ-irradiation. However, the appearance of the immersed films in THF was different. The irradiated PS-*b*-PMMA films were slightly swollen with THF, while no

change was observed for the irradiated PB-*b*-PMMA films. This result shows that PB-*b*-PMMA was more rigidly cross-linked.

To obtain clearer information for cross-linking and degradation of each component of the block copolymers, IR spectra were measured. Figure 7.1 shows IR spectra of PB-*b*-PMMA before and after the γ-irradiation. The peaks corresponding to the carbon-carbon double bond of PB (typically 1650, 1000, and 900 cm^{-1}) diminish after γ-irradiation, resulting from the cross-linking of PB by γ-irradiation. On the other hand, in spite of the expectation that the degradation of PMMA weakens the carbonyl peak at around 1750 cm^{-1}, little change is seen after the γ-irradiation. The reason for this discrepancy can be explained as follows. Firstly, γ-rays cause the PMMA chain scission but not carbonyl group decomposition. The residual PMMA fragments were

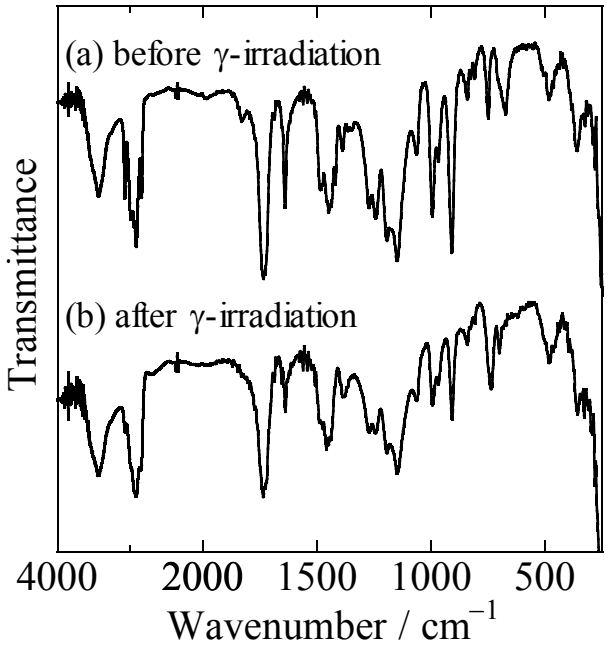

Figure 7.1. IR spectra of PB-*b*-PMMA before (a) and after (b) γ-irradiation. The peaks corresponding to the carbon-carbon double bond in PB-*b*-PMMA after γ-irradiation are smaller than those before γ-irradiation.

not removed by the solvent washing, resulting in the absorption at 1750 cm^{-1}. Secondly, the short PMMA chains are still linked to PB block. And lastly, the strong absorption of the PMMA carbonyl group was saturated and accordingly small changes were hard to discern.

The IR spectra of PS-*b*-PMMA do not exhibit distinct difference before and after γ-irradiation. This result seems inconsistent with the result of the solubility test. However, since the IR spectral changes for PS caused by the cross-linking are generally small, those changes were hardly detectable due to the low degree of PS cross-linking.

7.3.2. TEM Measurement

The cross-linking of PB and PS was confirmed by the solubility test and the IR spectroscopy, but the degradation of PMMA was not. Therefore the author tried to observe the nanostructure of the block copolymers before and after γ-irradiation by TEM. Figure 7.2 shows a TEM image of a PB-*b*-PMMA specimen before the γ-irradiation. The contrast of the micrograph is provided by the selective staining of PB with OsO_4. The dark and the bright phases in Figure 7.2 correspond to the PB matrix and the cylindrical PMMA microdomains, respectively. The micrograph shows that PB-*b*-PMMA forms the microdomain structure of PMMA cylinders hexagonally-packed in the PB matrix and the diameter of the PMMA cylindrical microdomains is approximately 50 nm.

A TEM image of a PS-*b*-PMMA/hPS blend specimen before the γ-irradiation is shown in Figure 7.3. The dark and the bright phases in Figure 7.3 correspond to the PS matrix and the cylindrical PMMA microdomains, respectively, because the PS domain was selectively stained with RuO_4. The micrograph shows that this PS-*b*-PMMA/hPS blend polymer also forms hexagonally-packed PMMA cylinders in the PS matrix.

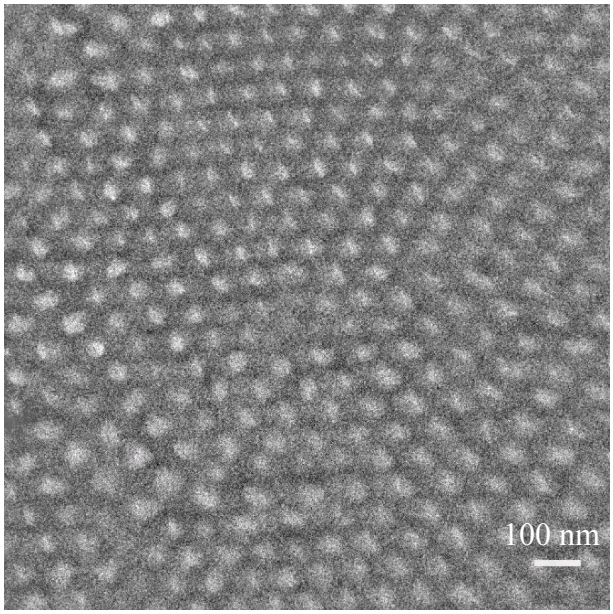

Figure 7.2. A TEM image of PB-*b*-PMMA before γ-irradiation showing a cylinder structure. The PB block was stained with OsO_4.

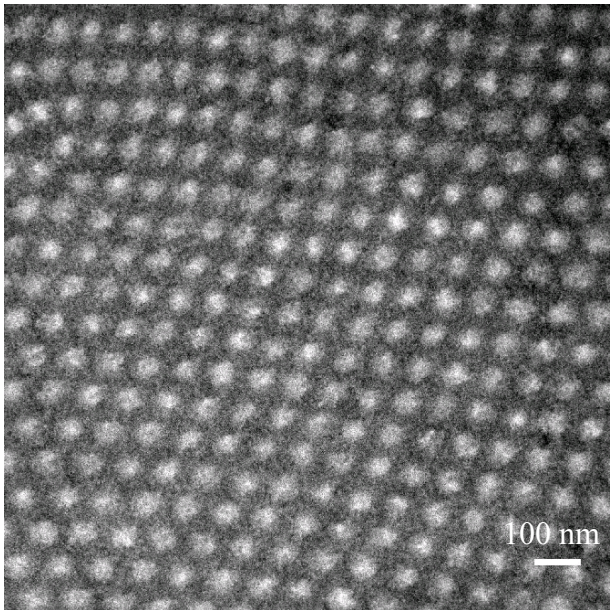

Figure 7.3. A TEM image of PS-*b*-PMMA before γ-irradiation showing a cylinder structure. The PS block was stained with RuO_4.

A TEM image of an unstained PB-*b*-PMMA specimen after the γ-irradiation is shown in Figure 7.4. Even without staining, the boundary between the bright cylindrical microdomains and the dark matrix after the γ-irradiation becomes clearer than that before the γ-irradiation. This sharp contrast obtained without staining indicates that the cylindrical microdomains are not as dense as the PB matrix and implies that the PMMA chains in the cylindrical microdomains are degraded by γ-irradiation and removed. Moreover, the bright rings around the edges of the cylinders are the thickness fringes observed with the defocus condition and suggest that the insides of the cylinders are empty. The hole diameter is approximately 50 nm, which is in good agreement with that before γ-irradiation. This result indicates that the original microdomain structure in the cast film is maintained even after the removal of the PMMA chains with dichloromethane.

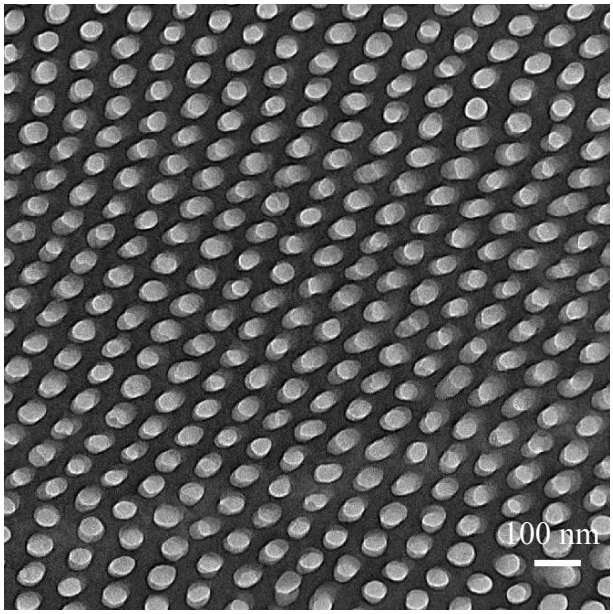

Figure 7.4. A TEM image of PB-*b*-PMMA after γ-irradiation without staining. The boundary between the PB matrix and the PMMA microdomains is clearer than that before γ-irradiation.

A comparison of the TEM images for PB-*b*-PMMA reveals that the shape, the size of the nanopattern, and the separation distance between the cylindrical microdomains completely coincide before and after the γ-irradiation. This fact means that the polymer nanoporous material was prepared by the γ-irradiation maintaining the original structure of the microphase-separated PB-*b*-PMMA.

Figure 7.5 shows a TEM image of an unstained PS-*b*-PMMA specimen after the γ-irradiation. The domain boundary is less clear than that of the PB-*b*-PMMA specimen shown in Figure 7.4. This result indicates that the PMMA chains remain in the cylindrical domains. The unclear boundary between the two components is due to the insufficient degradation of PMMA. The difference between PB-*b*-PMMA and PS-*b*-PMMA can be attributed to the protection effect of the aromatic rings in the PS block against γ-irradiation.[22] Thus, PS-*b*-PMMA is harder to yield a polymer nanoporous material than PB-*b*-PMMA.

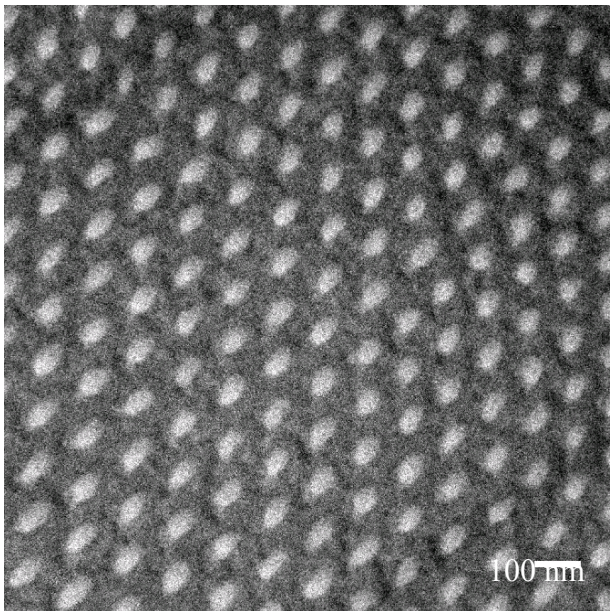

Figure 7.5. A TEM image of PS-*b*-PMMA after γ-irradiation without staining. The boundary between the PS matrix and the PMMA microdomains is less clear than that in the case of PB-*b*-PMMA after γ-irradiation.

To examine the degree of the degradation and removal of the PMMA block in a more detectable way, the author stained the PMMA microdomains with I_2. TEM images of I_2-stained PS-*b*-PMMA before and after the γ-irradiation are shown in Figure 7.6. The dark and the bright phases in Figure 7.6 correspond to the PMMA microdomains and the PS matrix, respectively. The contrast between the PMMA microdomains and the PS matrix after the γ-irradiation is much lower than that before γ-irradiation, indicating that PMMA in PS-*b*-PMMA is degraded by γ-irradiation and partly removed.

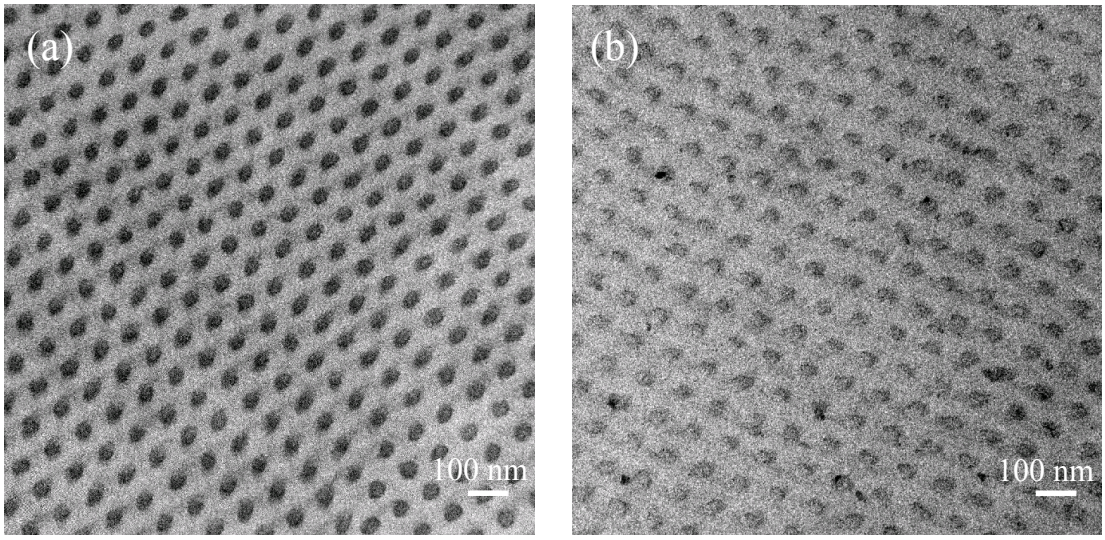

Figure 7.6. TEM images of PS-*b*-PMMA before (a) and after (b) γ-irradiation. The PMMA block was stained with I_2. The PMMA microdomains after γ-irradiation are brighter than those before γ-irradiation.

7.3.3. SEM Measurement

The TEM observation for the I_2-stained PB-*b*-PMMA specimens was also tried, but failed owing to the denser staining of the PB matrix than the PMMA microdomains. Therefore the formation of nanoporous materials created in the PB matrix was investigated by SEM. The SEM micrograph in Figure 7.7 exhibits the formation of cylindrical holes over the entire film. The pore diameter estimated from the micrograph is approximately 40 nm, which agrees with the estimated value from the TEM micrograph by taking the 5-nm thick Pt-Pd coating into account. This result indicates that the pores and lines with dark shadows may correspond to the removed PMMA domains.

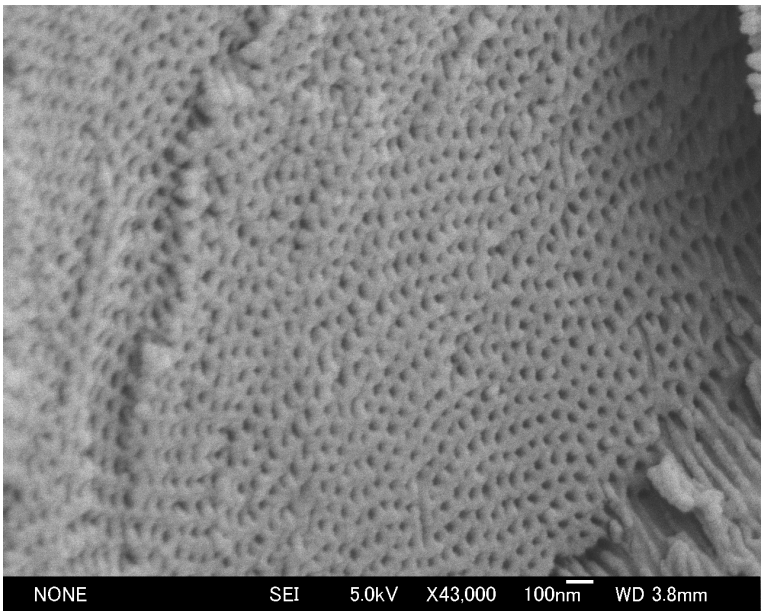

Figure 7.7. A SEM image showing nanoporous formed in PB matrix through the γ-ray-induced degradation of the PMMA block of the microphase-separated film.

Here, the result of the IR measurement should be explained again. The SEM result clearly shows the elimination of PMMA microdomains, whereas little change is observed for the PMMA carbonyl peak in the IR spectra after the γ-irradiation. This is partly due to the difference of the observed area. Although the IR spectra reflect all molecules throughout the whole depth of samples, SEM visualizes only the surface of samples. It is very likely that the fragmentary molecules resulting from the PMMA degradation can be easily removed at the near surface of the SEM specimen.

The following scheme is given for the results in this chapter. When a PB-*b*-PMMA film is irradiated, the PB component is cross-linked and the irradiated film becomes insoluble to THF while maintaining the microphase-separated structure. At the same time, the PMMA component is degraded and a polymer nanoporous film is fabricated from PB-*b*-PMMA. On the other hand, the cross-linking of the PS component in PS-*b*-PMMA is less favorable than that of the PB component in PB-*b*-PMMA. The degree of the degradation of the PMMA component in PS-*b*-PMMA is also smaller than that of the PMMA component in PB-*b*-PMMA. The difference in PB and PS cross-linking efficiency and PMMA degradation efficiency of the block copolymers is due to the protection effect against γ-irradiation by the aromatic rings in PS. These results indicate that PB is more suitable substance for the fixation of the microphase-separated structure and the preparation of the polymer nanoporous materials than PS.

Finally, the results in this chapter should be compared with previous studies on UV-light-induced simultaneous degradation and cross-linking of cylindrically microphase-separated structure of PS-*b*-PMMA, which was reported by T. Thurn-Albrecht et al.[19,20] In their study, the UV light irradiation caused the PMMA degradation and the PS cross-linking, but the largest difference from ours is that they could completely remove the PMMA microdomains by rinsing with acetic acid. The author

ascribes this difference to the following reasons. Firstly, the radiation sources are different. Although the quantitative comparison of the radiation effects on these polymers is not easy, the highly penetrative γ-rays cause less reactions in the polymers. Especially for PS-*b*-PMMA, the protection effect of the PS aromatic rings against γ-rays retards the γ-ray-induced reactions, leading to the insufficient PMMA degradation. Secondly, the difference in the sample preparation method is responsible. They applied an electric field to the copolymer film (800 nm), whereas we did not apply any special treatments in the microdomain formation process. The PMMA fragments by degradation can be readily let out from highly-oriented "straight" cylindrical holes. Finally, the presence of atmospheric oxygen may promote PMMA degradation in their case. In any case, the relationship between the radiation sources and the effects on microphase-separated structures needs further investigation under more refined experimental conditions.

7.4. CONCLUSION

γ-Irradiation of PB-*b*-PMMA induced the cross-linking of the PB matrix and the degradation of the cylindrical PMMA microdomains at the same time. The original structure of PB-*b*-PMMA as a template was maintained and the nanoporous material could be prepared by the use of γ-rays. On the other hand, the PMMA component in PS-*b*-PMMA was not degraded enough because of the protection effect by the aromatic rings in PS. The polymers having aromatic rings as a component of block copolymers are not appropriate for the radiation-induced fabrication of polymer nanoporous materials.

The polymer nanoporous materials presented in this study were simply made by the γ-irradiation. This method is applicable to the various microphase-separated

structures because the radiation-induced cross-linking and degradation are not destructive to the structures of phase separation. Since the morphology and the size of microphase-separated structure are easily controlled, the use of γ-rays for block copolymers is a facile method for nanomaterials.

References

1. I. W. Hamley, "*The Physics of Block Copolymers*", Oxford University Press, New York (1998).
2. F. S. Bates and G. H. Fredrickson, *Annu. Rev. Phys. Chem.*, **41**, 525 (1990).
3. T. P. Russell, T. Thurn-Albrecht, M. Tuominen, E. Huang, and C. J. Hawker, *Macromol. Symp.*, **159**, 77 (2000).
4. J. Miroslav, D. Sykora, F. Svec, J. M. J. Frechet, J. Schweer, and R. J. Holm, *J. Polym. Sci. Part A: Polym. Chem.*, **38**, 2767 (2000).
5. C. V. Nguyen, K. R. Carter, C. J. Hawker, J. L. Hedrick, R. L. Jaffe, R. D. Miller, J. F. Remenar, H.-W. Rhee, P. M. Rice, M. F. Toney, M. Trollsas, and D. Y. Yoon, *Chem. Mater.*, **11**, 3080 (1999).
6. J. L. Hedrick, C. J. Hawker, R. DiPietro, R. Jerome, and Y. Charlier, *Polymer*, **36**, 4855 (1995).
7. M. Park, C. Harrison, P. M. Chaikin, R. A. Register, and D. H. Adamson, *Science*, **276**, 1401 (1997).
8. J. Lee, A. Hirao, and S. Nakahama, *Macromolecules*, **21**, 274 (1988).
9. T. Hashimoto, K. Tsutsumi, and Y. Funaki, *Langmuir*, **13**, 6869 (1997).
10. U. Jeong, D. Y. Ryu, J. K. Kim, D. H. Kim, T. P. Russell, and C. J. Hawker, *Adv. Mater.*, **15**, 1247 (2003).
11. S. Ndoni, M. E. Vigild, and R. H. Berg, *J. Am. Chem. Soc.*, **125**, 13366 (2003).
12. M. S. Hansen, M. E. Vigild, R. H. Berg, and S. Ndoni, *Polym. Bull.*, **51**, 403 (2004).
13. Z. Lu, G. Liu, H. Phillips, J. M. Hill, J. Chang, and R. A. Kydd, *Nano Lett.*, **1**, 683 (2001).
14. H. Mao and M. A. Hillmyer, *Macromolecules*, **38**, 4038 (2005).
15. F. Guo, J. W. Andreasen, M. E. Vigild, and S. Ndoni, *Macromolecules*, **40**, 3669 (2007).

16. K.W. Guarini, C. T. Black, and S. H. I. Yeung, *Adv. Mater.*, **14**, 1290 (2002).
17. U. Jeong, H.-C. Kim, R. L. Rodriguez, I. Y. Tsai, C. M. Stafford, J. K. Kim, C. J. Hawker, and T. P. Russell, *Adv. Mater.*, **14**, 274 (2002).
18. U. Jeong, D. Y. Ryu, J. K. Kim, D. H. Kim, T. P. Russell, and C. J. Hawker, *Adv. Mater.*, **15**, 1427 (2003).
19. T. Thurn-Albrecht, J. Schotter, G. A. Kästle, N. Emley, T. Shibauchi, L. Krusin-Elbaum, K. Guarini, C. T. Black, M. T. Tuominen, and T. P. Russell, *Science*, **290**, 2126 (2000).
20. T. Thurn-Albrecht, R. Steiner, J. DeRouchey, C. M. Stafford, E. Huang, M. Bal, M. Tuominen, C. J. Hawker, and T. P. Russell, *Adv. Mater.*, **12**, 787 (2000).
21. A.Chapiro, "*Radiation Chemistry of Polymeric Systems*" Wiley, New York (1962).
22. A. Charlesby, "*Atomic Radiation and Polymers*", Pergamon Press, Oxford (1960).

SUMMARY

In this thesis, the conformational characteristics and self-assembled structures of polymers in space-limited systems were investigated by scanning near-field optical microscopy (SNOM). The former part of this thesis demonstrated the conformational characteristics of a single homopolymer chain confined in thin film and block copolymer lamella. In the latter part, the nanometric structures of block copolymers was focused on. The conformation and the chain end distribution of the block chain forming the two-dimensional microphase-separated structure were clarified by SNOM. The porous materials from the microphase-separated structure of block copolymers as a template were also described by using γ-ray. The summary of each chapter is presented below.

In Chapter 2, the conformation of poly(methyl methacrylate) (PMMA) in the confined geometry of the thin film with a thickness less than the unperturbed chain dimension in the bulk state was investigated by SNOM. The individual perylene-labeled PMMA (PMMA-Pe) chains dispersed in the thin films of the unlabeled PMMA prepared by the spin-coating and Langmuir-Blodgett techniques were observed by SNOM. The effect of the constraint in the height direction on the radius of gyration in the direction parallel to the film surface, R_{xy}, was examined. In the thickness range of 1−100 nm, R_{xy} in the ultra thin films was not significantly altered from that in the bulk state, indicating that the PMMA chain has lowered interchain interlacement in the ultra thin films.

In Chapter 3, the conformational rearrangement of PMMA chains confined in a two-dimensional monolayer to three-dimensional random coils was studied by SNOM. PMMA-Pe chains were dispersed in the unlabeled PMMA monolayer, and then it was

placed on a thick film of unlabeled PMMA and annealed above the glass transition temperature. Although R_{xy} in the lateral directions was maintained through the annealing process, the segment density showed a distribution closer to the Gaussian type after annealing. On the other hand, the observation from the direction normal to the sample surface revealed that the PMMA chains penetrated into the bulk substrate at a rate much faster than the translational diffusion of the entire polymer chains, suggesting that the unstable two-dimensional conformation of polymer chains relaxed into the three-dimensional ones. This indicates that the polymer chains confined in a monolayer interlaced with the surrounding chains and expanded mainly toward the depth direction on the relaxation processes, while keeping the dimensions of averaged radius of gyration in the lateral directions.

In Chapter 4, the localization and orientation of PMMA-Pe homopolymer chain confined in the polystyrene-*block*-poly(methyl methacrylate) (PS-*b*-PMMA) lamella were investigated by SNOM. The analysis of the center of mass (CM) of PMMA-Pe chain revealed that the PMMA homopolymer chains were distributed throughout the PMMA-rich domain layers, with the maximum CM population at the domain centers. The orientation of the PMMA homopolymer chains is dependent on the CM location in the PMMA domain. When the CM locates at the domain center, the homopolymer chain prefers an orientation parallel with the lamella. When the CM is close to the domain interface, the homopolymer chain tends to orient itself perpendicularly to the interface. This location dependence of chain orientation is the result of the rotational freedom of PMMA homopolymer chains in the PMMA-rich domains of the PS-*b*-PMMA lamella

In Chapter 5, the localization and the orientation of the symmetric diblock copolymer chain in a quasi-two-dimensional microphase-separated structure were studied by SNOM. In the monolayer of poly(octadecyl methacrylate)-*block*-

poly(isobutyl methacrylate) (PODMA-*b*-PiBMA), the individual PiBMA sub-chains were directly observed by SNOM, and the CM position and the orientational angle relative to the phase interface were examined at the single chain level. It was found that the CM position and the orientation of the PiBMA sub-chain in the lamellar structure were dependent on the curvature of the PiBMA/PODMA interface. As the interface was bent toward the objective chain, the block chain preferred the CM position closer to the domain center, and conformation was strongly oriented perpendicularly to the domain interface. With increase of the curvature, the steric hindrance among the block chain increases, resulting in the stretched conformation.

In Chapter 6, the chain end distribution of the block copolymer in a two-dimensional microphase-separated structure was studied by SNOM. In the PODMA-*b*-PiBMA monolayer, the free end of the PiBMA sub-chain was directly observed by SNOM, and the spatial distributions of the whole block and the chain end were examined and compared with the convolution of the point spread function of microscope and distribution function of model structures. It was found that the chain end distribution of the block copolymer confined in two dimensions has the peak near the domain center, being concentrated in the narrower region compared with the three-dimensional systems.

In Chapter 7, the polymer nanoporous materials with periodic cylindrical holes were fabricated from microphase-separated structure of diblock copolymers consisting of a radiation cross-linking polymer and a radiation degrading polymer through simultaneous cross-linking and degradation by the γ-irradiation. A polybutadiene-*block*-poly(methyl methacrylate) diblock copolymer (PB-*b*-PMMA) film which self-assembles into hexagonally-packed poly(methyl methacrylate) cylinders in polybutadiene matrix was irradiated with γ-rays. Solubility test, IR spectroscopy, and electron microscopy observation for a PB-*b*-PMMAr film in comparison to a PS-*b*-

PMMA film revealed that PMMA domains were removed by the γ-irradiation and succeeding solvent washing to form cylindrical holes within polybutadiene matrix which was rigidified by the radiation cross-linking. Thus, the polymer nanoporous material can be prepared by the γ-irradiation while keeping the original structure of PB-*b*-PMMA.

LIST OF PUBLICATION

Chapter 2

Conformation of Single Poly(methyl methacrylate) Chains in an Ultra-Thin Film Studied by Scanning Near-Field Optical Microscopy

Hiroyuki Aoki, Sayuri Morita, Ryojun Sekine, and Shinzaburo Ito

Polymer Journal, **40**, 274 (2008).

Chapter 3

Conformational Relaxation of Single Polymer Chain Confined in a Monolayer Studied by Scanning Near-Field Optical Microscopy

Ryojun Sekine, Tatsuya Iwamoto, Hiroyuki Aoki, and Shinzaburo Ito

Submitted to *Langmuir.*

Chapter 4

Localization and Orientation of Homopolymer in Block Copolymer Lamella Studied by Scanning Near-Field Optical Microscopy

Jian Yang, Ryojun Sekine, Hiroyuki Aoki, and Shinzaburo Ito

Macromolecules, **40**, 7573 (2007).

Chapter 5

Conformation of Single Block Copolymer Chain in Two-Dimensional Microphase-Separated Structure Studied by Scanning Near-Field Optical Microscopy

Ryojun Sekine, Hiroyuki Aoki, and Shinzaburo Ito

The Journal of Physical Chemistry B, in press.

Chapter 6

Chain End Distribution in Two-Dimensional Microphase-Separated Structure Studied by Scanning Near-Field Optical Microscopy

Ryojun Sekine, Hiroyuki Aoki, and Shinzaburo Ito

Submitted to *The Journal of Physical Chemistry B*.

Chapter7

Radiation-Induced Fabrication of Polymer Nanoporous Materials from Microphase-Separated Structure of Diblock Copolymers as a Template

Ryojun Sekine, Nobuhiro Sato, Tomochika Matsuyama, Satoshi Akasaka, and Hirokazu Hasegawa

Journal of Polymer Science Part A: Polymer Chemistry, **45**, 5916 (2007).

Others

Studies on Uniaxial Tensile Behaviour of Poly(ester ester) Thermoplastic Elastomers

Takanobu Kawamura, Koh-Hei Nitta, Ryojun Sekine, Kenji Urayama,

Shinzo Kohjiya, and Toshikazu Takigawa

Macromolecules: An Indian Journal, **3**, 15 (2007).

ACKNOWLEDGEMENT

The studies presented in this thesis were carried out at the Department of Polymer Chemistry, Graduate School of Engineering, Kyoto University, from 2004 to 2009. The author would like to express his most sincere thanks to Professor Shinzaburo Ito for his continuous guidance, valuable advices, and significant discussions throughout this study. The author would like to sincerely express his gratitude to Emeritus Professor Tomochica Matsuyama for his kind guidance, encouragement, valuable comments and discussions.

Professor Toshiji Kanaya and Professor Hirokazu Hasegawa are especially acknowledged for their critical review of this thesis.

The author is deeply indebted to Associate Professor Hiroyuki Aoki for his critical comments, thoughtful advices, and collaborations throughout this investigation.

The author is indebted to Dr. Nobuhiro Sato for his helpful guidance and advices.

The author wishes to express my sincere gratitude to Associate Professor Hideo Ohkita and Dr. Hiroaki Benten for their suggestions and advices in various situations.

The author is sincerely grateful to Professor Hirokazu Hasegawa, and Mr. Satoshi Akasaka for their kind support in electron microscopy measurements.

The author acknowledges the active collaboration and fruitful discussion with the colleagues of Ito Laboratory and Matsuyama Laboratory: especially, Dr. Jian Yang, Mr. Michihiro Ogawa, Mr. Toru Ube, Mr. Satoshi Honda, and Mr. Hidenori Tanaka. Without their collaboration and support, the author could not carry out his studies.

At last, the author expresses his sincere gratitude to his parents, Yoshitaka Sekine and Kyoko Sekine, for their support and encouragement.

March, 2009

Ryojun Sekine